

AD-A161 544

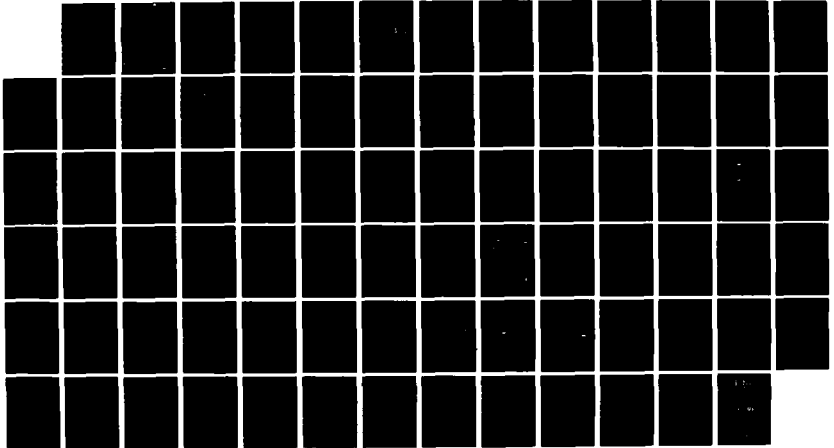
NON-LINEAR WAVE PHENOMENA IN JOSEPHSON ELEMENTS FOR
SUPERCONDUCTING ELECT. (U) TECHNICAL UNIV OF DENMARK
LYNGBY LAB OF APPLIED MATHEMATICAL P.
P L CHRISTIANSEN ET AL. JUL 85

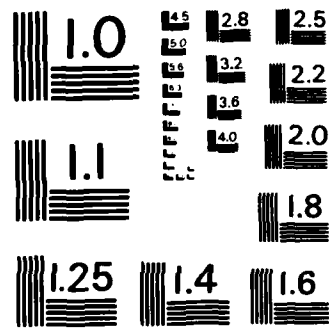
12

UNCLASSIFIED

F/G 9/3

ML





MICROCOPY RESOLUTION TEST CHART
NATIONAL BUREAU OF STANDARDS-1963-A

AD-A161 544

DTIC COPY

DTIC
SELECTED
NOV 26 1985
S D

REPORT DOCUMENTATION PAGE		READ INSTRUCTIONS BEFORE COMPLETING FORM
1. REPORT NUMBER	2. GOVT ACCESSION NO. AD-A161	3. RECIPIENT'S CATALOG NUMBER 544
4. TITLE (and Subtitle) Non-Linear Wave Phenomena in Josephson Elements for Superconducting Electronics		5. TYPE OF REPORT & PERIOD COVERED Final Technical Report April - June 1985
		6. PERFORMING ORG. REPORT NUMBER
7. AUTHOR(s) P.L. Christiansen, R.D. Parmentier, O. Skovgaard		8. CONTRACT OR GRANT NUMBER(s) DAJA37-82-C-0057
9. PERFORMING ORGANIZATION NAME AND ADDRESS Laboratory of Applied Mathematical Physics Technical University of Denmark, Bldg 303 DK-2800 Lyngby, Denmark		10. PROGRAM ELEMENT, PROJECT, TASK AREA & WORK UNIT NUMBERS 61102A 1T161102BH57-0-07
11. CONTROLLING OFFICE NAME AND ADDRESS USARDSG-UK Box 65, FPO NY 09510-1500		12. REPORT DATE July 1985
		13. NUMBER OF PAGES 24
14. MONITORING AGENCY NAME & ADDRESS (if different from Controlling Office)		15. SECURITY CLASS. (of this report) Unclassified
		15a. DECLASSIFICATION/DOWNGRADING SCHEDULE
16. DISTRIBUTION STATEMENT (of this Report) Approved for public release; distribution unlimited.		
17. DISTRIBUTION STATEMENT (of the abstract entered in Block 20, if different from Report)		
18. SUPPLEMENTARY NOTES		
19. KEY WORDS (Continue on reverse side if necessary and identify by block number) Cavity mode, Chaos, Fiske Steps, Hysteresis, Intermittency, Josephson fluxon Oscillator, Josephson ring oscillator, Josephson tunnel junction, Noise rise, Perturbation theory, Radiation line-width, Sine-Gordon equation (perturbed), Soliton (fluxon), SQUID, Subharmonics, Zero field steps. 4		
20. ABSTRACT (Continue on reverse side if necessary and identify by block number) The long and intermediate length Josephson tunnel junction oscillator with overlap geometry of linear and circular configuration, is investigated by computational solution of the perturbed sine-Gordon equation model and by experimental measurements. The model predicts the experimental results very well. Line oscillators as well as ring oscillators are treated. For long junctions soliton perturbation methods are developed and turn out to be efficient prediction tools, also providing physical understanding of the		

dynamics of the oscillator. For intermediate length junctions expansions in terms of linear cavity modes reduce computational costs.

The narrow linewidth of the electromagnetic radiation (typically 1 kHz of a line at 10 GHz) is demonstrated experimentally. Corresponding computer simulations requiring a relative accuracy of less than 10^{-7} are performed on supercomputer CRAY-1-S. The broadening of linewidth due to external microwave radiation and internal thermal noise is determined.

The effect of constant magnetic fields, applied to tune the radiation frequency, on the resonant soliton oscillations is investigated by detailed computations of the power spectra. Hysteresis and chaotic intermittency between soliton dynamic states are found. In narrow windows of parameter space chaos effects cause noise rise.

Poincare and return maps, Painleve and Melnikov methods are applied to indicate and predict chaos in ordinary differential equations of sine-Gordon type modelling SQUIDS.

Accession For	
NTIS CRA&I	<input checked="" type="checkbox"/>
DTIC TAB	<input type="checkbox"/>
Unannounced	<input type="checkbox"/>
Justification	
By	
Distribution /	
Availability Codes	
Dist	Avail and/or Special
A-1	



AD

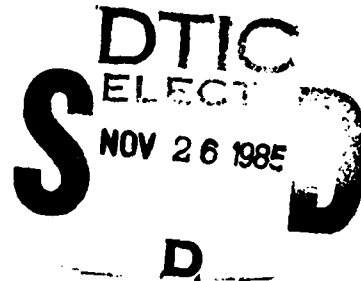
NON-LINEAR WAVE PHENOMENA IN JOSEPHSON
ELEMENTS FOR SUPERCONDUCTING ELETRONICS

Final Technical Report

by

P.L. Christiansen, R.D. Parmentier
and O. Skovgaard

July 1985



United States Army
EUROPEAN RESEARCH OFFICE OF THE U.S. ARMY
London England

CONTRACT NUMBER DAJA37-82-C-0057

Laboratory of Applied Mathematical Physics
The Technical University of Denmark
Building 303
DK-2800 Lyngby
Denmark

Approved for Public Release; distribution unlimited

SUMMARY

The long and intermediate length Josephson tunnel junction oscillator with overlap geometry of linear and circular configuration, is investigated by computational solution of the perturbed sine-Gordon equation model and by experimental measurements. The model predicts the experimental results very well. Line oscillators as well as ring oscillators are treated. For long junctions soliton perturbation methods are developed and turn out to be efficient prediction tools, also providing physical understanding of the dynamics of the oscillator. For intermediate length junctions expansions in terms of linear cavity modes reduce computational costs.

The narrow linewidth of the electromagnetic radiation (typically 1 kHz of a line at 10 GHz) is demonstrated experimentally. Corresponding computer simulations requiring a relative accuracy of less than 10^{-7} are performed on supercomputer CRAY-1-S. The broadening of linewidth due to external microwave radiation and internal thermal noise is determined.

The effect of constant magnetic fields, applied to tune the radiation frequency, on the resonant soliton oscillations is investigated by detailed computations of the power spectra. Hysteresis and chaotic intermittency between soliton dynamic states are found. In narrow windows of parameter space chaos effects cause noise rise.

Poincaré and return maps, Painlevé and Melnikov methods are applied to indicate and predict chaos in ordinary differential equations of sine-Gordon type modelling SQUIDs.

KEY WORDS

Cavity mode, Chaos, Fiske steps, Hysteresis, Intermittency, Josephson fluxon oscillator, Josephson ring oscillator, Josephson tunnel junction, Noise rise, Perturbation theory, Radiation linewidth, Sine-Gordon equation (perturbed), Soliton (fluxon), SQUID, Subharmonics, Zero field steps.

TABLE OF CONTENTS

	Page
Summary	1
List of Keywords	1
Table of Contents	2
List of Appendixes	3
List of Illustrations	3
Nonlinear Wave Phenomena in Josephson Elements for Superconducting Electronics	4
Introduction	4
Background	6
The Josephson Oscillator	7
The Dynamics of the Josephson Oscillator	10
Linewidth of Electromagnetic Radiation from Josephson Oscillator	15
Effects of External Magnetic Fields on Soliton Dynamics	16
Soliton and Chaos Effects on the Josephson Oscillator	17
Other Research in Connection with the Present Contract	21
Perspectives	21
Literature Cited	23

LIST OF APPENDIXES

The following major reprints and preprints are enclosed as appendixes.

M. Salerno and A.C. Scott, Phys. Rev. B 26, 2474 (1982).

M.P. Soerensen, P.L. Christiansen, R.D. Parmentier, and O. Skovgaard, Appl. Phys. Lett. 42, 739 (1983).

S.N. Ern , A. Ferrigno, and R.D. Parmentier, Phys. Rev. B 27, 5440 (1983).

M.P. Soerensen, N. Arley, P.L. Christiansen, and O. Skovgaard, Phys. Rev. Lett. 51, 1919 (1983).

F. If, M.P. Soerensen, and P.L. Christiansen, Phys. Lett. 100A, 68 (1984).

M. Salerno, E. Joergensen, and M.R. Samuelsen, Phys. Rev. B 30, 2635 (1984).

M. P. Soerensen, R.D. Parmentier, P.L. Christiansen, O. Skovgaard, B. Dueholm, E. Joergensen, V.P. Koshelets, O.A. Levring, R. Monaco, J. Mygind, N.F. Pedersen, and M.R. Samuelsen, Phys. Rev. B 30, 2640 (1984).

F. If, P.L. Christiansen, R.D. Parmentier, O. Skovgaard, and M.P. Soerensen (to appear in Phys. Rev. B).

M.P. Soerensen, M. Bartuccelli, P.L. Christiansen, and A.R. Bishop, Phys. Lett. 109A, 347 (1985).

LIST OF ILLUSTRATIONS

Fig. 1 Josephson junction of overlap geometry.

Fig. 2. Element of lumped transmission line equivalent circuit representing the Josephson oscillator.

Fig. 3. Computer solution of the perturbed sine-Gordon equation. One soliton.

Fig. 4. DC-voltage versus applied bias current showing the first three zero field steps.

Fig. 5 Computer solution of the perturbed sine-Gordon equation. Two solitons.

Fig. 6 Soliton dynamic states.

NONLINEAR WAVE PHENOMENA IN JOSEPHSON
ELEMENTS FOR SUPERCONDUCTING ELECTRONICS

INTRODUCTION

The work performed under this contract has been described in 7 technical reports.

1st Periodic Report	June 1982
2nd Periodic Report	October 1982
3rd Periodic Report	April 1983
4th Periodic Report + Appendix	October 1983
5th Periodic Report	April 1984
6th Periodic Report	October 1984
7th Periodic Report (Part I and II)	April 1985

The results obtained under the contract have been published as follows:

Scientific Journals

- [1] M. Salerno and A.C. Scott, "Linewidth for fluxon oscillators", Phys. Rev. B 26 (1982) 2474-2482 (enclosed).
- [2] S.N. Ern , A. Ferrigno and R.D. Parmentier, "Josephson junction fluxon oscillators of in-line geometry", IEEE Transactions on Magnetics, MAG-19 (1983) 1007-1009.
- [3] M.P. Soerensen, P.L. Christiansen, R.D. Parmentier, and O. Skovgaard, "Subharmonic generation in Josephson junction fluxon oscillators biased on Fiske steps", Appl. Phys. Lett. 42 (1983) 739-741 (enclosed).
- [4] S.N. Ern , A. Ferrigno, and R.D. Parmentier, "Fluxon propagation and Fiske steps in long Josephson tunnel junctions", Phys. Rev. B 27 (1983) 5440-5446 (enclosed).
- [5] M.P. Soerensen, N. Arley, P.L. Christiansen and O. Skovgaard, "Intermittent switching between soliton dynamic states in perturbed sine-Gordon model", Phys. Rev. Lett. 51 (1983) 1919-1922 (enclosed).
- [6] F. If, M.P. Soerensen, and P.L. Christiansen "Fluxon dynamics on the circular Josephson oscillator", Phys. Lett. 100A (1984) 68-70 (enclosed).
- [7] M. Salerno, E. Joergensen, and M.R. Samuelsen, "Phonons and solitons in the thermal sine-Gordon system", Phys. Rev. B 30 (1984) 2635-2639 (enclosed).

- [8] S. de Filippo and M. Salerno, "A geometrical approach to discretization of non-linear integrable evolution equations: I Burger's hierarchy", Phys. Lett. 101A (1984) 75-80.
- [9] M.P. Soerensen, R.D. Parmentier, P.L. Christiansen, O. Skovgaard, B. Dueholm, E. Joergensen, V.P. Koshelets, O.A. Levring, R. Monaco, J. Mygind, N.F. Pedersen, and M.R. Samuelson, "Magnetic field dependence of microwave radiation in intermediate-length Josephson junctions", Phys. Rev. B 30 (1984) 2640-2648 (enclosed).
- [10] P.L. Christiansen, "Aspects of modern non-linear dynamics: soliton and chaos phenomena", Radio Science 19 (1984) 1124-1130.
- [11] F. If, P.L. Christiansen, R.D. Parmentier, O. Skovgaard, and M.P. Soerensen, "Simulation Studies of Radiation Linewidth in circular Josephson Junction Fluxon Oscillators (to appear in Phys. Rev. B)(enclosed).
- [12] M.P. Soerensen, M. Bartuccelli, P.L. Christiansen, and A.R. Bishop, "On low-dimensional chaos in RF SQUID's", Phys. Lett. 109A (1985) 347-351 (enclosed).
- [13] M. Salerno, "A Mechanical Analog for the Double Sine-Gordon Equation" (to appear in Physica D).
- [14] M. Bartuccelli, P.L. Christiansen, N.F. Pedersen, and M.P. Soerensen, "Prediction of Chaos in a Josephson Junction by the Melnikov Function Technique" (submitted to Phys. Rev. B).

Conference Proceedings

- [15] P.L. Christiansen, "Soliton dynamic states in the sine-Gordon system", Wave Phenomena: Modern Theory and Applications, eds. C. Rogers and T.B. Moodie, Elsevier Science Publ. B.V., Amsterdam (1984) 349-360.
- [16] P.L. Christiansen, "Solitons and chaotic intermittency in the sine-Gordon system modelling the Josephson oscillator", Proceedings of a Workshop at Research Triangle Park North Carolina USA, Chaos in Nonlinear Dynamical Systems, March 13-15, 1984 ed. J. Chandra, SIAM Philadelphia (1985) 74-85.
- [17] M.P. Soerensen and R.D. Parmentier, "Josephson junction dynamics by multimode theory and numerical simulation", Proc. LT-17, eds. U. Eckern, A. Schmid, W. Weber and H. Wühl, Elsevier Science Publishers B.V., Amsterdam (1984) 707-708.
- [18] M.P. Soerensen, R.D. Parmentier, P.L. Christiansen, O. Skovgaard, B. Dueholm, E. Joergensen, V.P. Koshelets, O.A. Levring, R. Monaco, J. Mygind, N.F. Pedersen, and M.R. Samuelson, "X-Band Radiation from Josephson Junctions in Magnetic Field". IEEE Trans. Magnetics MAG-21 (1985) 629-631.

- [19] P.L. Christiansen, "Solitons and Chaos in the Sine-Gordon System", Dynamical Problems in Soliton Systems, Proc. of the 7th Kyoto Summer Institute, Kyoto, Japan, August 27-31, 1984, ed. S. Takeno, Springer-Verlag, Berlin (1985) 258-261.
- [20] P.L. Christiansen, Contribution to the discussion of J.B. Keller, "Soliton generation and nonlinear wave propagation" at "New Developments in the Theory and Application of Solitons", Royal Society of London, November 1-2, 1984 (to appear in Phil. Trans. Roy. Soc. Lond.).

Thesis

- [21] M.P. Soerensen, "Josephson junctions and sine-Gordon systems", Ph.D. Thesis, The Danish Center for Applied Mathematics and Mechanics, The Technical University of Denmark, Report S 27 (1984) 114 pp.

Major reprints and preprints are enclosed as appendixes.

In the following sections we summarize the new main results obtained under the contract. References to the published papers in the above lists will be given. Also the background for the research and the future perspectives will be discussed.

BACKGROUND

The study of soliton dynamics in connection with large Josephson tunnel junctions has recently drawn considerable theoretical [22-27] and experimental [28,29] attention*. Fulton and Dynes [1] conceived the idea that the Josephson tunnel junction could support the resonant propagation of a soliton (or fluxon) trapped in the junction, the soliton being a 2π jump in the phase difference (ϕ) across the insulating barrier which separates the two superconductors. The moving soliton is accompanied by a voltage pulse ($\sim\phi_t$) which can be detected at either end of the junction. The dc manifestation of the motion is a sequence of equidistantly spaced branches in the current-voltage characteristic of the junction. These near-constant voltage branches, which were first reported by Chen, Finnegan, and Langenberg [30], are known as zero-field steps (ZFS) because they occur also in the absence of an external magnetic field. In contrast, the so-called Fiske steps (FS) are found only when a magnetic field is applied [31].

* References 22-46 are given in the following section, Literature cited.

THE JOSEPHSON OSCILLATOR

An overlap-geometry Josephson tunnel junction consists of two superconductive metal layers (for example Nb and Pb) separated by a thin insulating oxide layer (Nb_xO_y) of uniform thickness (t_{ox}) that is small enough to permit quantum-mechanical tunnelling of electrons. The geometry is shown in Fig. 1. The region where the two superconducting layers overlap has the length L in the X-direction and the width W in the Y-direction. Typical values are $L \sim 6\lambda_J$ and $W \sim 0.8 \lambda_J$ where the Josephson length $\lambda_J \approx 10^{-4}$ m. Thus the overlap region is approximately 1-dimensional.

The tunnelling supercurrent is described by the two basic Josephson equations

$$j(X,T) = j_0 \sin\phi \tag{1}$$

and

$$\frac{\partial\phi}{\partial T} = \frac{2e}{\hbar} V . \tag{2}$$

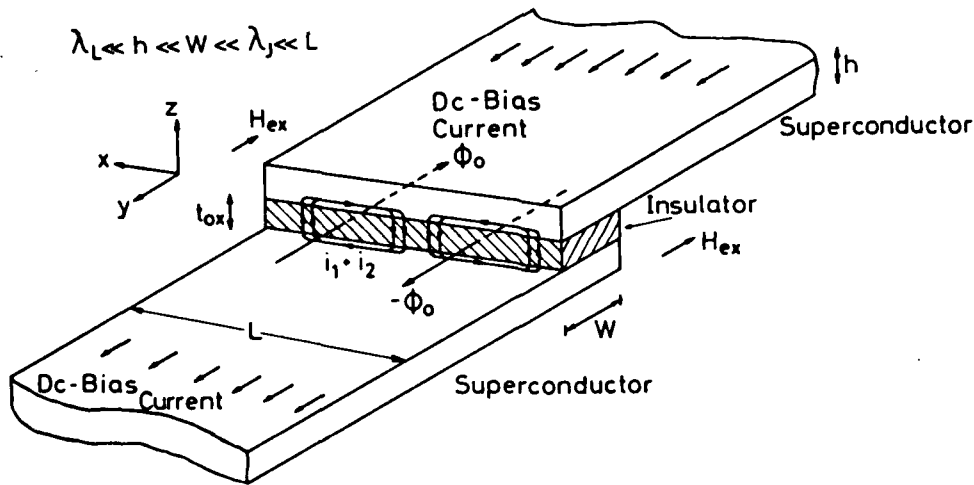


Figure 1. Josephson junction of overlap geometry [32].

Here $\phi = \phi(x, T)$ is the difference between the phases of the order parameter of the two superconductors, T is laboratory time, and $j(x, T)$ is the Josephson current crossing the barrier per unit length in the X -direction, j_0 being the maximum current. The voltage drop across the insulating barrier is $V = V(x, T)$. Combination of (1) and (2) with Maxwell's equations yields the following partial differential equation

$$(L_P/R_P)\phi_{XXT} + \phi_{XX} - L_P \phi_{TT} - GL_P \phi_T = (2\pi L_P j_0 / \phi_0) (\sin\phi - j_B / j_0) \quad (3).$$

Here L_P and R_P are inductance and skin resistance per length unit of the oscillator. (Figure 2 shows the equivalent circuit diagram for the oscillator). The capacitance and the effective normal resistance per length unit are represented by C and G^{-1} , respectively. The externally applied bias current per length unit is j_B , while $\phi_0 = h/2e = 2.064 \times 10^{-15}$ Wb is the magnetic flux quantum. Introduction of normalized coordinates, $x = X/\lambda_J$ and $t = T\omega_0$, yields the perturbed sine-Gordon equation:

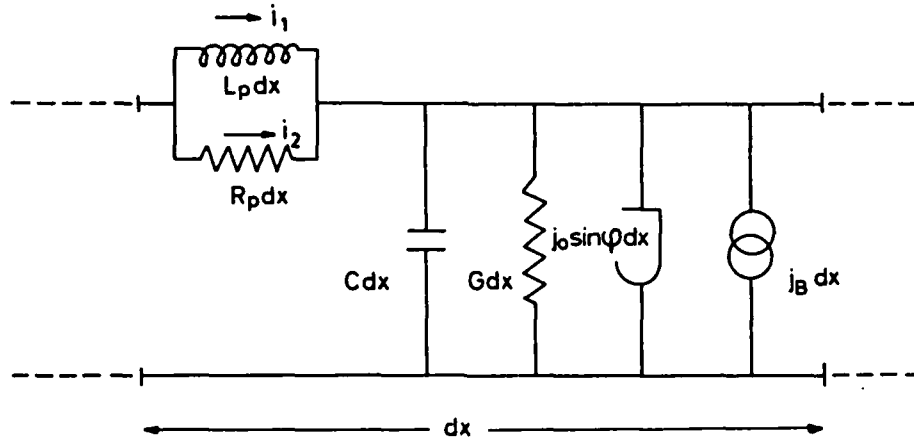


Figure 2. Element of lumped transmission line equivalent circuit representing the Josephson oscillator [32].

$$\phi_{xx} - \phi_{tt} - \sin\phi = \alpha\phi_t - \beta\phi_{xxt} - \gamma \quad (4).$$

Here the Josephson length and the Josephson plasma frequency are given by $\lambda_J = (\phi_0/2\pi j_0 L_P)^{1/2}$ and $\omega_0 = (2\pi j_0/\phi_0 C)^{1/2}$, and the coefficients in (4) are given by $\alpha = G/\omega_0 C$, $\beta = \omega_0 L_P/R_P$ and $\gamma = j_B/j_0$. Typical values of λ_J and ω_0 are $\lambda_J = 1.6 \times 10^{-4}$ m and $\omega_0 = 5.8 \times 10^{10}$ s⁻¹ such that the propagation velocity of electromagnetic signals (i.e. solutions of the linear wave equation, $\phi_{xx} - \phi_{tt} = 0$, corresponding to (4)) becomes $c = \lambda_J \omega_0 = 9.3 \times 10^6$ m/s in laboratory coordinates for a typical Josephson oscillator. In the normalized coordinates, x and t , this velocity is of course equal to unity.

At the ends of the oscillator, $X = 0$ and $X = L$, we apply the following boundary conditions:

(i) When no external magnetic field is applied we approximate the physical situation by an open-end condition, i.e. zero current on the junction at the ends. Since the current is proportional to ϕ_x we get

$$\phi_x(0,t) = \phi_x(\ell,t) = 0 \quad (5a)$$

in normalized units with $\ell = L/\lambda_J$. Condition (6) is only an approximation since coupling between the oscillator and the surrounding microwave circuit is neglected. However, the condition leads to good agreement between the computational results obtained for this condition and the experimental measurements.

(ii) When an external magnetic field H_{ex} in the negative Y-direction (see Fig. 1), is present the boundary condition becomes

$$\phi_x(0,t) = \phi_x(\ell,t) = \eta \quad (5b)$$

where η is the normalized magnetic field $\eta = (-W/j_0 \lambda_J) H_{ex}$.

The initial conditions used for the computational modelling of the oscillator are

$$\phi(x,0) = F(x) \quad \phi_t(x,0) = G(x) \quad (6)$$

where the functions F and G are chosen such that the stationary soliton dynamic states of the oscillator are obtained in the numerical computations without too long transients. In the following section we shall discuss these soliton dynamic states. In principle the initial conditions can be varied within certain limits without any change in the resulting stationary soliton dynamic states. In practice we often use the final values from a previous numerical solution of a boundary value problem (4), (5) and (6) with a slightly changed set of parameters. The five parameters in the model are α , β , γ , ℓ and η .

THE DYNAMICS OF THE JOSEPHSON OSCILLATOR

The classical sine-Gordon equation,

$$\begin{aligned} \phi_{xx} - \phi_{tt} - \sin\phi &= 0, \text{ has } 2\pi\text{-kinks and anti-kinks} \\ \phi(x,t) &= 4 \tan^{-1}[\exp(\pm(x - ut - x_0)/\sqrt{1 - u^2})] \end{aligned} \quad (7)$$

as soliton solutions [33]. Here u is the constant velocity of the soliton and x_0 is the position of the soliton at $t = 0$.

The perturbed sine-Gordon equation (4) has similar soliton solutions in the looser sense. Each soliton carries a magnetic flux quantum. The dynamics of these solitons is investigated by means of perturbation theory in Ref. [34]. As a result a first-order differential equation for the variable soliton velocity for a single soliton, $u(t)$, is derived

$$\frac{du}{dt} = \pm \frac{1}{4} \pi \gamma (1 - u^2)^{3/2} - \alpha u (1 - u^2) - \frac{1}{3} \beta u . \quad (8)$$

Eq. (8) expresses the balance between energy input in the system due to the γ -term and dissipation due to the loss terms, $\alpha\phi_t$ and $-\beta\phi_{xxt}$. The stationary velocity, u_∞ , is determined from Eq. (8) by letting $du/dt = 0$ and solving the resulting equation with respect to u . In typical computer experiments $u(t)$ rapidly adjusts towards the stationary velocity, u_∞ .

For a finite junction with open-end boundary conditions (5a) it is easy to show that solitons are reflected into antisolitons and vice versa at the boundaries. The bias current, γ , drives the soliton in the negative x -direction until it is reflected into an antisoliton at $x = 0$. The antisoliton is driven in the positive x -direction and reflected into a soliton at $x = \ell$ and a new cycle of this stationary state is initiated. We shall designate such a stationary state a soliton dynamic state. The periodic motion of the soliton on the oscillator is responsible for the emission of electromagnetic radiation, typically in the GHz-range, from the oscillator. Figure 3 shows a computer picture of part of the oscillation cycle in the soliton dynamic state with one soliton. In the inset, $\phi_t(\ell, t)$ is shown as a function of t for 50 time units. This quantity is proportional to the voltage on the oscillator at the end at $x = \ell$ according to (2). The DC-component of the voltage $\phi_t(\ell, t)$ has been computed for different values of the applied bias current γ in Eq. (4). The resulting curve shows agreement with experimentally measured 1st ZFS branch of the IV-characteristic as seen in Fig. 4. Similarly when two or three solitons are present on the oscillator the 2nd ZFS and the 3rd ZFS branches of the IV-characteristic are obtained.

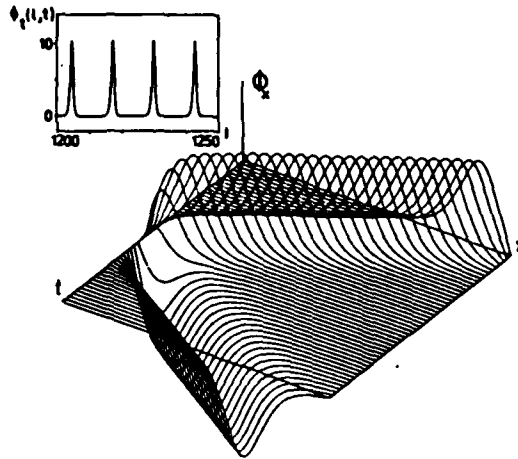


Figure 3. Computer solution of the perturbed sine-Gordon equation (4) with $\alpha = 0.05$, $\beta = 0.02$, $\gamma = 0.35$. Boundary conditions (5a) with $\ell = 6$. Initial conditions (6) with one soliton. The inset shows $\phi_t(\ell, t)$ [32].

Computational Fourier analysis of $\phi_t(\ell, t)$ provides the power spectrum for the radiation from the oscillator. The basic frequency is given by

$$f = u/2\ell . \tag{9}$$

Also the computational power spectrum shows agreement with experimental measurements of the power spectrum [35-36].

The presence of the loss term $-\beta\phi_{xxt}$ in Eq. (4) permits soliton dynamic states in which two or more solitons travel together in bunches [34].

Figure 3 illustrates the 2-soliton case for different parameter values. For small values of γ (Fig. 3a) the two solitons travel in a symmetric configuration - i.e. soliton and antisoliton in opposite directions. For higher values of γ (Fig. 3b) the two solitons travel in a bunched state - i.e. two solitons in the same direction followed by two antisolitons in the opposite direction. There is a gradual transition from the symmetric state to the 2-bunch state as the bias current γ is increased and vice versa as γ is decreased. In Ref. [37] it has been shown that the Hamiltonian for two (undeformed) solitons (on an infinite junction) has a local minimum for a finite separation between the solitons. This separation equals the length of the junction for the value of γ at which the transition between the two soliton dynamic states occurs. Ref. [32] reports on the following hysteresis phenomenon: For increasing (decreasing) bias current γ the transition from symmetric to bunched mode (vice versa) occurs at smaller (higher) values of γ .

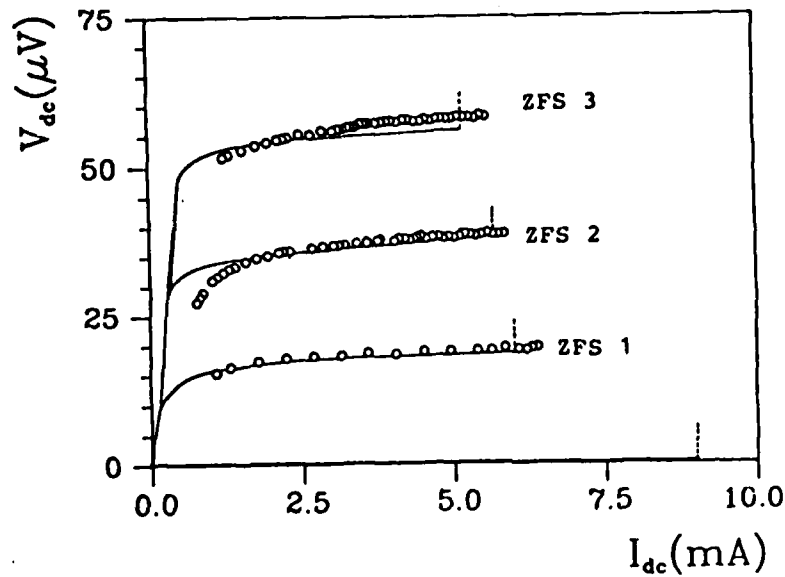


Figure 4. DC-voltage versus applied bias current showing the first three zero field steps. Circles indicate computational results and solid lines represent experimental results [32]. For the numerical results we have used $\alpha = 0.05$ and $\beta = 0.02$ in (4), $\lambda = 6$ and $\eta = 0$ in (5), and one, two and three solitons in the initial conditions (6) on ZFS 1, ZFS 2, and ZFS 3, respectively. Furthermore $\gamma \sim I_{dc}$ and $\langle \phi_t(0,t) \rangle \sim V_{dc}$.

Fig. 6 shows the soliton trajectories in the xt -plane corresponding to different soliton dynamic states. The diagram ZFS 1 corresponds to Fig. 3. while the diagrams ZFS 2 (Symmetric) and ZFS 2 (2-Bunch) correspond to Fig. 5a and b. The diagrams marked ZFS 3 (3-Bunch) and ZFS 3(2-Bunch, 1 Free) correspond to soliton dynamic states found experimentally and computationally in Ref. [36] where, respectively, three solitons travel in one bunch, and two solitons travel together and one soliton travels alone with a slightly deviating velocity, u . The soliton dynamic states corresponding to the other diagrams in Fig. 6 will be discussed in the following sections which treat the results obtained under the present contract work.

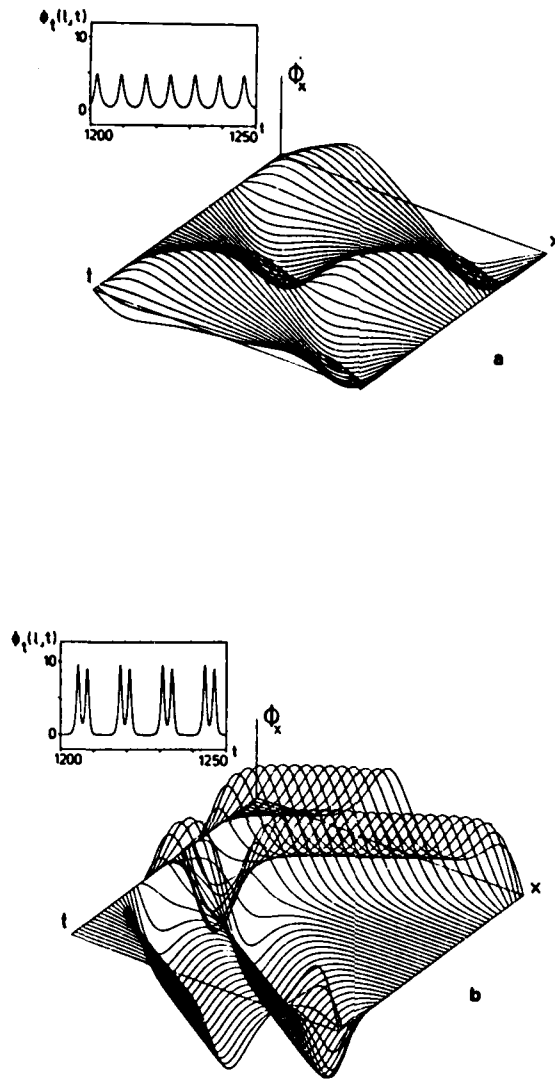


Figure 5. Computer solutions of the perturbed sine-Gordon equation (3) with $\alpha = 0.05$ and $\beta = 0.2$. Boundary conditions (5a) with $l = 6$. Initial conditions (6) with two solitons. (a): $\gamma = 0.125$, (b): $\gamma = 0.3$. The insets show $\phi_t(l, t)$ [32].

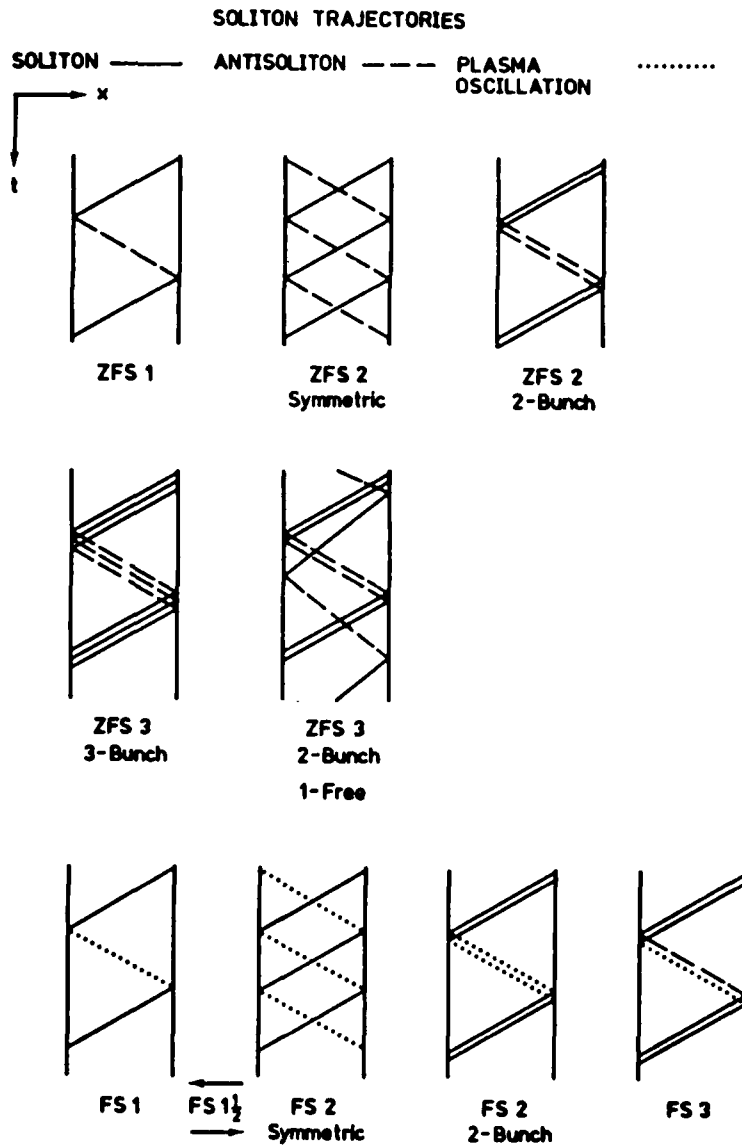


Figure 6. Soliton dynamic states. ZFS = zero field-step corresponding to boundary conditions (5a). FS = Fiske step corresponding to boundary conditions (5b).

LINEWIDTH OF ELECTROMAGNETIC RADIATION FROM JOSEPHSON OSCILLATOR

In the frequency spectrum of the electromagnetic radiation from the Josephson oscillator the width of the lines is very narrow. An experimental measurement shows a physical linewidth as narrow as 1 kHz of a line at 10 GHz [38]. The very well-defined frequency of the radiation is a technologically important feature of the Josephson junction. The narrow linewidth is a consequence of the coherence of the solitonic excitation of the junction.

In Ref. [1] of the present contract soliton perturbation theory is used to calculate the soliton oscillator linewidth arising from soliton interactions with background radiation. The paper treats the line oscillator illustrated in Fig. 1 and modelled by Eqs. (4-6) as well as the ring oscillator illustrated in Fig. 2 of Ref. [1]. In the latter case the boundary conditions (4) are replaced by the periodic boundary conditions

$$\begin{aligned} \phi_t(0,t) &= \phi_t(\ell,t) \\ \phi_x(0,t) &= \phi_x(\ell,t) \end{aligned} \tag{10}$$

where ℓ now denotes the circumference of the ring oscillator. The perturbation analysis is based on the ansatz that the soliton is given by

$$\phi_0 = 4 \tan^{-1} \exp [(x - X(t)) / \sqrt{1 - \dot{x}^2}] \tag{11}$$

where $X = X(t)$ describes the soliton trajectory in the xt -plane and the derivative $u = \dot{X}(t)$ is the velocity. Following the analysis of Ref. [34] the perturbation theory is expanded to second order. Detailed calculations in the case of an oscillator that is long compared with the Josephson length and for which the radiation field is thermal establish lower bounds for the linewidth of a real oscillator. These lower bounds are not in disagreement with available instrument-limited measurements of X-band linewidths less than 5 kHz. Fig. 3 and 4 of Ref. [1] show the experimentally measured linewidths as function of the average soliton velocity and the absolute temperature of the junction while Fig. 5 shows the computational linewidth at temperature $T = 3$ K and velocity $u = 0.8$.

A Hamiltonian perturbation theory was developed for the ring oscillator in Ref. [6]. Here the ansatz for the travelling wave was given by

$$\phi = \sin^{-1} [\pm \text{cn}(\xi, k)] \tag{12}$$

where $\xi = (x-ut)/k(1-u^2)^{1/2}$ and $\text{cn}(\xi, k)$ is a jacobian elliptic function with modulus k . ϕ given by (12) is an exact solution to the unperturbed sine-Gordon equation $\phi_{xx} - \phi_{tt} - \sin\phi = 0$ with periodic boundary conditions (10). The perturbation theory was developed for the elliptic function in the same manner as in Ref. [34]. As a result an ordinary differential equation like (8) was obtained. However, the coefficients γ , α and β were replaced by

$$\begin{aligned}\gamma' &= 2\gamma k^3/\Delta \\ \alpha' &= 2\alpha k^2 E(k)/\Delta \\ \beta' &= 2\beta [(2 - k^2)E(k) - 2(1 - k^2)K(k)]/\Delta\end{aligned}\tag{13}$$

with

$$\Delta = 2k^2 E(k) + (1 - k^2) \ell^2 4K(k) .$$

Here $K(k)$ and $E(k)$ denote the complete elliptic integrals of first and second kind. The stationary velocity was determined as function of circumferential length for different values of loss parameters α and β and as function of bias γ . Comparison to direct numerical solutions shows that Hamiltonian perturbation theory can be used to predict the stationary one-soliton velocity of the ring oscillator. The results are useful for the interpretation of experimental measurements of the I-V characteristic for this device. Furthermore the stationary solutions are useful as initial conditions for numerical simulations of the ring oscillator under different circumstances.

In Ref. [11] very detailed simulation studies of the dynamics in long ring oscillators under the influence of external microwave radiation field and internal thermal noise are presented. The former situation is modelled by inclusion of a sinusoidal driving term in the perturbed sine-Gordon equation (4) where $-\gamma$ is replaced by $\gamma + \eta(x,t)$ with $\eta(x,t) = \eta(t) = \eta_0 \sin \Omega t$, Ω being the frequency and η_0 the amplitude. The latter case is modelled by letting $\eta(x,t)$ be Gaussian white noise with zero mean $\langle \eta(x,t) \rangle = 0$ and autocorrelation function

$$R_\eta(\zeta, \tau) = \langle \eta(x,t) \eta(x + \zeta, t + \tau) \rangle = \sigma_\eta^2 \delta(\zeta) \delta(\tau)\tag{14}$$

Here the variance of the noise σ_η^2 is connected with the loss α and the absolute temperature T through

$$\sigma_\eta^2 = 4\pi \alpha k_B T / \phi_0 j_0 \lambda_J\tag{15}$$

where k_B is the Boltzmann constant. The simulation algorithm uses a pseudo spectral method making heavy use of fast Fourier transforms which is well adapted to vector processors (CRAY-1-S) which gives a speed-up factor in computing time of typically 22 in comparison to conventional high-speed computers, and also provides results with a relative accuracy of less than 10^{-8} which is required to study the very narrow linewidth of such oscillators. For the sinusoidal driving term the computational results are compared to results obtained by perturbation theory based on the ansatz

$$\phi(x,t) = \phi^k(x,t) + \phi^\infty(t)\tag{16}$$

where $\phi^k(x,t)$ denotes the kink part and $\phi^\infty(t)$ denotes the background part. In the theory the background motion becomes an effective driving term for the momentum of the kink part. As a result the kink momentum is determined as a function of time and thus the fluctuations in the kink velocity and in the revolution frequency. Since the velocity u fluctuates Eq. (9) is replaced by

$$\int_{t_{n-1}}^{t_{n-1} + T_n} u dt = \ell \quad (17)$$

and

$$f_n = 1/T_n$$

where T_n is the n 'th revolution period. We compare the standard deviation of the revolution frequency

$$\sigma_f = [\langle (f_n - \langle f_n \rangle)^2 \rangle]^{1/2} \quad \text{for } 0.4 \leq \Omega \leq 2.0.$$

The results are shown in Fig. 8 of Ref. [11]. The perturbative kink model predicts a resonance just below the plasma frequency $\Omega = 1$, whereas the numerical simulation yields this peak at a somewhat lower frequency. The reason for the discrepancy is attributable to the fact that we have used a linearized kink model. Presumably, the use of a higher order expansion would yield a behavior analogous to that of a soft nonlinear spring, thus reducing the discrepancy. It has also been shown later that the difference in scale of the standard deviation can be removed by a further refinement of the perturbative treatment [39].

For the Gaussian white noise driving term the numerical simulation results agree well with experimental results. The model based on Hamiltonian perturbation theory was also able to predict the qualitative dependence of the standard deviation σ_f on the bias.

In Ref. [7] standard methods of stochastic processes are used to study the coupling of the sine-Gordon system with a heat reservoir. Both phonons and solitons are found to be thermalized in a way such that the phonons will have an average energy at $k_B T$ per mode while solitons will have an energy of $\frac{1}{2} k_B T$. These results are in agreement with those obtained by using a statistical-mechanics approach for a "dilute" solution gas [40].

EFFECTS OF EXTERNAL MAGNETIC FIELDS ON SOLITON DYNAMICS

In Ref. [4] the dynamical behavior of solitons propagating in the presence of an applied magnetic field on a long overlap-geometry Josephson tunnel junction is investigated. The application of external magnetic fields is essential for tuning the frequency of the radiation. The magnetic field is modelled by boundary conditions (5b). It is demonstrated that the soliton dynamic state corresponding to the branch of the IV-characteristic for the oscillator denoted the 1st Fiske step (FS 1) is the following: The soliton travels in the bias-aided direction which is the negative x-direction in the FS 1 diagram in Fig. 6 and reacts with the boundary condition (5b) at $x = 0$. As a result energy is absorbed from the incident soliton such that the minimum energy for the sine-Gordon soliton ($= 8$ in normalized units) is no longer available. Therefore no antisoliton is reflected. Instead reflection of plasma oscillations is observed. They travel in the positive x-direction and reach the boundary at $x = \ell$ where a new soliton is created due to the energy input caused by boundary condition (5b). This constitutes the first cycle of the stationary soliton dynamic state. For the initial conditions used in this paper the 2nd Fiske step which contains two solitons is not found, while the 3rd Fiske step (FS 3 in Fig. 6) is found to consist of two solitons travelling in the negative x-direction and one antisoliton and plasma oscillations travelling in the positive x-direction. Analyses of the corresponding of the three first harmonics of the computational power spectra confirm this picture of the soliton dynamics for the junction biased on FS 1 and FS 3.

Ref. [3] demonstrates that the 1st Fiske step possesses a branched structure. The major portion of the step corresponds to a simply periodic soliton oscillation whereas the branches are characterized by subharmonic generation. Such period doublings are important because they may be the first step on the road to chaos. Indeed such chaotic behavior is found by us for overlap Josephson junctions when the oscillator is subjected to a constant external magnetic field [5]. The phenomenon will be discussed in the following section.

In Ref. [2] the soliton dynamics for different geometries of the Josephson tunnel junction are compared. So far we have only been concerned with the overlap geometry illustrated in Fig. 1. In the in-line geometry the bias current enters in the direction parallel to the long dimension (instead of perpendicular to the long dimension) of the junction and is limited by self-screening effects to the two ends of the junction. In the paper I-V characteristics and microwave emission spectra are calculated for the two geometries and shown to be qualitatively similar, although also quantitative differences are found.

Ref. [9] is a detailed study of I-V structure and the emitted X-band radiation from the overlap-geometry Josephson tunnel junctions of intermediate length ($\ell = 2$) when external magnetic fields are applied. Direct computational solutions of the perturbed sine-Gordon equation (4) with inhomogeneous boundary conditions (5b) are compared to experimental measurements. Furthermore cavity mode analyses, both single mode and

multimode, are shown to predict the simulation results quite accurately. This result is important because the application of a superposition of linear cavity modes is computationally cheaper than direct numerical solution of the boundary value problem of the partial differential equation. The method works for intermediate length Josephson junctions. For longer junctions the soliton nature of the excitation becomes more important and must be included in the expansion modes.

Fig. 1 in Ref. [9] gives some of the main results of the paper. For small values of the magnetic field η the junction is biased on ZFS 1 while larger values of η leads to a soliton dynamic state corresponding to the 2nd Fiske step. Both FS 2 symmetric and FS 2 2-Bunch (indicated in Fig. 6) are found. In the former case solitons and plasma oscillations are travelling in opposite directions on the junction at the same time. In the latter case two solitons are travelling in a bunch together and reflected into plasma oscillations. Thus we have demonstrated the existence of the bunching phenomenon [32] also in the magnetic case. For $\eta \lesssim 1.8$ Fig. 1 shows the bias value at the top of the 1st zero field step and the bias value at the bottom of this step as function of the magnetic field. The top decreases and the bottom increases as the magnetic field is increased. At $\eta \approx 1.8$ ZFS 1 no longer exists. For $1.8 \lesssim \eta \lesssim 5.5$ the junction operates on FS 2 in the symmetric mode or in the bunched mode as illustrated in the insets of the figure. On FS 2 it is only possible to detect the top bias value of the step. As indicated by the arrows in Fig. 1 the stationary values of the bias current depend on the direction of the field variation. A similar hysteresis phenomenon was found in the non-magnetic case [32]. The figure also shows the agreement between the results obtained by direct numerical solution and the results obtained by the single mode theory due to Kulik [41], up to $\eta \approx 4.4$, and the results obtained by the multimode theory due to Enpuku et al. [42].

Ref. [9] contains numerous computations of time series for the voltage at one end of the junction, power spectra, and dependence of frequency components on bias and magnetic fields (illustrated in Figs. 2-9).

Experimental measurements, shown in Fig. 10-12, agree well with the computational results. In particular, it was found experimentally that the first frequency component was missing in the interval in the magnetic field strength where the junction operates on FS 2. Here the power in the first harmonic was found computationally to be very low.

SOLITON AND CHAOS EFFECTS ON THE JOSEPHSON OSCILLATOR

As mentioned earlier the little distorted coherent solitonic excitation of the Josephson oscillator is the reason for the narrow linewidth of the electromagnetic radiation from the device. Chaotic features in the nonlinear dynamics of the oscillator may change this picture. In particular, a combination of random thermal effects and chaotic effects

may have serious effects on the frequency spectrum. Thus it is desirable for the technological applications to avoid operation of the oscillator in the regions of parameter space $(\ell, \alpha, \beta, \gamma, \eta)$ where these phenomena occur. In Ref. [5] we have found a region where chaotic intermittency between soliton dynamic states occurs. It is, however, only a relatively narrow window. The junction considered has $\lambda = 5$, $\alpha = 0.252$, $\beta = 0$, and the magnetic field is $\eta = 0.25$. For $\gamma = 0.454$ the junction is biased on FS 1 while for $\gamma = 0.5$ the junction is biased on FS 2. For intermediate γ -values ($\gamma = 0.456-0.490$) the oscillator was observed computationally to switch between FS 1 and FS 2 intermittently, giving rise to a special branch in the IV-characteristic which we denoted FS 1½ as indicated in Fig. 6. Long computer simulations of the phenomenon made a detailed study of the power spectrum possible and also demonstrated that the switching can be treated probabilistically as a Poisson process. Experimental measurements [43] have in fact perhaps revealed FS 1½.

For the study of chaos it is necessary to possess analytical and computational tools for the detection of the phenomenon. We have worked with the Painlevé test [44] and developed software for computation of return maps. In Ref. [12] we apply these tools to a periodically driven rf superconducting quantum interference device (SQUID) consisting of a ring with a single Josephson junction. The system is described by the ordinary differential equation

$$\phi'' + \epsilon \phi' + \sin \phi = a(\gamma \sin \omega_D t - \phi) \quad (18)$$

Here prime denotes differentiation with respect to time, ϵ is a loss parameter, ω_D is the driving frequency and $a\gamma$ the amplitude. The perturbing term, $a\phi$, has the effect of confining the chaos. As a result an almost 1-dimensional return map is found. The very delicate structure of the dynamics as well as the existence of coexisting attractors are demonstrated.

Besides detection of chaos prediction of the phenomenon is important. Available here is the method of Melnikov integrals [45]. So far the method has only been developed for ordinary differential equations that possess a homoclinic orbit. In Ref. [14] we apply the method to the following equations with linear and quadratic damping terms, $\epsilon a\phi'$ and $k(\phi')^2$,

$$\begin{aligned} \phi'' + \sin \phi &= \epsilon(r + r_1 \sin \omega_D t - a\phi') \\ \phi'' + k(\phi')^2 + \sin \phi &= \rho + \rho_1 \sin \omega_D t, \end{aligned} \quad (19)$$

respectively. The differential operators on the left hand sides possess homoclinic orbits in phase space. The right hand sides are the perturbative terms giving rise to Smale horseshoe chaos when the Melnikov integral vanishes. In the case of quadratic damping the existence of an exact solution to $\phi'' + k(\phi')^2 + \sin \phi = 0$ makes it possible to avoid the inclusion of the damping term into the perturbation. The Melnikov prediction of chaos becomes correspondingly more accurate as is demonstrated by comparison to numerical solutions of (19).

OTHER RESEARCH IN CONNECTION WITH THE PRESENT CONTRACT

In connection with the physical understanding of the soliton phenomena in the sine-Gordon system the mechanical analogue consisting of elastically coupled pendula subjected to gravity [46] plays an important role. In Ref. [13] a mechanical analogue for the double-sine-Gordon equation

$$\phi_{xx} - \phi_{tt} - \lambda_1 \sin \phi - \frac{\lambda_2}{2} \sin \frac{\phi}{2} = 0 \quad (20)$$

is proposed and used to analyze solitary solutions for arbitrary parameter values. Eq. (20) applies to other condensed matter systems.

For the numerical solution of nonlinear evolution equations like the sine-Gordon equation it is a fundamental question to perform the discretization in an optimal manner. Ref. [8] investigates this question in the case where the evolution equation is integrable. A geometrical approach is used to obtain a discretization that preserves the integrability. As an illustrative example the discrete Burger's hierarchy is analyzed. The possibility of extending this procedure to soliton equations which are also integrable is briefly discussed.

PERSPECTIVES

The work done in the present contract is being continued under the following main themes:

Instabilities of the steps in the I-V characteristics for the Josephson junction. For optimal operation of the Josephson oscillator it is important to understand the instabilities of the soliton dynamic states. For example why does the spatially uniform excitation of the junction become unstable for values of the bias current which are larger than a certain critical value? As a result a spatial structure is formed (one soliton on ZFS 1, two solitons on ZFS 2, etc.). And why does this structure become unstable again at larger values of the bias current such that the step has a maximum height?

Chaos and noise rise due to thermal effects. The relationship between these effects is of crucial importance for the narrow linewidth properties of the Josephson oscillator.

Modal expansions for longer Josephson junctions. Computational costs have been reduced considerably by using cavity mode expansions for intermediate length Josephson junctions. Can a similar reduction of simulation costs be achieved for long Josephson junctions by using expansions in terms of nonlinear soliton modes from the unperturbed system?

Coupling problems. For the practical application of Josephson oscillators in thin film electronic networks the coupling between the oscillator, other oscillators and surrounding microstrips is essential. The dynamics of the junction equipped with boundary conditions modelling such couplings is very important.

LITERATURE CITED

References [1-21] which are parts of the present contract work, are listed on pages 4 - 6.

- [22] T.A. Fulton and R.C. Dynes, *Solid State Commun.* 12, 57 (1973).
- [23] T.A. Fulton and L.M. Dunkleberger, *Rev. Phys. Appl.* 9, 299 (1974).
- [24] K. Nakajima, Y. Onodera, T. Nakamura, and R. Sato, *J. Appl. Phys.* 45, 4095 (1974).
- [25] K. Nakajima, T. Yamashita, and Y. Onodera, *J. Appl. Phys.* 45, 3141 (1974).
- [26] S.N. Ern  and R.D. Parmentier, in *Proceedings of the 1980 Applied Superconductivity Conference*, IEEE Trans. Mag. MAG-17, 804 (1981); *J. Appl. Phys.* 51, 5025 (1980); 52, 1091 (1981).
- [27] M. Cirillo, R.D. Parmentier, and B. Savo, *Physica D3*, 565 (1981).
- [28] B. Dueholm, O.A. Levring, J. Mygind, N.F. Pedersen, O.H. Soerensen, and M. Cirillo, *Phys. Rev. Lett.* 46, 1299 (1981).
- [29] G. Costabile, A.M. Cucolo, S. Pace, R.D. Parmentier, B. Savo, and R. Vaglio, in *SQUID-80*, edited by H. D. Hahlbohm and H. Lubbig (de Gruyter, Berlin, 1980), p. 147; S.N. Ern , A. Ferrigno, R.F. Finnegan, and R. Vaglio, in *Proceedings of the Sixteenth International Conference on Low Temperature Physics*, Los Angeles, 1981, *Physica B + C*, 108, 1301 (1981).
- [30] J.T. Chen, T.F. Finnegan, and D.N. Langenberg, in *Proceedings of the International Conference on Superconductivity*, Stanford, 1969, edited by F. Chilton (North-Holland, Amsterdam, 1971), p. 413; *Physica* 55 413 (1971); J.T. Chen and D.N. Langenberg, in *Proceedings of the Thirteenth International Conference on Low Temperature Physics*, LT13, 1972, edited by K.D. Timmerhaus, W.J. Sullivan, and E.F. Hammel (Plenum, New York, 1974), Vol. 3, p. 289.
- [31] D.D. Coon and M.D. Fiske, *Phys. Rev.* 138, A744 (1965).
- [32] P.S. Lomdahl, O.H. Soerensen and P.L. Christiansen, *Phys. Rev. B* 25, 5737 (1982).
- [33] A.C. Scott, F.Y.F. Chu and D.W. McLaughlin, *Proc. IEEE*, 61, 1443 (1973).
- [34] D.W. McLaughlin and A.C. Scott, *Phys. Rev. A* 18, 1652 (1978).

- [35] P.L. Christiansen, P.S. Lomdahl, A.C. Scott, O.H. Soerensen, and J.C. Eilbeck, *Appl. Phys. Lett.* 39, 108 (1981).
- [36] P.S. Lomdahl, O.H. Soerensen, P.L. Christiansen, A.C. Scott, and J.C. Eilbeck, *Phys. Rev. B* 24, 7460 (1981).
- [37] T.H. Soerensen, P.L. Christiansen and P.S. Lomdahl, *Phys. Lett* 89 A, 308 (1982).
- [38] E. Joergensen, V.P. Koshelets, R. Monaco, M.R. Samuelson, and M. Salerno, *Phys. Rev. Lett.* 49, 1093 (1982).
- [39] M. Fordsmand and P.L. Christiansen (to appear).
- [40] A.R. Bishop, J.A. Krumhansl and S.E. Trullinger, *Physica (Utrecht)* 1D, 1 (1980).
- [41] O. Kulik, *Zh. Tekn. Fiz.* 37, 157 (1967) [*Sov. Phys. - Techn. Phys.* 2, 111 (1967)].
- [42] K. Enpuku, K. Yoshida, and F. Irie, *J. Appl. Phys.* 52, 344 (1981).
- [43] M. Cirillo, G. Costabile, S. Pace, R.D. Parmentier, and B. Savo, *Proceedings LT-17, Part II* (eds. U. Eckern, A. Schmied, H. Weber, and H. Wühl) North-Holland, Amsterdam, p. 1131 (1984).
- [44] M.J. Ablowitz, A. Ramani, and H. Segur, *J. Math. Phys.* 21, 715 (1980).
- [45] V.K. Melnikov, *Moscow Math. Soc.* 12, 1 (1963).
- [46] A.C. Scott, *Am. J. Phys.* 37, 52 (1969).

Linewidth for fluxon oscillators

Mario Salerno* and Alwyn C. Scott

Center for Nonlinear Studies, Los Alamos National Laboratory, Los Alamos, New Mexico 87545

(Received 19 March 1982)

Soliton perturbation theory is used to calculate the fluxon oscillator linewidth arising from fluxon interaction with background radiation. Detailed calculations in the case of an oscillator that is long compared with the Josephson length and for which the radiation field is thermal establish lower bounds for the linewidth of a real oscillator. These lower bounds are not in disagreement with recent, instrument-limited measurements of X-band linewidths less than 5 kHz.

I. INTRODUCTION

In 1973 Fulton and Dynes pointed out that the "zero-field steps" observed in the voltage-current characteristics of long Josephson junctions could be ascribed to oscillatory behavior of internal fluxons (or magnetic solitons).¹ Subsequent observations of microwave radiation² led to the hope that such structures could play a technically useful role as oscillators into the millimeter wave range.³ Recently, some long Josephson junctions of high quality were fabricated and tested at the University of Salerno⁴ and sent to the Physikalische Technische Bundesanstalt in Berlin⁵ and the Technical University of Denmark^{6,7} for detailed measurements in the microwave range. Comparison of these microwave measurements with numerical and analog computations of fluxon dynamics (based on a structurally perturbed version of the sine-Gordon equation)⁸ confirms that the original idea of Fulton and Dynes is correct.

Among other results emerging from these experimental studies has been the observation of a surprisingly narrow oscillator linewidth: less than 5 kHz (the instrument limit) at a fundamental oscillator frequency of 10 GHz.⁷ Our aim in this paper is to present a theory of fluxon oscillator dynamics which allows us to predict the linewidth of a long Josephson junction oscillator.

Our approach is based upon the description of a Josephson transmission line as the sine-Gordon equation with structural perturbations that represent dissipation and input of energy.^{9,10} We extend a recently developed soliton perturbation theory¹¹ to second order in a small parameter proportional to the structural perturbations in order to calculate the effect of background radiation on soliton dynamics.¹² This calculation allows us to define an "instantaneous frequency" which leads

directly to an explicit formula for oscillator linewidth as a function of the background radiation in the junction. Such background radiation may be generated in several ways: (i) electrical noise conducted to the oscillator through bias and output leads, (ii) radiation generated by spatial inhomogeneities of the junction, (iii) radiation generated during reflection of a fluxon from the end of the junction, and (iv) thermal noise in the cavity modes of the junction. To obtain a lower bound on oscillator linewidth, we assume the radiation field to be entirely thermal noise. Under this assumption, and with some simplifications, we calculate suitably normalized values for linewidth as a function of temperature and average fluxon velocity. The worst (i.e., largest) value of linewidth that we calculate under these assumptions is less than the instrument-limited value of 5 kHz.⁷

Although the work reported here is related to recent studies of chaotic behavior in the sinusoidally driven nonlinear pendulum and sine-Gordon equation,¹³ we emphasize that our results depend upon the assumption that the trajectory of the fluxon oscillation is not trapped in a region of phase space that contains a "strange attractor."¹⁴ The above-mentioned numerical studies⁸ support this assumption.

II. DESCRIPTION OF OSCILLATORS

Our analysis of fluxon oscillators is based upon a previously developed theoretical model for the Josephson transmission line^{9,10} (JTL), which is briefly recapitulated here for the convenience of the reader. Figure 1 shows a transmission line equivalent circuit¹⁵ for JTL in which L is series inductance per unit length (pul) related to superconducting surface currents, R is series resistance pul

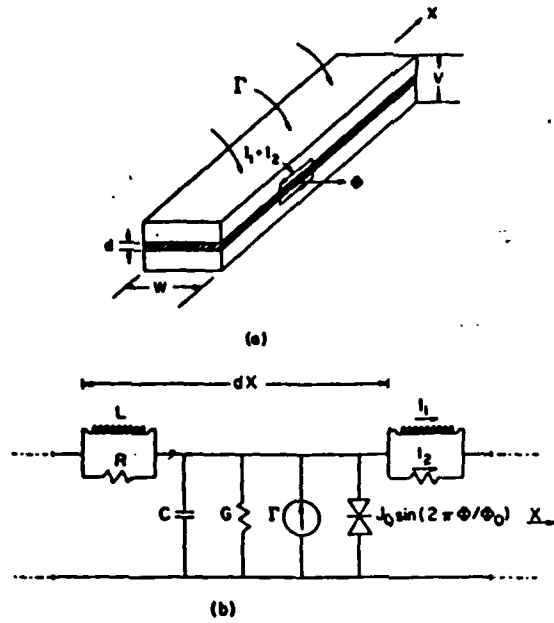


FIG. 1. (a) Physical model of the JTL (not to scale). (b) Transmission line equivalent circuit of the JTL.

related to normal surface currents, C is shunt capacitance pul related to electric field in the junction, G is shunt conductance pul related to normal electron conduction across the junction, Γ is an externally imposed bias current pul, and, finally, $J_0 \sin(2\pi\Phi/\Phi_0)$ is the Josephson current pul crossing the junction. Kirchhoff's equations for this JTL model lead to the following partial differential equation for transverse voltage (V):

$$\frac{L}{R} \Phi_{xT} + \Phi_{xx} - LC\Phi_{TT} - GL\Phi_T = J_0 L \sin(2\pi\Phi/\Phi_0) + \Gamma L, \quad (1)$$

where X and T are laboratory space and time, $\Phi_0 = h/2e$ is the flux quantum, and

$$\Phi \equiv \int V dT. \quad (2)$$

Series inductance (L) and shunt capacitance (C) are related to junction geometry by

$$L = \mu_0 \frac{2\lambda_L + d}{W} \quad (3)$$

and

$$C = \epsilon \frac{W}{d}, \quad (4)$$

where λ_L is "London" penetration depth for surface currents, W is junction width, d is thickness of the barrier region, ϵ is dielectric permittivity for the

barrier, and $\mu_0 (=4\pi \times 10^{-7} \text{ H/m})$ is the magnetic susceptibility of free space.

For analysis it is convenient to normalize these variables as follows:

$$\phi = 2\pi\Phi/\Phi_0, \quad (5)$$

$$x = X/\lambda_J, \quad (6)$$

$$t = T/\tau_J, \quad (7)$$

where λ_J is the "Josephson" penetration length and

$$\tau_J \equiv \lambda_J \sqrt{LC}. \quad (8)$$

With these normalizations, velocity is measured in units of

$$u_0 = \lambda_J/\tau_J = 1/\sqrt{LC}, \quad (9)$$

and (1) becomes

$$\phi_{xx} - \phi_{tt} - \sin\phi = \alpha\phi_t - \beta\phi_{xx} + \gamma, \quad (10)$$

where

$$\alpha \equiv GL/\tau_J, \quad (11a)$$

$$\beta \equiv L/R\tau_J, \quad (11b)$$

$$\gamma \equiv 2\pi L\Gamma/\Phi_0\lambda_J^2. \quad (11c)$$

With α , β , and $\gamma=0$, (10) is recognized as the sine-Gordon equation with the exact soliton solution¹⁶

$$\phi = 4 \tan^{-1} \left[\exp \left\{ \pm \frac{x-ut}{(1-u^2)^{1/2}} \right\} \right], \quad (12)$$

which represents the propagation of a magnetic flux quantum or "fluxon" along the junction. To make a fluxon oscillator, one must design a physical path over which the fluxon can execute periodic motion. Two examples are shown in Fig. 2. In the "line oscillator" [Fig. 2(a)], a fluxon approaches one end, is reflected as an antifluxon [change of sign in (12)], propagates to the other end, and is reflected as a fluxon, etc. In the "ring oscillator" [Fig. 2(b)] the fluxon proceeds at constant velocity around the ring. In our calculations, an important parameter is the total path, l , over which the fluxon travels to complete a cycle of oscillation normalized to λ_J . Thus for the *line oscillator* [Fig. 2(a)]

$$l = \frac{2a}{\lambda_J} \quad (13)$$

while for the *ring oscillator* [Fig. 2(b)]

$$l = \frac{2\pi R}{\lambda_J}. \quad (14)$$

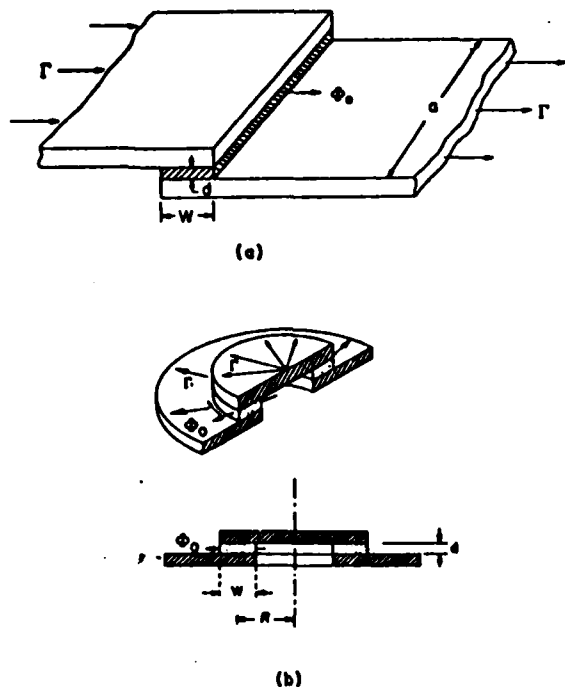


FIG. 2. (a) Line oscillator. (b) Ring oscillator.

The effect of the term γ in (10) is to pump energy into the fluxon motion while the α and β terms dissipate energy. In the following section we use soliton perturbation theory to calculate effects of these terms on the motion.

III. OUTLINE OF PERTURBATION APPROACH

The approach to sine-Gordon soliton perturbation analysis in Ref. 11 begins with a nonlinear equation

$$N\bar{\phi} = \epsilon f(\bar{\phi}), \quad (15)$$

where $N\bar{\phi} = 0$ is a completely integrable (i.e., "soliton") equation $\bar{\phi} = \text{col}(\phi, \phi_1)$, where

$$\text{col}(x, y) \equiv \begin{pmatrix} x \\ y \end{pmatrix},$$

and ϵ is a small parameter. Expanding

$$\bar{\phi} = \bar{\phi}_0 + \epsilon \bar{\phi}_1 + \epsilon^2 \bar{\phi}_2 + \dots \quad (16)$$

one finds that

$$N\bar{\phi}_0 = 0, \quad (17)$$

so $\bar{\phi}_0$ is an exact multisoliton solution which depends upon certain constant parameters p_j (e.g., the

speeds and positions of the solitons). Thus

$$\bar{\phi}_0 = \bar{\phi}_0(x, t, \{p_j\}). \quad (18)$$

If $\bar{\phi}_1$ and $\bar{\phi}_2$ are secular (i.e., grow linearly in time) the second and third terms on the right-hand side (RHS) of (16) are useful only for times of order ϵ^{-1} and ϵ^{-2} , respectively. To overcome this objection one can allow order ϵ time variations in the p_j 's of $\bar{\phi}_0$ so $\bar{\phi}_1$ and $\bar{\phi}_2$ satisfy

$$L\bar{\phi}_1 = \bar{F}_1(\bar{\phi}_0), \quad (19)$$

$$L\bar{\phi}_2 = \bar{F}_2(\bar{\phi}_0, \bar{\phi}_1), \quad (20)$$

where \bar{F}_1 and \bar{F}_2 acquire extra terms because of the modulations of the p_j 's, and L is a linearization of N around $\bar{\phi}_0$. Now secular growth of $\bar{\phi}_1$ and $\bar{\phi}_2$ can be avoided by requiring that

$$\bar{F}_1 \perp \mathcal{N}_d(L^\dagger), \quad (21)$$

$$\bar{F}_2 \perp \mathcal{N}_d(L^\dagger), \quad (22)$$

where $\mathcal{N}_d(L^\dagger)$ is the discrete null space of the adjoint of L . From (21) and (22) one obtains ordinary differential equations (ODE) for the order ϵ and order ϵ^2 variations in the p_j 's.

The strategy of our calculation is as follows. Order ϵ corrections obtained from (21), are used to calculate the effects of α , β , and γ terms in (10) on the steady motion of a JTL fluxon. The radiation field $\bar{\phi}_1$ is then determined from (19). This permits us to evaluate the orthogonality condition (22) which gives ODE's that determine the effects of $\bar{\phi}_1$ (radiation field) on the fluxon motion. In our picture it is this interaction of the fluxon motion with the radiation field that leads to an instantaneous frequency and therefore to a nonzero oscillator linewidth.

Our analysis proceeds as follows (see Ref. 11 for details). The exact single fluxon solution (12) of the unperturbed sine-Gordon equation is modified to

$$\phi_0 = 4 \tan^{-1}[\exp(\zeta)], \quad (23)$$

where

$$\zeta \equiv \gamma(t)[x - X(t)]. \quad (24)$$

Thus $X(t)$ specifies the trajectory of the fluxon and $\gamma(t)$ its relativistic contraction. Two elements of $\mathcal{N}_d(L^\dagger)$ are

$$\bar{b}_1 \equiv \begin{bmatrix} \phi_{0,n} \\ -\phi_{0,t} \end{bmatrix} \quad (25)$$

and

$$\bar{b}_2 \equiv \begin{bmatrix} \phi_{0,xt} \\ -\phi_{0,x} \end{bmatrix}. \quad (26)$$

The conditions $\bar{F}_1 \bar{b}_1$ and $\bar{F}_1 \bar{b}_2$ imply

$$\gamma = \frac{1}{(1 - \dot{X}^2)^{1/2}}. \quad (27)$$

Thus, for typographical convenience, we define

$$\dot{X} \equiv u. \quad (28)$$

The time dependence of \dot{X} is divided into order ϵ contributions, calculated from (21), and order ϵ^2 contributions, calculated from (22). Thus

$$\dot{X} = \dot{X}_1 + \dot{X}_2, \quad (29)$$

where

$$\begin{aligned} \ddot{X}_1 = & -\frac{\epsilon}{4}(1-u^2)^{3/2} \\ & \times \int_{-\infty}^{\infty} f(\phi_0(\zeta)) \operatorname{sech} \zeta d\zeta, \end{aligned} \quad (30)$$

$$\begin{aligned} \ddot{X}_2 = & \frac{\epsilon^2}{4}(1-u^2)^{3/2} \\ & \times \int_{-\infty}^{\infty} [f(\phi_1) - \frac{1}{2}\phi_1^2 \sin \phi_0] \operatorname{sech} \zeta d\zeta. \end{aligned} \quad (31)$$

IV. GENERAL CALCULATION OF LINEWIDTH

From the results of the previous section we see that, under steady-state oscillator conditions, the fluxon speed is

$$\dot{X} = u_c + u_p(t), \quad (32)$$

where u_c is a constant (power balance) velocity. The time-varying component u_p arises from interaction of the fluxon with the radiation field and, from (30) and (31) obeys the ODE

$$\dot{u}_p = \ddot{X}_2 - \langle \ddot{X}_2 \rangle_{av}, \quad (33)$$

where $\langle \rangle_{av}$ indicates a time average.

If $u_p = 0$, the fluxon executes a perfectly periodic motion over a path l with frequency

$$v_c = u_c / l. \quad (34)$$

$$\ddot{X}_2 = \frac{1}{4}(1-u^2)^{3/2} \int_{-\infty}^{\infty} [\alpha f(\eta\phi_1) + (1-u^2)(\eta\phi_1)^2 \tanh \zeta \operatorname{sech} \zeta] \operatorname{sech} \zeta d\zeta, \quad (39)$$

where α is a small parameter that measures the structural perturbation, and η is a small parameter that measures the amplitude of the radiation field.

In the following analysis we make two simplify-

In general we can define a (time-dependent) instantaneous frequency as

$$v(t) = v_c + u_p / l. \quad (35)$$

The rms derivation of $v(t)$ from its mean value v_c is

$$\Delta v = \{ \langle [v(t) - v_c]^2 \rangle_{av} \}^{1/2}. \quad (36)$$

We take Δv as a convenient measure of oscillator linewidth. Since the radiation field in (31) is not periodic we take the average in (36) over a long time as

$$\Delta v = \left[\lim_{T \rightarrow \infty} \frac{1}{T} \int_0^T dt [v(t) - v_c]^2 \right]^{1/2}. \quad (37)$$

Equation (37), together with (35) and (31), provides a straightforward procedure for calculating the linewidth of a fluxon oscillator. We do this for a particular example in the following section.

V. THERMAL LINEWIDTH OF A SINGLE FLUXON OSCILLATOR

We now turn to a practical question of fluxon oscillator design: calculation of linewidth when the radiation field is assumed to be in thermal equilibrium with its environment. This calculation neglects other sources of the radiation field (electrical noise, radiation emitted from the fluxon, etc.) thus it should give a lower bound for realizable linewidths and some idea about how the linewidth depends upon oscillator parameters and temperature. The analysis is restricted to a single fluxon oscillation to avoid analytical difficulties associated with the phenomena of "bunching."⁸

We employ (31) where, from (10),

$$\epsilon f(\phi_1) \equiv \alpha \left[\phi_{1,t} - \frac{\beta}{\alpha} \phi_{1,xx} + \frac{\gamma}{\alpha} \right], \quad (38)$$

thus α is our small parameter in the perturbation analysis. Since we are assuming that the radiation field arises because the linear modes of the oscillator are in thermal equilibrium, (31) takes the form

ing assumptions:

$$\beta = 0 \quad (40)$$

and

$$l \gg 1. \quad (41)$$

The first of these is not a serious restriction if one assumes a somewhat larger value of α to account for dissipation in the β term of (38).

$$\eta\phi_1 = \sum_n \frac{A_n}{\sqrt{2\pi}} \frac{\sqrt{1-u^2}}{\omega_n - uk_n} \left[\frac{k_n - u\omega_n}{\sqrt{1-u^2}} \cos(k_n x - \omega_n t) - \sin(k_n x - \omega_n t) \tanh \left[\frac{x - ut}{\sqrt{1-u^2}} \right] \right], \quad (42)$$

where

$$k_n^2 = \omega_n^2 - 1 \quad (43a)$$

and

$$k_n = \frac{2\pi n}{l}. \quad (43b)$$

Since the second term in the integral (39) is an odd function of ξ while the first term is even, the contribution of the second term is small except when $n \simeq l$. Then the ratio of the first to second term is of order l and, under assumption (41), we can neglect the second term. Thus (39) takes the form

$$\ddot{X}_2 = \frac{\alpha}{4} (1-u^2)^{3/2} \int_{-\infty}^{\infty} \left[\eta\phi_{1,t} + \frac{\gamma}{\alpha} \right] \text{sech}\xi d\xi. \quad (44)$$

The term γ/α in (44) merely contributes a constant to \ddot{X}_2 which is absorbed in the power balance condition that determines u_c . Thus it does not enter into our calculation of Δv .

The component of \ddot{X}_2 that depends on the radiation field is

We calculate the thermal radiation field $\eta\phi_1$ as a sum of individual photon modes of a cavity which contains a single fluxon moving with constant velocity u .¹⁷ Thus

$$\ddot{X}_{2R} = \sum_n \alpha C_n \cos[(k_n u - \omega_n)t + \theta_n], \quad (45)$$

where

$$C_n = \frac{u^2(1-u^2)^{3/2}}{4\sqrt{2\pi}} \frac{k_n A_n}{(k_n u - \omega_n)} \times \text{sech} \left[\frac{\pi k_n}{2} (1-u^2)^{1/2} \right] \times \exp[-\pi k_n (1-u^2)^{1/2}]. \quad (46)$$

To calculate the mode amplitudes $\{A_n\}$, we assume a mode at frequency ω_n to have the energy

$$E_n = \frac{\hbar\omega_n}{\exp\left[\frac{\hbar\omega_n}{k_B T} - 1\right]}. \quad (47)$$

Strictly speaking, the relation between E_n and A_n should be calculated for a cavity containing a fluxon; however, from inequality (41) this relation is the same as that for an empty cavity. Thus in normalized units

$$A_n = \left[\frac{8\pi\hbar u_0 k_n \omega_n / n \Phi_0^2}{\left| \exp\left[\frac{\hbar\omega_n}{k_B T \tau_j}\right] - 1 \right| \left[\frac{k_n^2}{L} + C u_0^2 \omega_n^2 + \frac{2eJ_0 \lambda_j^2}{\hbar} \right]} \right]^{1/2}. \quad (48)$$

From (48), (45), and (37) we obtain

$$\frac{\Delta v}{\alpha} = \frac{u^2(1-u^2)^{3/2}}{2\sqrt{2}\Phi_0 l} \sqrt{\hbar u_0} \times \left[\sum_n \frac{1}{n} \frac{\omega_n k_n^4 \left| \text{sech} \left[\frac{\pi}{2} k_n (1-u^2)^{1/2} \right] \exp[-k_n \pi (1-u^2)^{1/2}] \right|^2}{\left| \exp\left[\frac{\hbar\omega_n}{k_B T \tau_j}\right] - 1 \right| \left[\frac{k_n^2}{L} + C u_0^2 \omega_n^2 + \frac{2eJ_0 \lambda_j^2}{\hbar} (k_n u - \omega_n)^2 \right]} \right]^{1/2}. \quad (49)$$

Equation (49) is the main result of this paper. To appreciate the dependence of linewidth $\Delta\nu$ upon oscillator parameters and temperature that it implies, we turn to two examples of JTL that have been thoroughly studied.¹⁰ Important parameters are recorded in Table I. From these parameters we have plotted in Figs. 3 and 4 $l\Delta\nu/\alpha$ as a function of u for several values of temperature and l . Since these calculations are rather insensitive to l (see Fig. 5) we can assume $\Delta\nu \propto l^{-1}$. We see that $\Delta\nu(u)$ rises to a maximum value at

$$u \approx 0.8 \quad (50)$$

and, as we expect, falls to zero in limits $u \rightarrow 0$ and 1. The main difference between N25L and N53C is in the value for λ_J , but this has a relatively small effect upon $\Delta\nu$. We find, of course, that $\Delta\nu$ falls with decreasing temperature, but it is interesting to observe that the curves $\Delta\nu(u)$ show little change in shape.

Ducholm *et al.*⁷ have reported an instrument-limited measurement that

$$\Delta < 5, \quad (51)$$

where Δ is the linewidth (in units of kHz) for a line oscillator with

$$\alpha = 0.01,$$

$$l = 12.$$

From our calculation the thermal linewidth in laboratory units is given by $\Delta\nu/\tau_J$. Assuming $l = 12$ [i.e., $a/\lambda_J = 6$ in Fig. 2(a)] we find for N25L that the maximum linewidth is equal to 260 Hz and for N53C, the maximum linewidth is equal to 550 Hz. These results are not inconsistent with (51).

VI. CONCLUDING DISCUSSION

The main result of this paper is (49) which gives $\Delta\nu/\alpha$ as a function of the oscillator parameters where l is the total fluxon path length for a cycle of oscillation, measured in units of λ , u is the average

TABLE I. Josephson transmission lines.

Parameter	N25L	N53C	Unit
α	0.0052	0.00555	
u_0	2.3×10^7	1.76×10^7	m/s
L	2.1×10^{-9}	2.5×10^{-9}	H/m
C	0.9×10^{-6}	1.3×10^{-6}	F/m
λ_J	1.27×10^{-3}	2.63×10^{-4}	m
J_0	9.7×10^{-2}	1.9	A/m
τ_J	0.55×10^{-10}	1.5×10^{-11}	s

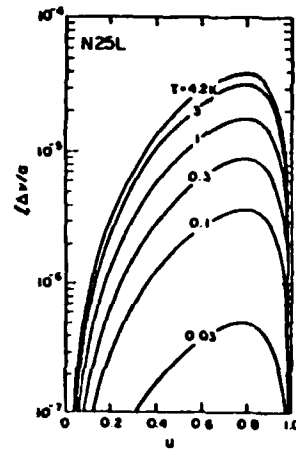


FIG. 3. Normalized thermal linewidth as a function of average fluxon velocity and absolute temperature for JTL No. N25L.

fluxon speed normalized to u_0 ($=\lambda_J/\tau_J$), and T is the absolute temperature, in addition to the JTL parameters λ_J , τ_J , C , L , and J_0 defined in Sec. II.

From (49) the rms deviation of the oscillator linewidth is equal to $\Delta\nu/\tau_J$ Hz, where α measures the shunt oscillator losses (including loading). In deriving (49) the following assumptions have been made:

- (1) only a single fluxon is present in the cavity,
- (2) $l \gg 1$,
- (3) the background radiation field is entirely thermal, and
- (4) surface losses [$\beta\phi_{ext}$ in (10)] are neglected.

Thus our calculations give a lower bound for the linewidth to be found in a real oscillator. Additional contributions to oscillator linewidth may arise

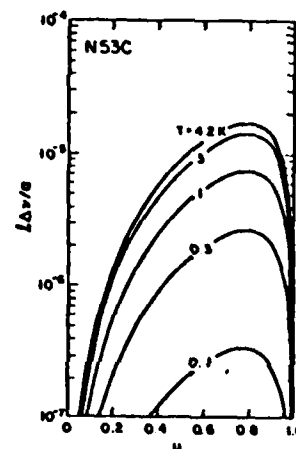


FIG. 4. Same as Fig. 3 for JTL no. N53C.

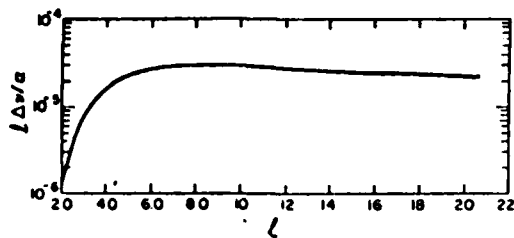


FIG. 5. $\Delta v/v$ vs v for $T=3$ K, and $u=0.8$.

from excess electrical noise and radiation from the fluxon itself.

Equation (44) shows an exact mechanism for influence of electrical noise on the fluxon motion through stochastic behavior of the bias current γ . A line oscillator may have larger linewidth than a corresponding ring oscillator because the kink-antikink reflection that take place in a line oscillator generate an additional component of radiation¹⁸ that is not present in a ring oscillator. Since we see

no special difficulties in making ring oscillators, we suggest that they be considered experimentally.

Finally, Figs. 3 and 4 show Δv rising to a maximum value around $u=0.8$. Although this result is obtained for thermal linewidth, we feel that this behavior should be found when a more general radiation field is present. An experimental check of this suggestion should be possible with instrumental resolution of linewidth only an order of magnitude better than that reported in Ref. 7.

ACKNOWLEDGMENTS

It is a pleasure to thank E. Jen for assistance with the numerical calculations and M. R. Samuelson for interesting theoretical discussions. One of us (M.S.) appreciates support from the Ansaldo Company, Genoa, Italy, and by the United States Army through its European Research Office.

*On research leave from the Department of Physics, University of Salerno, Italy. Presently visiting The Laboratory of Applied Mathematical Physics, Technical University of Denmark, DK-2800 Lyngby, Denmark.

¹T. A. Fulton and R. C. Dynes, *Solid State Commun.* **12**, 57 (1973); T. A. Fulton, in *Superconducting Applications: SQUIDS and Machines*, edited by B. B. Schwartz and S. Foner, (Plenum, New York, 1977), p. 125.

²J. T. Chen and D. N. Langeberg, in *Proceedings of the 13th International Conference on Low Temperature Physics—LT13*, edited by K. D. Timmerhaus, W. J. O'Sullivan, and E. F. Hammel (Plenum, New York, 1974), Vol. 3, p. 289; T. A. Fulton and L. N. Dunklenberger, *Rev. Phys. Appl.* **2**, 299, 1974; T. F. Finnegan, J. Toots, and J. Wilson, in *Proceedings of the 14th International Conference on Low Temperature Physics—LT 14*, edited by M. Krusius and M. Vuorio (North-Holland, Amsterdam, 1975), Vol. 4, p. 184.

³R. D. Parmentier and G. Costabile, *Rocky Mount. J. Math.* **8**, 117, (1978); G. Costabile, R. D. Parmentier, B. Savo, D. W. McLaughlin, and A. C. Scott, *Appl. Phys. Lett.* **32**, 587 (1978).

⁴G. Costabile, A. M. Cucolo, S. Pace, R. D. Parmentier, B. Savo, and R. Vaglio, in *SQUIDS and Their Applications*, edited by H. D. Hahlbohm and H. Lubbig (W. de Gruyter, Berlin, 1980), p. 147; A. M. Cucolo, R. Monaco, S. Pace, R. D. Parmentier, B. Savo, and R. Vaglio, in *Proceedings of the 16th International Conference on Low Temperature Physics—LT16*, edited by W. G. Clark [*Physica 107B+C*, 547 (1981)]; A. M. Cucolo, S. Pace, R. Vaglio, V. Lacquaniti, and G.

Marullo, *IEEE Trans. Magn.* **17**, 812 (1981).

⁵S. N. Ern , A. Ferrigno, T. F. Finnegan, and R. Vaglio, in *Proceedings of the 16th International Conference on Low Temperature Physics—LT16* [*Physica 108B+C*, 1301 (1981)].

⁶B. Ducholm, O. A. Levring, J. Mygind, N. F. Pedersen, O. H. Soerensen, and M. Cirillo, *Phys. Rev. Lett.* **46**, 1299 (1981).

⁷B. Ducholm, E. Joergensen, O. A. Levring, J. Mygind, N. F. Pedersen, M. R. Samuelson, O. H. Olsen, and M. Cirillo, in *Proceedings of the 16th International Conference on Low Temperature Physics—LT16* [*Physica 108B+C*, 1303 (1981)].

⁸K. Nakajima, T. Yamashita, and Y. Onodera, *J. Appl. Phys.* **45**, 3141 (1974); K. Nakajima, Y. Onodera, T. Nakamura, and R. Sato, *J. Appl. Phys.* **45**, 4095 (1974); M. Cirillo, thesis, University of Salerno, 1979 (unpublished); S. N. Ern  and R. D. Parmentier, *J. Appl. Phys.* **51**, 5025 (1980) [see also **52**, 1091 (1981)]; M. Cirillo, R. D. Parmentier, and B. Savo, *Physica D* **3**, 565 (1981); P. L. Christiansen, P. S. Lomdahl, A. C. Scott, O. H. Soerensen, and J. C. Eilbeck, *Appl. Phys. Lett.* **39**, 108 (1981) [see also *Phys. Rev. B* **24**, 7460 (1981)]; O. H. Soerensen, P. S. Lomdahl, and P. L. Christiansen, in *Proceedings of the 16th International Conference on Low Temperature Physics—LT16* [*Physica 108B+C*, 1299 (1981)]; P. S. Lomdahl, O. H. Soerensen, and P. L. Christiansen, *Phys. Rev. B* **25**, 5737 (1982).

⁹A. C. Scott, *Am. J. Phys.* **37**, 52 (1969); *Nuovo Cimento* **69B**, 241 (1970).

¹⁰A. C. Scott, F. Y. F. Chu, and S. A. Reible, *J. Appl. Phys.* **47**, 3272 (1976).

- ¹¹D. W. McLaughlin and A. C. Scott, *Phys. Rev. A* **18**, 1652 (1978).
- ¹²This second order interaction is consistent with related results for the interaction a ϕ^4 kink with radiation by Y. Wada and J. R. Schrieffer [*Phys. Rev. B* **18**, 8 (1978)].
- ¹³B. A. Huberman, J. P. Crutchfield and N. H. Packard, *Appl. Phys. Lett.* **37**, 750 (1980); N. F. Pedersen and A. Davidson (unpublished); J. C. Eilbeck, P. S. Lomdahl and A. C. Newell, *Phys. Lett.* **87A**, 1 (1981); D. Bennett, A. R. Bishop, S. E. Trullinger (unpublished).
- ¹⁴E. Ott, *Rev. Mod. Phys.* **53**, 665 (1981); J. P. Eckmann, *ibid.* **53**, 643 (1981).
- ¹⁵A. C. Scott, *Active and Nonlinear Wave Propagation in Electronics* (Wiley-Interscience, New York, 1970).
- ¹⁶A. C. Scott, F. Y. F. Chu, and D. W. McLaughlin, *Proc. IEEE* **61**, 1443 (1973).
- ¹⁷J. Rubinstein, *J. Math. Phys.* **11**, 258 (1970).
- ¹⁸M. Salerno, *Phys. Lett.* **87A**, 116 (1981).

Subharmonic generation in Josephson junction fluxon oscillators biased on Fiske steps

M. P. Soerensen, P. L. Christiansen, R. D. Parmentier,^{a)} and O. Skovgaard
Laboratory of Applied Mathematical Physics, The Technical University of Denmark, DK-2800 Lyngby, Denmark

(Received 22 November 1982; accepted for publication 1 February 1983)

Numerical integration of the perturbed sine-Gordon equation describing a long overlap-geometry Josephson junction in a magnetic field indicates a branched structure of the first Fiske step. The major portion of the step corresponds to a simply periodic fluxon oscillation whereas the branches are characterized by subharmonic generation.

PACS numbers: 74.50. + r, 85.25. + k, 84.20.Pc, 84.30.Ng

The dynamics of fluxons on long Josephson tunnel junctions has recently attracted considerable interest. Fluxon propagation has clearly been demonstrated to be responsible for the appearance of zero-field steps (ZFS)¹⁻³ and indicated as being associated also with the appearance of Fiske steps (FS)⁴⁻⁶ in the current-voltage (I - V) characteristics of such long junctions. Moreover, associated with this propagation there is an emission of microwave radiation of very narrow linewidth from the ends of the junction,⁷ suggesting the possibility of interesting electronic applications.

In this letter we report on detailed numerical investigations of a perturbed sine-Gordon model of a long Josephson junction in a magnetic field. The results that have emerged give further confirmation to the fluxon propagation mechanism as being responsible also for the FS and, more importantly, show a branching of the first FS in the I - V plane with the presence of subharmonic generation on the branches.

The mathematical model studied is³

$$\phi_{xx} - \phi_{tt} - \sin \phi = \alpha \phi_t - \gamma, \quad (1a)$$

$$\phi_x(0,t) = \phi_x(L,t) = \eta. \quad (1b)$$

Here, ϕ is magnetic flux normalized to $\hbar/2e$, x the longitudinal distance normalized to the Josephson penetration depth λ_J , and t the time normalized to the inverse of the Josephson plasma frequency ω_0 . The γ term represents a uniformly distributed bias current normalized to the maximum zero-voltage (Josephson) current I_0 appropriate to an overlap geometry.⁸ The term in α represents quasiparticle loss. The constant η is a normalized measure of the external magnetic field which determines the boundary conditions [Eq. (1b)] at the two ends of the junction of normalized length L . For this study $L = 5$, $\alpha = 0.252$, $\eta = 0.75$, and $0 < \gamma < 1$. These values were chosen to be similar to those used in Ref. 5. Equations (1a) and (1b) were integrated using the implicit finite difference method described in detail in Ref. 3, with the space and time intervals both set to 0.05. Numerical accuracy and stability were verified by halving and doubling the space and time intervals in the computations and by carrying out the integration for long periods of time ($t \sim 1500$) and observing that all measurable characteristics of the solutions remained stationary.

Two types of initial conditions were used: (i) a "smooth"

initial condition, defined as

$$\phi(x,0) = F(x,0) + G(x), \quad (2a)$$

$$\phi_t(x,0) = F_t(x,0), \quad (2b)$$

where

$$F(x,t) = 4 \tan^{-1} \{ \exp[(x - 2.5 + ut)/(1 - u^2)^{1/2}] \}, \quad (2c)$$

in which the velocity u ($0 < u < 1$) is chosen by a power balance calculation according to the value of γ , and $G(x)$ is a static solution of Eqs. (1a) and (1b) in which $\eta = 0.75 - F_x(0,0)$; (ii) a "tickled" initial condition, similar to (i) but with the further superposition of a packet of plasma oscillations, defined as

$$H(x,t) = A \cos(kx - \omega t) \exp[-(x - x_0)^2/W^2], \quad (3)$$

in which $k = 1$, $\omega^2 = 1 + k^2$, $0.1 < A < 0.2$, $1 < x_0 < 4$, and $0.1 < W < 0.2$.

The results presented refer to the situation with the junction biased on the first FS. Our most significant result is indicated in Fig. 1, which shows the I - V form, on an expanded scale, of this FS. Here, and in the following, voltage is defined as ϕ_t , which represents the physical voltage normalized to $\hbar\omega_0/2e$. In particular, in addition to the major portion of the step, similar to that observed by Ern e *et al.*,⁵ we observe two lateral branches. These branches are characterized by the generation of subharmonics in the radiation emit-

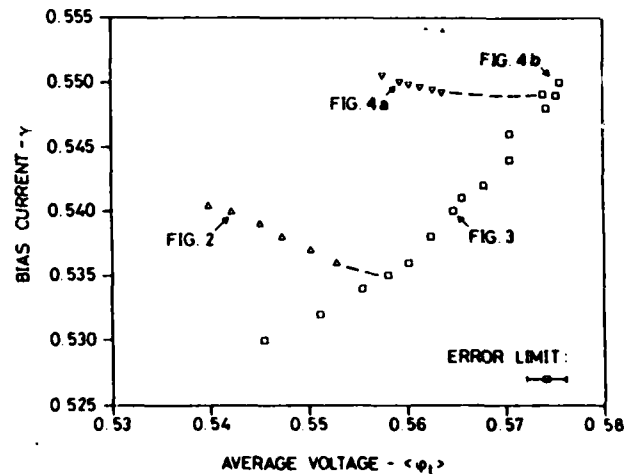


FIG. 1. Detail of current-voltage form of first Fiske step for $\eta = 0.75$. Rectangles: major portion, without subharmonic generation; triangles: lateral branches, with subharmonic generation.

^{a)} Permanent address: Istituto di Fisica, Universit  di Salerno, I-84100 Salerno, Italy.

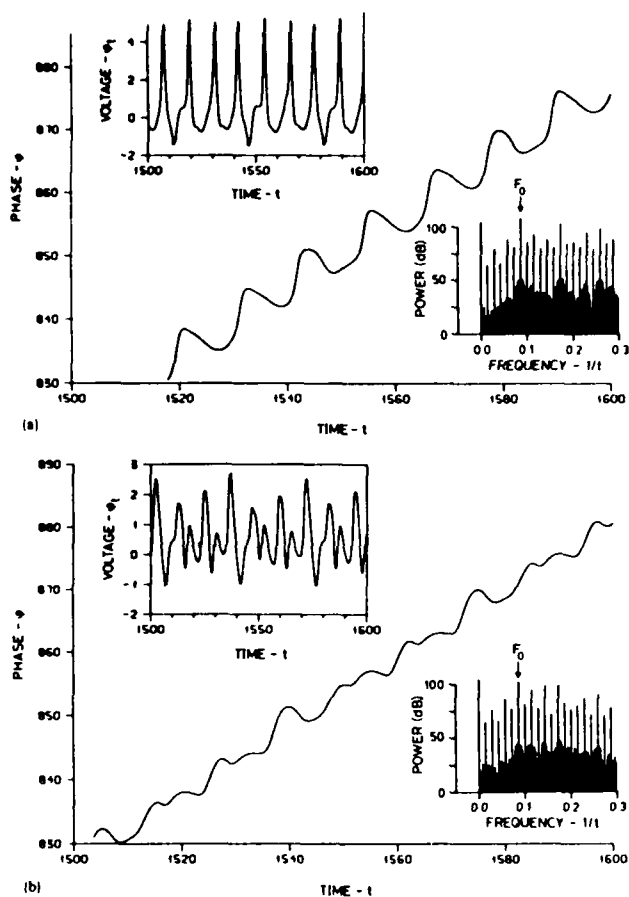


FIG. 2. Dynamics of lower subharmonic branch of first Fiske step for $\gamma = 0.54$, $\eta = 0.75$. Time evolution of phase ϕ , voltage ϕ , (upper inset), and power spectrum (lower inset). (a) Left junction end, (b) right junction end.

ted from the junction, whereas the major portion has no such subharmonic generation. Figures 2-4 indicate the detailed dynamics associated with the labeled points on the I - V characteristic of Fig. 1. In Figs. 2(a) and 2(b) we show the time evolution of the phase ϕ and the voltage ϕ , at the two ends of the junction and the related power spectra corresponding to a point on the lower branch. The power spectra were calculated as follows: Printouts of the time evolution of ϕ , were examined and a tentative maximum superperiod (highest-order subharmonic) established by eye. Time intervals of $\Delta t \sim 500$ of these waveforms, containing exactly an integral number of such superperiods, were then fast Fourier transformed using a simple rectangular window. For display purposes, all of the spectra have been normalized to an arbitrary value of $\phi^2 = 10^{-11}$. Solutions similar to those in Fig. 2 were invariably arrived at from "tickled" initial conditions. In this connection it is worth mentioning that the existence of the branches seems to depend only upon the fact of tickling and not upon the precise mode in which tickling is effected. This fact was established by varying the amplitude, width, and initial position of the tickling wave packet in the type (ii) initial condition and observing that the state into which the solution evolved did not change with these variations. As is apparent from Figs. 2(a) and 2(b), the fundamental period of oscillation is approximately 12 normalized time units. The

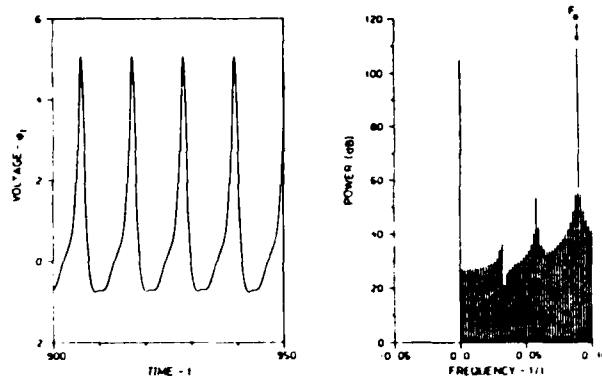


FIG. 3. Dynamics of major portion of first Fiske step for $\gamma = 0.54$, $\eta = 0.75$. Time evolution of voltage ϕ , and power spectrum at left junction end.

presence of the asymmetric fluxon propagation mechanism proposed in Ref. 4 is confirmed by the phase jump of 2π per fundamental period,⁵ and by the asymmetry between the time evolution at the left and right ends (note that the polarity of the magnetic field used here is opposite that used in Ref. 5, for which right and left are interchanged here with respect to that work). Particularly apparent from the insets of Fig. 2 is the strong subharmonic content of this oscillation. This is shown in detail in the power spectra of Figs. 2(a) and 2(b), which indicate the presence of third and sixth subharmonics as well as multiples of these. In contrast with the results of Fig. 2, when the "smooth" initial condition is employed with the same value of the bias, the simply periodic time evolution indicated in Fig. 3 is obtained. Although some subharmonic content is still present, it is very much reduced compared with that shown in Fig. 2.

In a similar way, higher up on the FS is a second branch of the I - V curve, the power spectra of the dynamics of which are indicated in Figs. 4(a) and 4(b). In Fig. 4(a), once again, subharmonic generation is observed, this time, however, with only a dominant second subharmonic. As before, the subharmonic branch of Fig. 4(a) evolves from the type (ii) initial condition, whereas the simply periodic solution of Fig. 4(b) evolves from the type (i) initial condition.

In physical terms, the major portion of the FS corresponds to a situation in which a fluxon propagates in the field-aided direction (here, from right to left), is reflected at the end as a localized plasmon moving in the opposite direction, which in turn is reflected at the other end as a fluxon which resumes propagating exactly as before.^{4,5} Propagation on the subharmonic branches is almost the same, except that perfect periodicity of the overall process is resumed only after a certain number of complete back-and-forth cycles. The reason for the existence of such multiple solutions for given parameter values is not understood, but the fact is consistent with the frequently noted experimental observation of fine structure on FS.⁹ In the experiments, wave packets may be created by thermal fluctuations or imperfections in the junction thus giving rise to creation of subharmonics.

Of considerable interest is the manner in which the solutions evolve as the bias parameter γ is varied in small increments during the computation. As we move along the

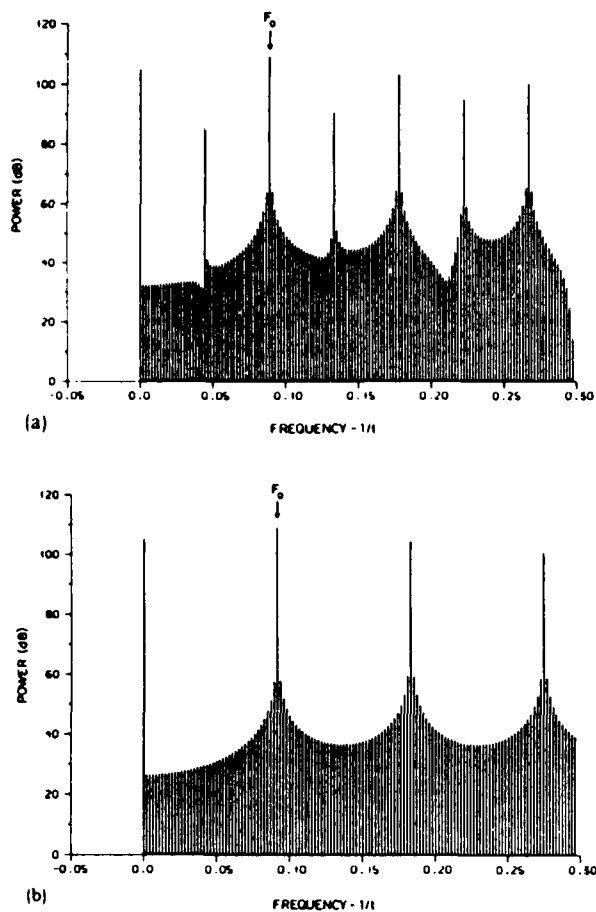


FIG. 4. Dynamics of first Fiske step. Power spectrum of ϕ , at left junction end for $\gamma = 0.55$ and $\eta = 0.75$. (a) Subharmonic branch, (b) major portion of first FS.

branches, the relative ratios of the subharmonic components vary; however, until we reach the juncture point of the branch with the major portion of the FS, motion along the branches is repeatable and reversible. Once the juncture

point is reached, however, a simply periodic solution corresponding to the major portion of the FS is maintained, which is also repeatable and reversible. The only way to proceed from the major portion of the FS to the branches is through tickling the solution, which causes a jump to the branch. This may be related to the fact, as is evident from Fig. 1, that the branches have negative differential resistance. When the bias is progressively increased on the lower branch, the junction switches abruptly from the branch to the major portion of the FS for $\gamma > 0.5407$. The same procedure on the upper branch leads to a jump to the third FS for $\gamma > 0.5505$. On the major portion of the step, the junction switches to the third FS for $\gamma > 0.550$ and to a static zero-voltage state for $\gamma < 0.528$. Finally, our results suggest the possible existence of further fine structure of the branches. This is presently being investigated.

We are pleased to thank A. C. Scott for helpful and stimulating discussions. The financial support of the Danish Natural Science Research Council under grant No. 11-3064 and of the European Research Office of the United States Army through contract No. DAJA37-82-C-0057 is gratefully acknowledged.

¹S. N. Ern  and R. D. Parmentier, *J. Appl. Phys.* **51**, 5025 (1980).

²B. Ducholm, O. A. Levring, J. Mygind, N. F. Pedersen, O. H. Soerensen, and M. Cirillo, *Phys. Rev. Lett.* **46**, 1299 (1981).

³P. S. Lomdahl, O. H. Soerensen, and P. L. Christiansen, *Phys. Rev. B* **25**, 5737 (1982).

⁴B. Ducholm, E. Joergensen, O. A. Levring, J. Mygind, N. F. Pedersen, M. R. Samuelsen, O. H. Olsen, and M. Cirillo, *Physica B* **108**, 1303 (1981).

⁵S. N. Ern , A. Ferrigno, and R. D. Parmentier (unpublished).

⁶M. Radparvar and J. E. Nordman, presented at the 1982 Applied Superconductivity Conference.

⁷E. Joergensen, V. P. Koshelets, R. Monaco, J. Mygind, M. R. Samuelsen, and M. Salerno, *Phys. Rev. Lett.* **49**, 1093 (1982).

⁸A. Barone, W. J. Johnson, and R. Vaglio, *J. Appl. Phys.* **46**, 3628 (1975).

⁹N. F. Pedersen (private communication).

Fluxon propagation and Fiske steps in long Josephson tunnel junctions

S. N. Erné and A. Ferrigno

Physikalisch-Technische Bundesanstalt, Institut Berlin, D-1000 Berlin 10, West Germany

R. D. Parmentier*

*Laboratory of Applied Mathematical Physics, The Technical University of Denmark,
DK-2800 Lyngby, Denmark*

(Received 15 September 1982)

The dynamical behavior of fluxons propagating in the presence of an applied magnetic field on an overlap-geometry Josephson tunnel junction of length $5\lambda_J$ having a McCumber $\beta_c = 5\pi$ is studied by numerical integration of the circuit equations of a 50-section lumped RSJ-type (resistive shunted junction) model. Resonant propagating configurations corresponding to the first and third Fiske steps are found. The fundamental frequencies and power levels of the radiation emitted from one end when the junction is biased on the first and third Fiske steps and on the first zero-field step are comparable, but a magnetic field renders the power spectra at the two ends of the junction different.

INTRODUCTION

The zero-field steps, or dc current singularities, that appear (also) in the absence of applied magnetic fields in the dc current-voltage characteristics of Josephson tunnel junctions which are long in one dimension with respect to the Josephson penetration length λ_J have by now been convincingly shown to be associated with the resonant propagation of fluxons in the junction,¹⁻³ according to the mechanism first proposed by Fulton and Dynes.⁴ In this picture the first zero-field step (ZFS), which has a voltage asymptote of $\Phi_0 \bar{c}/l$, where Φ_0 is the magnetic flux quantum, \bar{c} is the electromagnetic wave velocity within the junction, and l is the length of the junction, is due to the propagation back and forth along the junction of a single fluxon; the second ZFS, whose voltage asymptote is twice that of the first, is due to two fluxons, etc.

In addition to the ZFS, when a dc magnetic field is applied in the plane of a Josephson tunnel junction (either long or short), a second set of current steps, called Fiske steps (FS), is observed in the current-voltage characteristic. Successive FS occur with a voltage-asymptote spacing just half that of the ZFS. For short junctions, the theory of FS developed by Kulik⁵ quite satisfactorily accounts for experimental observations; however, this is no longer the case for long junctions.⁶ Extensions of Kulik's theory to long junctions, framed in terms of cavity-mode interactions, have been formulated by various authors.⁷⁻¹⁰ These analyses are intended to

be applicable to both FS and ZFS, and they have found varying degrees of success in explaining experimental observations.

The idea of applying the fluxon propagation model to the explanation of FS in long junctions was first suggested, but rejected as not physically feasible, by Fulton and Dunkleberger.¹¹ It was re-proposed, with an argument for its feasibility, by Samuelsen.¹² The essential ingredients of this picture are the observation that an applied magnetic field renders the junction dynamical equation asymmetric through the boundary conditions,¹³ thus rendering wave propagation along the junction asymmetric, and the observation that the average junction voltage in a fluxon propagation mode depends only upon the time-averaged number of fluxons present, so that, for example, the first FS is consistent with a situation in which a single fluxon is present for half the time. Later, a numerical simulation result which supported Samuelsen's hypothesis was reported by Dueholm *et al.*¹⁴

The purpose of this paper is to contribute to a clarification of the situation through a numerical simulation of a long Josephson junction in a magnetic field. The results that emerge give further support to the Samuelsen mechanism. Specific predictions of the frequencies and power levels of the microwave radiation emitted by a junction current-biased on a FS, as compared with the same quantities with the junction biased on a ZFS, are consistent with experimental measurements. Moreover, the results suggest further experimental measurements to check the proposed mechanism.

JUNCTION MODEL AND COMPUTATION TECHNIQUES

The junction model and computational procedures employed in this study are essentially those used in a previous study of ZFS.¹ An electrical representation of the model is shown in Fig. 1. The spatial dependence of the problem is taken into account by considering a 50-section lumped-circuit approximation to the junction. A junction length of $5\lambda_j$ is assumed throughout this study. Dissipation is assumed to be due only to the linear resistor R of Fig. 1. Accordingly, we assume simply that the powers radiated from the left and right ends of the junction at a given frequency are equal to the sum of the squares of the Fourier components $V_{\cos}^2 + V_{\sin}^2$ at that frequency of the end-point voltages V_L and V_R , respectively.

An overlap-geometry junction is assumed, implying that the bias current, I_B per section, may be considered to be uniformly distributed along the junction.¹⁵ The effect of an externally applied dc magnetic field B_{ex} in the plane of the junction and perpendicular to its long dimension is modeled by applying the dc current I_F as shown in Fig. 1. The relation between the two quantities is $B_{ex} = \mu_0 I_F / w$, where μ_0 is the permeability of free space and w is the width of the junction in the field direction.

The Josephson element J in Fig. 1 is characterized by the adiabatic Josephson equations

$$I = I_0 \sin \phi, \quad (1a)$$

$$\frac{d\phi}{dt} = \frac{2\pi}{\Phi_0} v. \quad (1b)$$

Combining Eqs. (1a) and (1b) with the circuit equations of Fig. 1 results in, for section 1,

$$\frac{\tau_c}{\tau_\Delta} \frac{dV_1}{d\tau} = \gamma + M + \lambda_j^2 (\phi_2 - \phi_1) - \sin \phi_1 - V_1, \quad (2a)$$

for section j ($1 < j < 50$),

$$\frac{\tau_c}{\tau_\Delta} \frac{dV_j}{d\tau} = \gamma + \lambda_j^2 (\phi_{j-1} - 2\phi_j + \phi_{j+1}) - \sin \phi_j - V_j, \quad (2b)$$

for section 50,

$$\frac{\tau_c}{\tau_\Delta} \frac{dV_{50}}{d\tau} = \gamma - M + \lambda_j^2 (\phi_{49} - \phi_{50}) - \sin \phi_{50} - V_{50}, \quad (2c)$$

and for all sections ($1 \leq j \leq 50$),

$$\frac{d\phi_j}{d\tau} = \frac{\pi}{2} V_j. \quad (2d)$$

Here V is voltage v normalized to $I_0 R$, τ is time normalized to $\tau_\Delta \equiv \Phi_0 / 4I_0 R$ (the inverse of the gap-sum frequency), $\tau_c \equiv RC$, $\gamma \equiv I_B / I_0$, $M \equiv I_F / I_0$, and $\lambda_j^2 \equiv \Phi_0 / 2\pi L I_0$. The value of the parameter τ_c / τ_Δ , which is a measure of the dissipation, is assumed to be 10 throughout this study; the value of the parameter M , which is a measure of the applied magnetic field, is fixed at 8.

Equations (2a)–(2d) correspond to a discretized version of the perturbed sine-Gordon equation, with boundary conditions given by $\phi_x(0, t) = \phi_x(l, t) \propto B_{ex}$, as employed by many other authors (see, e.g., Ref. 13). The time normalization employed in Eqs. (2a)–(2d) is the same as in Ref. 1, but it differs from that used by other authors, who measure time in units of the inverse plasma frequency $1/\omega_j \equiv (C\Phi_0/2\pi I_0)^{1/2}$. It is trivial to show that the relation between the two time scales is given by $\omega_j \tau_\Delta = (2\tau_c/\pi\tau_\Delta)^{-1/2}$. It is likewise trivial to show that the dissipative parameter $\tau_c/\tau_\Delta = 2\beta_c/\pi$, where β_c is the usual McCumber parameter.

Equations (2a)–(2d) were integrated by means of a fourth-order Runge-Kutta routine using a fixed time increment of $0.01\tau_\Delta$. The problem was integrated as an initial-value problem, and two types of initial conditions were employed:

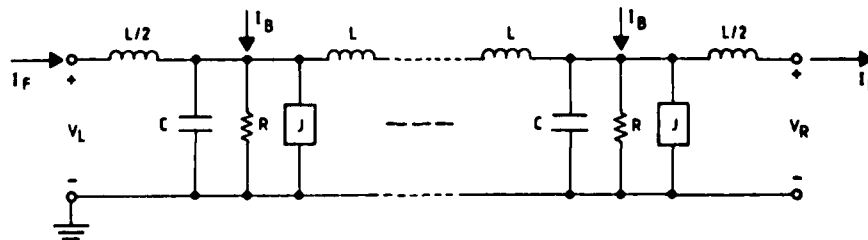


FIG. 1. Lumped circuit junction model.

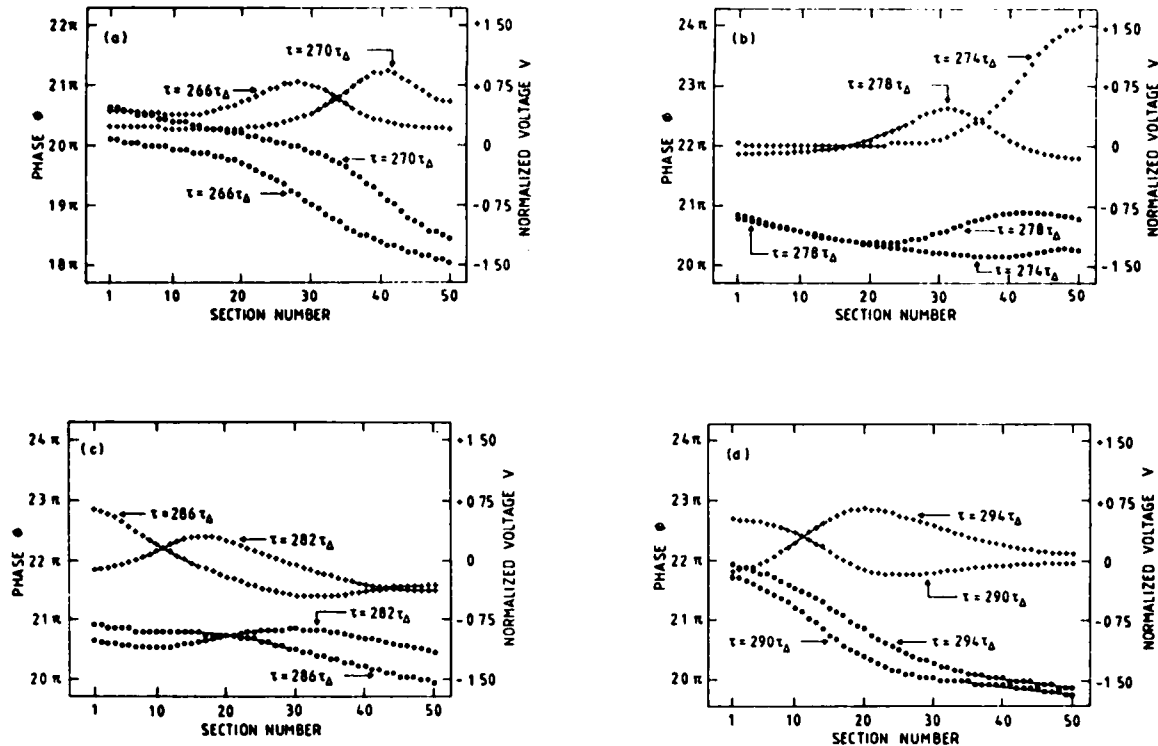


FIG. 2. Time evolution of FS-1 fluxon propagation for $\gamma=0.53$ and $M=8$. Circles: phase ϕ ; crosses: normalized voltage V . (a) $\tau=266\tau_{\Delta}$ and $270\tau_{\Delta}$; (b) $\tau=274\tau_{\Delta}$ and $278\tau_{\Delta}$; (c) $\tau=282\tau_{\Delta}$ and $286\tau_{\Delta}$; (d) $\tau=290\tau_{\Delta}$ and $294\tau_{\Delta}$. Apparent discontinuities are due to printer discretization.

(1) When searching for a first point on a given FS, the simple phase and voltage distributions shown in Fig. 2(a) of Ref. 1 were used. These distributions represent only a rough approximation to a single propagating fluxon, and their use constitutes a weakness in the calculations, as will be discussed below. (2) When searching for the upper (lower) extremity (in bias current) of a given FS, γ was increased (decreased) by a small increment and the initial phase and voltage distributions were taken as the final distributions corresponding to the previous bias value. The integration was continued until the oscillation settled into a steady state, defined operationally as in Ref. 1. Normally, this required integrating to about $300\tau_{\Delta}$ (about 9–10 complete oscillation periods).

After stopping the integration, the final two oscillation periods of the voltages at the two ends of the junction, V_L and V_R , were recorded on a grid of approximately 500 equally spaced points. The average values of these voltages, $\langle V_L \rangle$ and $\langle V_R \rangle$, were determined using the fact that the average voltage over a period is proportional to the phase difference

over that period, through the Josephson frequency relation, Eq. (2d). Physically, $\langle V \rangle$ must be constant along the entire junction; in practice, $\langle V_L \rangle$ and $\langle V_R \rangle$ were always equal to within better than 0.5%.

The Fourier sine and cosine coefficients of V_L and V_R were then obtained by trapezoidal rule integration of the basic definitions of these coefficients over the grid. Since the integration was performed over two oscillation periods, the first even-order harmonic was, in fact, the fundamental, and the absence of odd-order harmonics served as a further check that the oscillation had indeed reached a steady state.

FLUXON OSCILLATIONS AND FISKE STEPS

Figures 2 and 3 show a series of snapshots of the phase and voltage distributions along the junction over a single period of oscillation for two different modes of propagation. In Fig. 2(a), a fluxon is located near the center of the junction at $\tau=266\tau_{\Delta}$ and is propagating toward the right (this is an anti-fluxon by the definition used in Ref. 1, but the dis-

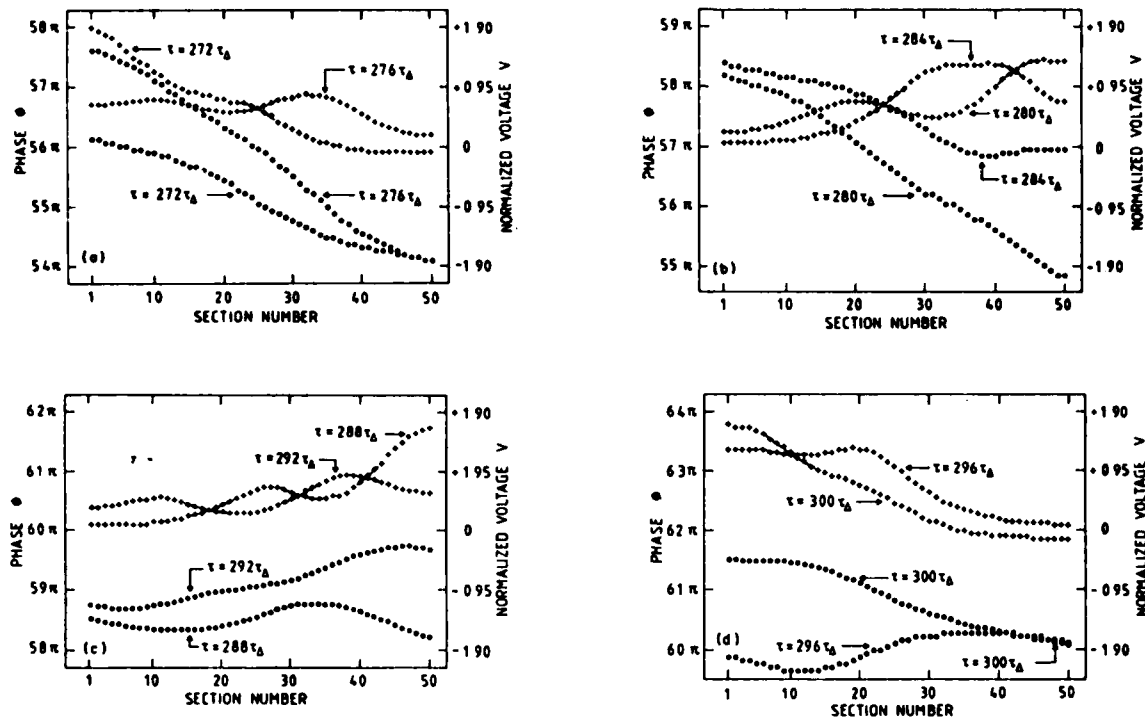


FIG. 3. Time evolution of FS-3 fluxon propagation for $\gamma=0.60$ and $M=8$. Circles: phase ϕ ; crosses: normalized voltage V . (a) $\tau=272\tau_{\Delta}$ and $276\tau_{\Delta}$; (b) $\tau=280\tau_{\Delta}$ and $284\tau_{\Delta}$; (c) $\tau=288\tau_{\Delta}$ and $292\tau_{\Delta}$; (d) $\tau=296\tau_{\Delta}$ and $300\tau_{\Delta}$. Apparent discontinuities are due to printer discretization.

inction is arbitrary). Note that there is a net phase difference of 2π along the junction and that the voltage is a well-defined pulse which is everywhere positive. At $\tau=270\tau_{\Delta}$, the fluxon is approaching a reflection at the right end of the junction. In Fig. 2(b), this reflection has just taken place at $\tau=274\tau_{\Delta}$, after which a clearly defined voltage pulse begins propagating to the left. Note, however, that the voltage waveform now goes both positive and negative, and that the net end-to-end phase difference is essentially zero. These facts suggest that the entity in question is a localized plasmon, or perhaps a plasmon-breather oscillation.¹⁶ In Fig. 2(c) this entity continues propagating to the left, and at $\tau=286\tau_{\Delta}$ it is approaching a reflection at the left end. In Fig. 2(d) this reflection has just occurred at $\tau=290\tau_{\Delta}$, whereupon propagation resumes toward the right. During the reflection, however, the net end-to-end phase difference has increased again toward 2π , so that at $\tau=294\tau_{\Delta}$ the oscillation has completed almost one full cycle. As is evident from Fig. 2, the phase at any point along the junction advances by a total of 2π during one oscillation period, as compared with the value of 4π for the oscillation associ-

ated with the first ZFS (cf. Fig. 2 of Ref. 1).

In Fig. 3 the situation is somewhat less "binary" inasmuch as the various propagating entities overlap one another, but the overall picture is still sufficiently clear. In Fig. 3(a), at $\tau=272\tau_{\Delta}$ there is a net phase difference of 2π along the junction and a voltage peak near section 21, corresponding to a fluxon moving to the right, but a second fluxon is rapidly entering from the left end. At $\tau=276\tau_{\Delta}$ two voltage pulses are clearly visible, and the net end-to-end phase difference is about 3.5π , corresponding to something less than two fluxons in the junction. In Fig. 3(b) this packet has moved to the right at $\tau=280\tau_{\Delta}$, with the first pulse approaching a reflection at the right end of the junction and the second one near section 21. During this portion of the oscillation the situation suggests, approximately, the propagation of two fluxons in a "bunched" configuration.^{17,18} At $\tau=284\tau_{\Delta}$ the leading voltage pulse has just emerged from the reflection and is located near section 40, moving to the left; whereas the trailing pulse is located near section 33 and moving to the right. In Fig. 3(c) the two voltage pulses have exchanged positions at $\tau=288\tau_{\Delta}$, with the leading

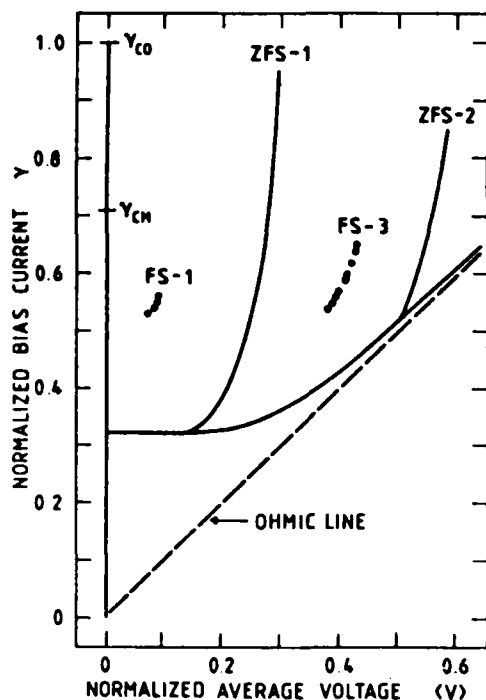


FIG. 4. Normalized current-voltage characteristic of the junction. Solid curve: magnetic field equal to zero, showing first two zero-field steps; circles: first and third Fiske steps for $M=8$. γ_{CM} is the field-reduced critical current value.

pulse now located near section 27, moving to the left, and the trailing pulse just undergoing a reflection from the right end. Note that the net phase difference along the junction is at this point essentially zero. At $\tau=292\tau_{\Delta}$ the two voltage pulses continue propagating to the left, and the net end-to-end phase difference has become approximately π . Interpretation of this situation is not completely unambiguous, but the propagation of a fluxon-plasmon, fluxon-breather, or fluxon-plasmon-breather combination is suggested. In Fig. 3(d) the

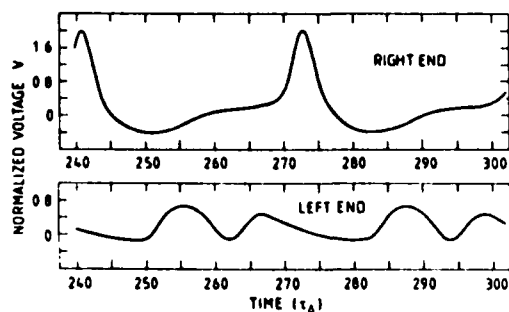


FIG. 5. End-point voltage waveforms of FS-1 fluxon oscillation for $\gamma=0.53$ and $M=8$.

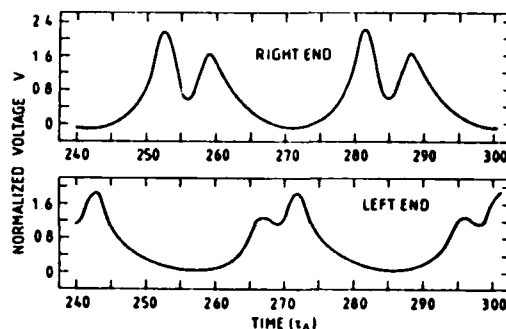


FIG. 6. End-point voltage waveforms of FS-3 fluxon oscillation for $\gamma=0.60$ and $M=8$.

leading voltage pulse is just undergoing a reflection from the left end of the junction at $\tau=296\tau_{\Delta}$, and the trailing pulse is located near section 19 and still moving to the left. At $\tau=300\tau_{\Delta}$ the leading pulse, barely distinguishable, is located near section 17, moving again toward the right, whereas the trailing pulse is approaching a reflection at the left end. The net end-to-end phase difference is now approximately 1.5π , and the oscillation has completed almost one full cycle. Figure 3 shows clearly that during one full period of this oscillation the phase at any point along the junction advances by a total of 6π .

Figures 2 and 3 show each of the two modes of propagation for a single value of the bias current. Each of these two modes, however, exists over a certain range of γ . This fact is displayed in Fig. 4, which shows the two loci of points, indicated as circles, labeled, respectively, as FS-1 and FS-3 in the $\gamma-\langle V \rangle$ plane. The solid curve, for reference, is the current-voltage characteristic of the junction in the absence of magnetic field, taken from Ref. 1. The positions of the two groups of circles relative to the first two zero-field steps, ZFS-1 and ZFS-2, confirm that FS-1 and FS-3 are, respectively, the first and third Fiske steps. The point γ_{CM} at $\langle V \rangle=0$, incidentally, is the value to which the critical current has been reduced by the magnetic field $M=8$.

At this point we note that there should also exist a second FS corresponding approximately in voltage position to ZFS-1, but we have not been able to find this FS numerically. We believe that the reason for this is that the initial condition employed is not really appropriate to finding FS-2. We have observed in calculating FS-1 and FS-3 that the outcome of the simulation depends, at least sometimes, quite strongly on the initial condition employed: If the initial condition is "too far" (by some measure) from the final propagating configuration, the junction tends to switch to some other mode of propagation.

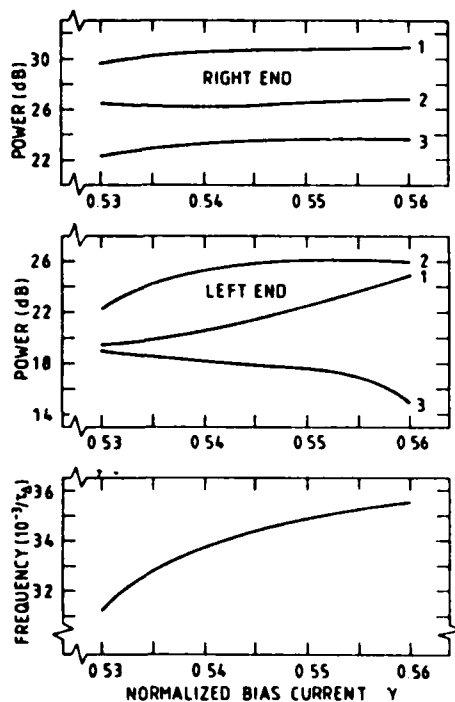


FIG. 7. Power spectra (first three harmonics) of the radiation emitted from the junction ends, normalized to $V_L, V_R = 0.04/\pi$. The frequency indicated is that of the fundamental component. The junction is biased on the first Fiske step.

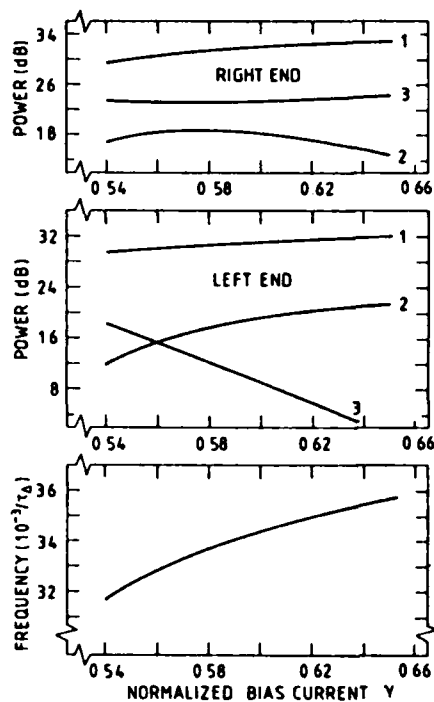


FIG. 8. Power spectra (first three harmonics) of the radiation emitted from the junction ends, normalized to $V_L, V_R = 0.04/\pi$. The frequency indicated is that of the fundamental component. The junction is biased on the third Fiske step.

POWER SPECTRA

Figures 2 and 3 clearly show that the two modes of propagation associated with FS-1 and FS-3 are asymmetric. This fact is underlined in Figs. 5 and 6, which show the temporal evolution of the two end-point voltages V_L and V_R in the two cases corresponding to Figs. 2 and 3, respectively.

Since we assume that the power radiated from an end of the junction is proportional to the square of the voltage at that end, it is clear that Figs. 5 and 6 imply that the spectra of the radiation emitted from the two ends are quite different. That this is indeed the case is indicated in Figs. 7 and 8, which show the power spectra, calculated as described above, for the first three Fourier components of the voltages V_L and V_R , corresponding, respectively, to FS-1 and FS-3 as a function of the bias current. The frequency shown in the lower part of the figures is that of the fundamental (labeled 1) Fourier component in each case. The power levels have been normalized to an arbitrary value of $V_L, V_R = 0.04/\pi$.

The main conclusions to be drawn from Figs. 7

and 8 are the following: (1) The fundamental frequencies associated with FS-1 and FS-3 are the same; moreover, they are the same as that associated with ZFS-1 [cf. Fig. 5(a) of Ref. 1]. This fact has already been confirmed by experimental observations.¹⁴ (2) The power levels of the radiation emitted by a junction biased on a FS are comparable, at least in the field-aided direction, with those obtained with the junction biased on a ZFS (cf. Fig. 5 of Ref. 1). This fact is also consistent with experimental observations.¹⁴ (3) The asymmetries in the power spectra of the radiation emitted from the two ends of the junction may well be large enough to be measurable. One way of doing this would be to couple to a single end of the junction and measure the radiation with both polarities of the magnetic field.

COMMENTS

The present work is intended as a contribution to the understanding of the dynamics of long Josephson tunnel junctions. We believe that fluxon propa-

gation is the basic physical mechanism underlying all of the various phenomena observed in connection with such long junctions, and that cavity-mode interaction analyses are essentially mathematical approximations that, as they become more refined, tend toward the same picture, being particularly suitable in the limit of short junctions. We propose that a detailed comparison of the results of experimental measurements on real junctions with those from careful numerical simulations, similar to those recently reported by Lomdahl *et al.*³ in connection with ZFS, should be an important objective for future studies.

ACKNOWLEDGMENTS

We are grateful to J. Mygind, M. R. Samuelsen, and A. C. Scott for helpful and stimulating discussions. One of us (A.F.) acknowledges financial support from the Deutscher Akademischer Austauschdienst. Another of us (R.D.P.) was supported in part by the Consiglio Nazionale delle Ricerche through the Gruppo Nazionale di Struttura della Materia and the Progetto Finalizzato "Superconduttività," and in part by the European Research Office of the United States Army through Contract No. DAJA37-82-C-0057.

*Permanent address: Istituto di Fisica, Università degli Studi di Salerno, I-84100 Salerno, Italy.

- ¹S. N. Ern  and R. D. Parmentier, *J. Appl. Phys.* **51**, 5025 (1980).
- ²B. Dueholm, O. A. Levring, J. Mygind, N. F. Pedersen, O. H. Soerensen, and M. Cirillo, *Phys. Rev. Lett.* **46**, 1299 (1981).
- ³P. S. Lomdahl, O. H. Soerensen, and P. L. Christiansen, *Phys. Rev. B* **25**, 5737 (1982).
- ⁴T. A. Fulton and R. C. Dynes, *Solid State Commun.* **12**, 57 (1973).
- ⁵I. O. Kulik, *Zh. Tekh. Fiz.* **37**, 157 (1967) [*Sov. Phys.—Tech. Phys.* **12**, 111 (1967)].
- ⁶G. Patern  and J. Nordman, *J. Appl. Phys.* **49**, 2456 (1978).
- ⁷K. Takanaka, *Solid State Commun.* **29**, 443 (1979).
- ⁸Y.-S. Gou and C.-S. Chung, *J. Low Temp. Phys.* **37**, 367 (1979).
- ⁹K. Enpuku, K. Yoshida, and F. Irie, *J. Appl. Phys.* **52**, 344 (1981).
- ¹⁰J.-J. Chang, J. T. Chen, and M. R. Scheuermann, *Phys. Rev. B* **25**, 151 (1982).
- ¹¹T. A. Fulton and L. N. Dunkleberger, *Rev. Phys. Appl.* **9**, 299 (1974).
- ¹²M. R. Samuelsen (private communication).
- ¹³O. H. Olsen and M. R. Samuelsen, *J. Appl. Phys.* **52**, 6247 (1981).
- ¹⁴B. Dueholm, E. Joergensen, O. A. Levring, J. Mygind, N. F. Pedersen, M. R. Samuelsen, O. H. Olsen, and M. Cirillo, *Physica* **108B**, 1303 (1981).
- ¹⁵A. Barone, W. J. Johnson, and R. Vaglio, *J. Appl. Phys.* **46**, 3628 (1975).
- ¹⁶R. D. Parmentier, in *Solitons in Action*, edited by K. Lonngren and A. Scott (Academic, New York, 1978), pp. 173–199.
- ¹⁷S. N. Ern  and R. D. Parmentier, *J. Appl. Phys.* **52**, 1091 (1981).
- ¹⁸P. L. Christiansen, P. S. Lomdahl, A. C. Scott, O. H. Soerensen, and J. C. Eilbeck, *Appl. Phys. Lett.* **39**, 108 (1981).

Intermittent Switching between Soliton Dynamic States in a Perturbed Sine-Gordon Model

M. P. Soerensen, N. Arley, P. L. Christiansen, R. D. Parmentier,^(a) and O. Skovgaard
Laboratory of Applied Mathematical Physics, The Technical University of Denmark, DK-2800 Lyngby, Denmark
 (Received 6 June 1983)

Chaotic intermittency between soliton dynamic states has been found in a perturbed sine-Gordon system in the absence of an external ac driving term. The system is a model of a long Josephson oscillator with constant loss and bias current in an external magnetic field. The results predict the existence of a current step between the first two Fiske steps in the current-voltage characteristic. A simple probability model demonstrates an asymmetry in the statistical nature of the switching in the two directions.

PACS numbers: 74.50.+r, 05.40.+j, 84.30.Ng, 85.25.+k

Chaos phenomena have been found for the rf- and dc-current driven small Josephson junction described by the resistively shunted junction (RSJ) model.¹ Recently Ben-Jacob *et al.* and Yeh and Kao reported on intermittent chaos in the numerical solution of this model.² For a long Josephson junction, the perturbed sine-Gordon equation (SGE) with spatially uniform or nonuniform oscillating driving forces and linear damping also gives rise to chaos in time and space-time.³ Detailed numerical investigations have revealed subharmonic generation caused by soliton motion in a long Josephson junction in a constant external magnetic field modeled by the perturbed SGE *without* an external ac driving term in the current bias.⁴ In the present Letter we demonstrate a new chaotic intermittency phenomenon between two dynamic states of this model. The two states correspond physically to the first two Fiske steps (FS1 and FS2, respectively) in the current-voltage characteristic of the junction.

The mathematical model studied is⁵

$$\varphi_{xx} - \varphi_{tt} - \sin\varphi = \alpha\varphi_t - \gamma, \quad (1a)$$

$$\varphi_x(0, t) = \varphi_x(L, t) = \eta. \quad (1b)$$

Here φ is the usual Josephson phase variable, x is distance normalized to the Josephson penetration depth λ_J , and t is time normalized to the inverse of the Josephson plasma frequency ω_0 . The γ term represents a uniformly distributed constant bias current normalized to the maximum zero-voltage (Josephson) current. The term in α represents quasiparticle loss. The constant η is a normalized measure of the external magnetic field which determines the boundary conditions (1b) at the ends of the junction of normalized length L . In this study $L = 5$, $\alpha = 0.252$, $\eta = 1.25$, and γ is varied in the range $\gamma = 0.45 - 0.55$. Equations (1) were integrated from appropriate initial conditions [similar to Eqs. (2) of Ref. 4 or con-

tinuations from runs done at nearby points in parameter space] for long periods of time (typically $t \sim 10000$) by means of the implicit finite-difference method described in detail in Ref. 5, with space and time intervals set equal to 0.05 and 0.025, respectively. Numerical accuracy and stability were verified by halving the space and time intervals.

In a narrow range of relatively low γ values ($\gamma = 0.450 - 0.454$) the solution develops stably into the FS1 solution illustrated in Fig. 1(a). In physical terms FS1 corresponds to a situation in which a soliton propagates in the field-aided direction, and is reflected at $x = 0$ as a localized plasma wave because of the energy loss at this boundary. This plasma wave then moves in the opposite direction and is reflected as a soliton at $x = L$ as a result of the energy injection here by the magnetic field. [An unambiguous interpretation of Fig. 1(a) in the schematic terms shown in Fig. 1(c) may be established by examining together $\varphi(x, t)$, $\varphi_x(x, t)$, and $\varphi_t(x, t)$.] The soliton then resumes propagation as before the reflections.^{4,6,7} On the average this cycle lasts the time $\bar{t}_{FS1} \approx 12$ (at $\gamma = 0.454$). For $\gamma < 0.450$ the junction switches into a static zero-voltage state where $\varphi_t = 0$.

For relatively high γ values ($\gamma = 0.500 - 0.540$) the solution develops stably into the FS2 solution corresponding to a situation in which a soliton and a localized plasma wave travel in opposite directions at the same time [shown numerically in Fig. 1(b) and schematically in Fig. 1(c)]. The average length of this cycle was estimated to be $\bar{t}_{FS2} \approx 6$ (at $\gamma = 0.500$). For $\gamma > 0.540$ the junction switches to FS3.

For intermediate γ values ($\gamma = 0.456 - 0.490$) the junction exhibits chaotic intermittency between FS1 and FS2. The intermittency is shown in Fig. 2 for $\gamma = 0.480$, where it is evidenced by changes in the average slope of φ versus t (on the FS1 portions $\langle \varphi_t \rangle \approx 0.6$ and on the FS2 por-

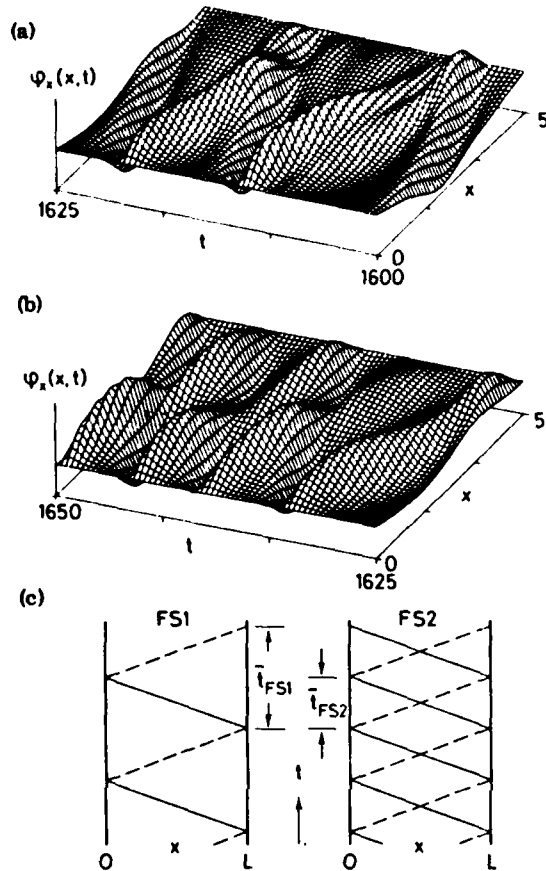


FIG. 1. $\varphi_x(x,t)$ on (a) FS1 and (b) FS2 portions of solution in intermittency region ($\gamma = 0.480$). (c) Schematic representations of (a) and (b) showing soliton (solid lines) and plasma-wave (dashed lines) trajectories. A switch from FS1 to FS2 is seen at $t \approx 1625$.

tions ($\langle \varphi_t \rangle \approx 1.0$). The switch from FS2 to FS1 occurs when the plasma oscillation fails to generate a soliton at $x = L$. Conversely, a switch from FS1 to FS2 may occur when an extra soliton is generated at $x = L$ during the FS1 cycle. The power spectrum (inset in Fig. 2) of $\varphi_t(0,t)$, normalized to $\varphi_t^2 = 4 \times 10^{-7}$, was obtained by a fast Fourier transform over the time interval 1600–3238 by use of a Hamming window.⁸ Since loading effects are not included in the model, the power levels in this spectrum represent ideal, available values. Translation into physically measurable quantities requires a knowledge of the junction-to-microwave circuit coupling (to set the physical power scale) and the junction plasma frequency (to set the physical frequency scale). The spectrum shows numerous frequency components among which the two dominant lines at $t^{-1} = 0.10$ and 0.17 may be ascribed to the soliton motion

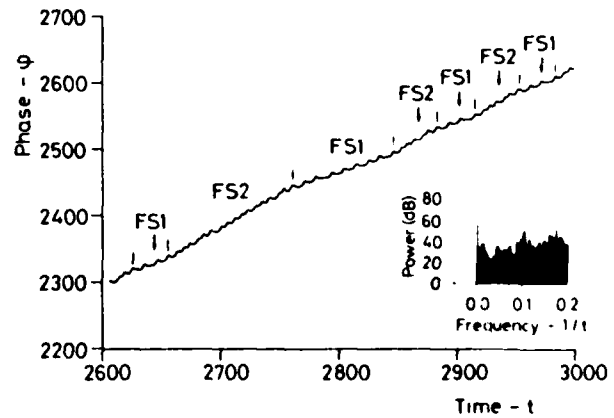


FIG. 2. Phase vs time at the left end ($x = 0$) showing intermittency between FS1 and FS2 at $\gamma = 0.480$. Inset: Power spectrum of $\varphi_t(0,t)$, normalized to $\varphi_t^2 = 4 \times 10^{-7}$, for $t = 1600-3238$, with frequency measured in units of the Josephson plasma frequency.

on FS1 and FS2, respectively. The average times the junction remains on FS1 and FS2 were found to be $\bar{T}_{FS1} \approx 46$ and $\bar{T}_{FS2} \approx 52$ (at $\gamma = 0.480$). We have found that \bar{T}_{FS1} and \bar{T}_{FS2} remain stationary in time at these values. The corresponding lines are barely visible in the low end of the power spectrum.

For a particularly long time interval shown in Fig. 3 ($t = 1902-2079$) the junction remained on FS2. Around $t = 1960$ the development of aperiodicity is observed. The insets (a) and (b) show the power spectrum for the time intervals 1902–1951 and 1984–2079, respectively, again ob-

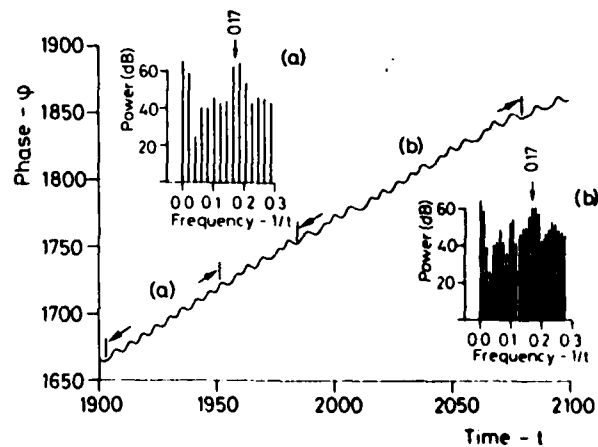


FIG. 3. Phase vs time at the left end ($x = 0$) for a particularly long operation on FS2 at $\gamma = 0.480$. Insets: Power spectra of $\varphi_t(0,t)$, normalized to $\varphi_t^2 = 4 \times 10^{-7}$, for (a) $t = 1902-1951$ and (b) $t = 1984-2079$. The fundamental frequency is $f_0 = 0.17$.

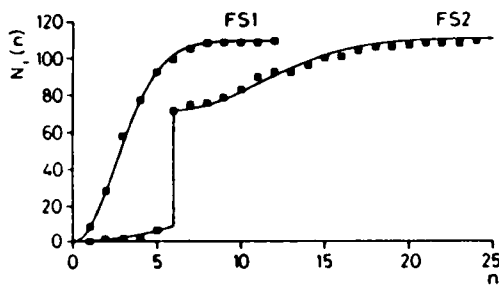


FIG. 4. Abscissa: Length of time interval on FS1 and FS2 measured in terms of number of cycles, n , of lengths \bar{t}_{FS1} and \bar{t}_{FS2} , respectively. Ordinate: Dots show number of intervals, $N_i(n)$, with $i=1,2$, shorter than or equal to n . Full curves result from theoretical estimates with $p_{12}(t) = (1.0 \times 10^{-3})t$, $p_{21}(t) = (1.2 \times 10^{-4})t$ for $n < 6$, $p_{21}(t) = (0.95 \times 10^{-5})t$ for $n > 6$. Bias $\gamma = 0.480$.

tained by use of a Hamming window. In inset (a) we observe the dominant frequency at $t^{-1} \approx 0.17$ and a relatively low content of subharmonics. In inset (b) subharmonics have developed at approximately $\frac{1}{3}$ and $\frac{2}{3}$ of this frequency. A similar building up of subharmonics is *not* seen while the junction operates on FS1.

Figure 4 (dots) shows the accumulated distributions, $N_1(n)$ and $N_2(n)$, of the lengths of the time intervals the junction operates on FS1 and FS2 for 217 switches between the two steps during a run of over 10000 time units. Here n is t/\bar{t}_{FS1} and t/\bar{t}_{FS2} , respectively. To analyze this situation, let the probability that the junction switches from FS1 to FS2 in the time interval $[t, t+dt]$, where t is the time after the last switch, be $p_{12}(t)dt$. Furthermore, if all the switches are independent, then the switching is a Poisson process. Consequently, the probability $P_1(t)$ that the oscillator switches from FS1 to FS2 within the time t becomes $P_1(t) = 1 - \exp[-\int_0^t p_{12}(\tau)d\tau]$. Assuming $p_{12}(t) = pt$, with $p = 1.0 \times 10^{-3}$, we get for FS1 the fit $N_1 = P_1(n\bar{t}_{FS1})N_{1max}$, where N_{1max} is the total number of intervals on FS1, shown in Fig. 4 (full curve). The agreement between the numerical data and this simple, but arbitrary, probability model is quite good.

For FS2 a jump of 63 in $N_2(n)$ at $n=6$ is observed in our 10000-time-unit run. Only by use of a transition probability, $p_{21}(t)$, containing 0.96 times a unit impulse at $n=6$, besides a linear term, do we obtain the fit shown in Fig. 4. The difference between the two results clearly demonstrates an asymmetry in the statistical nature of the switching in the two directions. The reason for this fact is not known. A possible cause

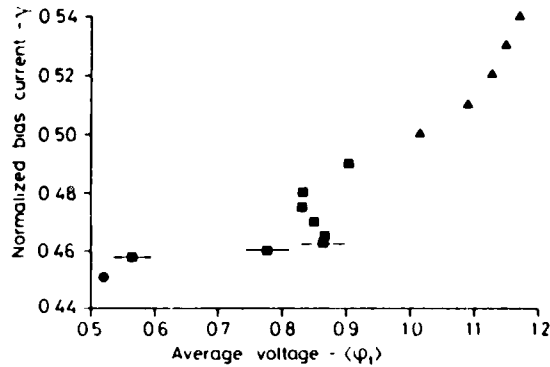


FIG. 5. Detail of current-voltage characteristic for $L=5$, $\alpha=0.252$, $\eta=1.25$. FS1 (circles), FS1 $_{1/2}$ (squares), and FS2 (triangles). Error limits for $\langle \varphi_t \rangle$ are indicated by horizontal bars when larger than 0.01.

may be an interference between the subharmonics $\frac{1}{3}$ and $\frac{2}{3}$ which build up on FS2, as seen in Fig. 3, but the question certainly requires further study.

Finally, Fig. 5 shows the resulting current-voltage characteristic for the γ interval covering FS1, the intermittency region, and FS2. At the average voltage $\langle \varphi_t \rangle \approx 0.83$ a jump in the current (from $\gamma = 0.462$ to $\gamma = 0.480$) occurs. We propose the name "FS1 $_{1/2}$ " for this portion of the characteristic. We have checked that the values of $\langle \varphi_t \rangle$ are stationary in time. Thus it should be possible to detect FS1 $_{1/2}$ experimentally. Recent measurements by Cirillo, Costabile, and Parmentier⁹ have in fact perhaps revealed such structures.

We thank A. C. Scott and N. F. Pedersen for stimulating discussions. The financial support of the Danish Natural Science Research Council, the Thomas B. Thrige Fond, and the European Research Office of the U. S. Army through Contract No. DAJA 37-82-C-0057 is acknowledged.

⁽⁹⁾Permanent address: Istituto di Fisica, Università di Salerno, I-84100 Salerno, Italy.

¹B. A. Huberman, J. P. Crutchfield, and N. H. Packard, *Appl. Phys. Lett.* **37**, 750 (1980); N. F. Pedersen and A. Davidson, *Appl. Phys. Lett.* **39**, 830 (1981); M. Cirillo and N. F. Pedersen, *Phys. Lett.* **90A**, 150 (1982); R. L. Kautz, *IEEE Trans. Magn.* **19**, 465 (1983); A. H. MacDonald and M. Plischke, *Phys. Rev. B* **27**, 201 (1983).

²E. Ben-Jacob, I. Goldhirsch, Y. Imry, and S. Fishman, *Phys. Rev. Lett.* **49**, 1599 (1982); W. J. Yeh and

Y. H. Kao, *Appl. Phys. Lett.* **42**, 299 (1983).

³J. C. Eilbeck, P. S. Lomdahl, and A. C. Newell, *Phys. Lett.* **87A**, 1 (1981); D. Bennett, A. R. Bishop, and S. E. Trullinger, *Z. Phys.* **B74**, 265 (1982); A. R. Bishop, K. Fesser, P. S. Lomdahl, W. C. Kerr, M. B. Williams, and S. E. Trullinger, *Phys. Rev. Lett.* **50**, 1095 (1983); M. Imada, *J. Phys. Soc. Jpn.* **52**, 1946 (1983).

⁴M. P. Soerensen, P. L. Christiansen, R. D. Parmentier, and O. Skovgaard, *Appl. Phys. Lett.* **42**, 739 (1983).

⁵P. S. Lomdahl, O. H. Soerensen, and P. L. Christiansen, *Phys. Rev. B* **25**, 5737 (1982).

⁶B. Dueholm, E. Joergensen, O. A. Levring, J. Mygind, N. F. Pedersen, M. R. Samuelson, O. H. Olsen, and M. Cirillo, *Physica (Utrecht)* **108B**, 1303 (1981).

⁷S. N. Erne, A. Ferrigno, and R. D. Parmentier, *Phys. Rev. B* **27**, 5440 (1983).

⁸R. W. Hamming, *Digital Filters* (Prentice-Hall, Englewood Cliffs, N.J., 1983), 2nd ed.

⁹M. Cirillo, G. Costabile, and R. D. Parmentier, unpublished.

FLUXON DYNAMICS ON THE CIRCULAR JOSEPHSON OSCILLATOR [☆]

F. IF, M.P. SOERENSEN and P.L. CHRISTIANSEN

*Laboratory of Applied Mathematical Physics, The Technical University of Denmark,
DK-2800 Lyngby, Denmark*

Received 20 May 1983

Revised manuscript received 29 September 1983

A hamiltonian perturbation theory is developed for the perturbed sine-Gordon equation with periodic boundary conditions modelling the Josephson ring oscillator. Stationary fluxon velocities are determined as function of length, loss and bias parameters.

The circular Josephson oscillator was originally proposed by Scott and McLaughlin [1] who pointed out that this oscillation structure may be of technical importance at electromagnetic wavelengths of 100 μm or less. This oscillator structure has in fact been included in the current programmes of several experimental groups [2]. The mathematical model for the circular Josephson oscillator with losses and bias current is a perturbed sine-Gordon equation [3] with periodic boundary conditions and fixed winding number. These boundary conditions close the circular oscillator in a perfect matching and thus permit undisturbed fluxon motion on the oscillator. Furthermore the boundary conditions are ideal for spectral method numerical studies of the radiation from the oscillator. However, perturbation methods for fluxon dynamics so far have only been used for infinitely long Josephson junctions [1]. In the present note ^{††} the perturbation method is extended to the finite case with periodic boundary conditions.

The normalized perturbed sine-Gordon equation [3] with periodic boundary conditions can be written

$$\phi_{xx} - \phi_{tt} - \sin \phi = \alpha \phi_t - \beta \phi_{xxt} + \gamma,$$

[☆] Supported by the Danish Council for Scientific and Industrial Research and by United States Army through its European Research Office.

^{††} Based on a master's thesis by one of the authors (F.I.).

$$\phi_x(0, t) = \phi_x(l, t), \quad \phi_t(0, t) = \phi_t(l, t), \quad (1)$$

where the α term represents quasi-particle loss across the barrier and the β term the surface impedance of the superconductor. The γ term is the bias current. The circumference of the circular transmission line normalized to the Josephson length is denoted l in the periodic boundary conditions. According to hamiltonian perturbation theory [1] the hamiltonian for the unperturbed sine-Gordon equation,

$$H = \int_0^l (\frac{1}{2} \phi_x^2 + \frac{1}{2} \phi_t^2 + 1 - \cos \phi) dx,$$

satisfies the differential equation

$$\frac{dH}{dt} = - \int_0^l (\alpha \phi_t^2 + \beta \phi_{xt}^2 + \gamma \phi_t) dx \quad (2)$$

for small values of α , β , and γ .

The travelling wave solution to the unperturbed sine-Gordon equation is given by [4]

$$\phi = 2 \sin^{-1} [\pm \text{cn}(\xi, k)], \quad (3)$$

with $\xi = (x - ut)/k(1 - u^2)^{1/2}$. Here $\text{cn}(\xi, k)$ is a jacobian elliptic function [5] with modulus k . Plus and minus sign refer, respectively, to fluxons and antifluxons. The velocity of the wave is denoted u . If the modulus satisfies the condition

$$l/(1-u^2)^{1/2} = 2kK(k), \tag{4}$$

the periodic function ϕ gets the period l , and ϕ represents a single fluxon (or antifluxon). As in ref. [5] the normal complete elliptic integrals of first and second kind are denoted $K(k)$ and $E(k)$, respectively.

Using eq. (3) we get the new expression for the hamiltonian

$$H = 8(1-u^2)^{-1/2}E(k)/k - 4k^{-1}(1-k^2)(1-u^2)^{1/2}K(k). \tag{5}$$

Inserting eq. (5) with $u = u(t)$ on the lhs of eq. (2) and ϕ given by (3) on the rhs of eq. (2) we obtain

$$du/dt = \pm \frac{1}{4}\pi\gamma'(1-u^2)^{3/2} - \alpha'u(1-u^2) - \frac{1}{3}\beta'u, \tag{6}$$

with $\alpha' = 2\alpha k^2 E(k)/\Delta$, $\beta' = 2\beta[(2-k^2)E(k)$

$- 2(1-k^2)K(k)]/\Delta$, $\gamma' = 2\gamma k^3/\Delta$, and $\Delta = 2k^2E(k) + (1-k^2)l^2/4K(k)$. Here eq. (6) has the same form as the perturbation equation for the infinitely long Josephson transmission line. Thus for $l \rightarrow \infty$ it can be shown that $\alpha' \rightarrow \alpha$, $\beta' \rightarrow \beta$, and $\gamma' \rightarrow \gamma$. In the opposite limit, $l \rightarrow 0$, we find $\alpha' \rightarrow \frac{2}{3}\alpha$, $\beta' \rightarrow 0$, and $\gamma' \rightarrow 0$.

The stationary velocity $u = u_\infty$ is obtained from (6) by letting $du/dt = 0$. The periodicity condition (4) is approximately valid for the perturbed sine-Gordon equation in the stationary state. Using (4) with $u = u_\infty$ in (6) we obtain u_∞ as function of l . This function is shown in fig. 1a and b for different values of the parameters α and β . We note that a maximum velocity occurs for relatively small values of the ratio α/β . In the limit $\alpha = 0$ it can be shown that $u \rightarrow 1$ for $l \rightarrow 0$. For $\alpha \neq 0$, $u \rightarrow 0$ for $l \rightarrow 0$ due to the fact that effective bias, γ' , vanishes in this limit while the effective loss, α' , tends towards a finite value.

Fig. 2 shows the velocity as function of the bias for different values of the length. The curves intersect because the same velocity, u , occurs for two different values of l for certain values of α , β , and γ is seen in fig. 1. The similarity between the curves and the first zero field step [4] in the $I-V$ characteristic is due to the fact that the normalized voltage $V = 2\pi u_\infty/l$ for $l \gg 1$. The current $I \propto \gamma$.

In order to check the validity of the perturbation theory we have solved eq. (1) numerically with the static one-fluxon solution

$$\phi = 2 \sin^{-1} [\text{cn}((x-l/2)/k, k)] - \sin^{-1} \gamma$$

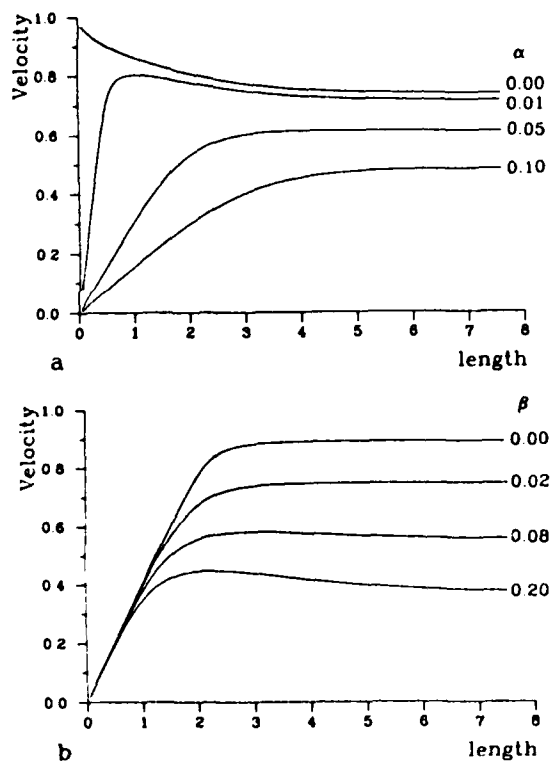


Fig. 1. Stationary one-fluxon velocity, u_∞ , versus length of Josephson oscillator, l , estimated by means of hamiltonian perturbation theory. (a) $\beta = 0.10$, $\gamma = 0.10$, $\alpha = 0.00, 0.01, 0.05$, and 0.10 , (b) $\alpha = 0.02$, $\gamma = 0.05$, $\beta = 0.00, 0.02, 0.08$, and 0.20 .

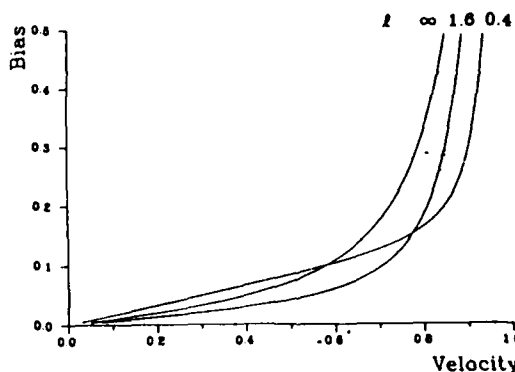


Fig. 2. The bias current, γ , versus the stationary one-fluxon velocity, u_∞ , estimated by means of hamiltonian perturbation theory. $\alpha = 0.01$, $\beta = 0.2$, $l = 0.4, 1.6$, and ∞ .

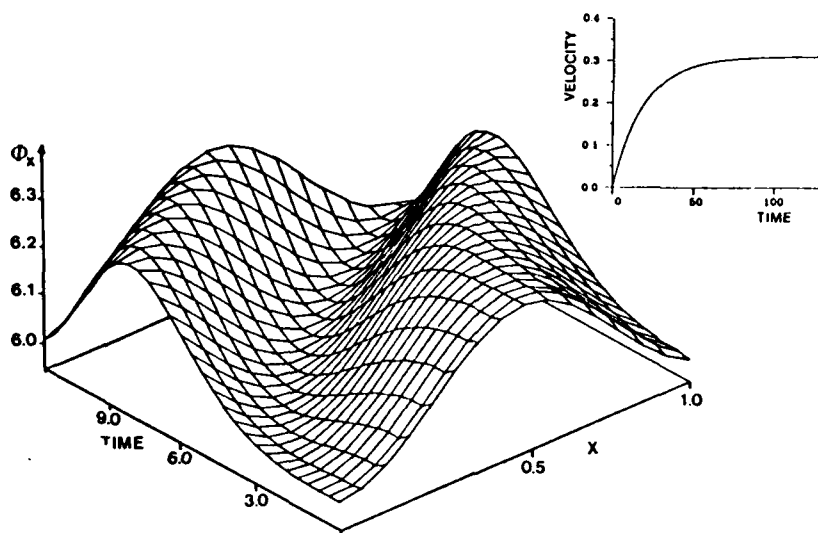


Fig. 3. Numerical solution of eq. (1), shown in terms of ϕ_x , with $\alpha = 0.05$, $\beta = 0.10$, $\gamma = 0.10$, and $l = 1.0$. Inset shows the fluxon velocity, u , versus time t computed by means of the numerical solution.

in the initial conditions. The method used is a spectral (Fourier transform) treatment of the space dependence together with a leap-frog scheme in time. The resulting acceleration of the fluxon is seen in fig. 3. The fluxon velocity shown in the inset converges towards the value $u_{\infty, \text{num}} = 0.3091$ in good agreement with the predicted value $u_{\infty, \text{pert}} = 0.3086$.

We conclude that hamiltonian perturbation theory can be used to predict the stationary one-fluxon velocity on the circular Josephson oscillator. The results will be useful for the interpretation of experimental measurements of the I - V characteristic for this device.

We are pleased to thank R.D. Parmentier, N.F. Pedersen, A.C. Scott and O. Skovgaard for helpful discussions.

References

- [1] D.W. McLaughlin and A.C. Scott, Phys. Rev. A18 (1978) 1652.
- [2] A. Davidson and N.F. Pedersen, private communication.
- [3] A.C. Scott, F.Y.F. Chu and S.A. Reible, J. Appl. Phys. 47 (1976) 3272.
- [4] R.D. Parmentier, in: Solitons in action, eds. K. Lonngren and A. Scott (Academic Press, New York, 1978) p. 173.
- [5] P.F. Byrd and M.D. Friedman, Handbook of elliptic integrals for engineers and physicists (Springer, Berlin, 1954).

Phonons and solitons in the "thermal" sine-Gordon system

Mario Salerno*

Laboratory of Applied Mathematical Physics, The Technical University of Denmark, DK-2800 Lyngby, Denmark

E. Joergensen and M. R. Samuelsen

Physics Laboratory I, The Technical University of Denmark, DK-2800 Lyngby, Denmark

(Received 23 September 1983)

Standard methods of stochastic processes are used to study the coupling of the sine-Gordon system with a heat reservoir. As a result we find thermal phonons with an average energy of $k_B T$ per mode. The translational mode (zero mode) is found to carry an average energy of $\frac{1}{2} k_B T$. This last value is just the energy in the Brownian motion of a thermal soliton. These results are in agreement with those obtained by the use of a statistical-mechanical description of a dilute soliton gas. Connection of the above results with Josephson junctions and the extension of the analysis to more general equations is also discussed.

I. INTRODUCTION

The sine-Gordon equation has recently been used to model several physical systems in contact with a heat reservoir at a given temperature.¹⁻⁹ The effect of the coupling of the sine-Gordon system to the heat reservoir provides a twofold mechanism:

- (i) a dissipation of energy in the system due to an energy flow from the system to the heat reservoir,
- (ii) a disordered input of energy into the system due to a flow back of energy from the reservoir.

A loss term in the sine-Gordon equation is then intrinsically connected to a thermal noise term, suggesting a modeling of the interaction between the system and the reservoir with a driving stochastic force (temperature dependent) in the pure sine-Gordon equation:^{1,3-5,7}

$$\phi_{xx} - \phi_n - \sin\phi = \alpha\phi_t + n(x, t). \quad (1.1)$$

The first term on the right-hand side (rhs) of Eq. (1.1) is the loss term representing the energy flow to the reservoir, while the second term is the noise associated with α , giving the *disordered* thermal-energy input to the system. The noise term is assumed to be "white" both in space and time with the autocorrelation function:

$$\langle n(x, t)n(x', t') \rangle = 16\alpha(k_B T/E_0)\delta(x-x')\delta(t-t'). \quad (1.2)$$

Here $\langle \dots \rangle$ means ensemble average, while the constant $16\alpha(k_B T/E_0)$ is determined by applying the fluctuation dissipation theorem for a soliton with small velocity^{1,4,7,10} (E_0 is the rest energy of a soliton and is used to fix the scale of energy in the system, k_B is the Boltzmann constant, and T is the temperature).

When $\alpha=0$, $n(x, t)=0$, Eq. (1.1) reduces to the pure sine-Gordon equation with the exact soliton solution

$$\phi = 4 \tan^{-1} \left[\exp \pm \left(\frac{x-vt}{(1-v^2)^{1/2}} \right) \right] \quad (1.3)$$

and Hamiltonian density

$$H = \frac{E_0}{8} \left[\frac{1}{2} (\phi_x^2 + \phi_t^2) + 1 - \cos\phi \right]. \quad (1.4)$$

Small oscillations around a ground state ϕ_0 of the system are obtained by linearizing the sine-Gordon equation with

$$\phi = \phi_0 + \psi, \quad (1.5)$$

this providing a linear equation for ψ :

$$\psi_{xx} - \psi_{tt} - \psi \cos\phi_0 = 0, \quad (1.6)$$

with an associated energy density given by

$$H_{ph} = \frac{E_0}{16} (\psi_x^2 + \psi_t^2 + \psi^2 \cos\phi_0). \quad (1.7)$$

When the ground state of the system is given by (1.3), a "zero mode" (translational mode) is found from Eq. (1.6). In addition to this mode, there exists a continuum set of states (phonon modes) which satisfy the linear dispersion relation:¹¹

$$\omega^2 = 1 + k^2. \quad (1.8)$$

For practical applications to Josephson junctions, it is of interest to include also in the rhs of Eq. (1.1) a constant bias term η , representing an *ordered* energy input into the system (work on the system). In this case (in the absence of solitons), phonons (also called "plasmons") are seen as small oscillations around the ground state $\phi_0 = -\sin^{-1}\eta$.¹²

In this paper we study the effect of the heat reservoir both on solitons and phonons by using standard methods of stochastic processes. This will be done in the following cases.

In Sec. II we study thermal phonons in the presence of a static "exact" sine-Gordon soliton. In Sec. III we include a η bias term in the rhs of (1.1) and study the thermally excited plasmons around $\phi_0 = -\sin^{-1}\eta$ (no solitons present in the system).

In both cases we find that as long as $k_B T \ll E_0$, the

phonon modes have an average energy of $k_B T$ per mode. In the case when a soliton is in the system, however, we find that the corresponding extra mode (zero mode), has an average energy of $\frac{1}{2} k_B T$. All these results are in agreement with a statistical-mechanical description of the sine-Gordon system. In Sec. IV we concentrate on the effect of both the bias term (η) and the heat reservoir [α and $n(x,t)$] on the soliton motion. As result of the "thermalization" the soliton will execute a Brownian motion with average energy of $\frac{1}{2} k_B T$ (the zero-mode energy). In Sec. V we relate the above results to a practical Josephson junction and, finally, in Sec. VI we give a short summary of the main results of the paper including a brief discussion of the possibility of extending the analysis to other equations of the nonlinear Klein-Gordon class.

II. THERMAL PHONONS IN THE PRESENCE OF A SOLITON

We consider as an "unthermalized" system the pure sine-Gordon equation

$$\phi_{xx} - \phi_n - \sin\phi = 0 \quad (2.1)$$

and assume that only a static soliton is present (dilute-gas limit). Phonon modes ψ_k are obtained as solutions of Eq. (1.6) with ϕ_0 given by (1.3) with $\nu = 0$. Assuming ψ_k as

$$\psi_k(x,t) = f_k(x) e^{i\omega_k t}, \quad (2.2)$$

we obtain from Eq. (1.6) that

$$(-\partial_{xx} + 1 - 2 \operatorname{sech}^2 x) f_k(x) = \omega_k^2 f_k(x). \quad (2.3)$$

As is well known, (2.3) admits a continuum set of eigenfunctions:

$$f_k(x) = \frac{1}{(2\pi)^{1/2}} e^{ikx} (1+k^2)^{-1/2} (k+i \tanh x) \quad (2.4)$$

together with a zero mode:

$$f_b(x) = \frac{1}{\sqrt{2}} \operatorname{sech} x \quad (2.5)$$

which restores the translational symmetry broken by the introduction of the soliton into the system (Goldstone mode).¹¹ Equations (2.4) and (2.5) together form a complete set of orthonormal eigenfunctions:

$$\int_{-\infty}^{+\infty} f_b^*(x) f_b(x) dx = 1, \quad \int_{-\infty}^{+\infty} f_b(x) f_k(x) dx = 0$$

$$\int_{-\infty}^{+\infty} f_k^*(x) f_{k'}(x) dx = \delta(k-k'), \quad (2.6)$$

$$f_b(x) f_b(x') + \int_{-\infty}^{+\infty} f_k^*(x) f_k(x') dk = \delta(x-x')$$

where * in the superscript means complex conjugate.

By coupling the sine-Gordon system with the heat reservoir, we change Eq. (2.1) into Eq. (1.1). Thermal phonons are then found to satisfy

$$\psi_{xx} - \psi_n - \psi \cos\phi_0 = \alpha \psi_t + n(x,t) \quad (2.7)$$

for which the general solution can be expanded in terms of the complete set (2.6) as

$$\psi_k(x,t) = \sum_{n=0}^{\infty} A_k(t) f_k(x) + A_b(t) f_b(x) \quad (2.8)$$

(here we assume the system to be in a box of length L , and then let $L \rightarrow \infty$). Substituting (2.8) in (2.7) and using Eq. (2.3), we obtain

$$\sum_{n=0}^{\infty} [A_{k,n} f_k(x) + \alpha A_{k,t} f_k(x) + A_k \omega_k^2 f_k(x)] + (A_{b,n} + \alpha A_{b,t}) f_b(x) = -n(x,t). \quad (2.9)$$

Equation (2.9) is easily studied once projected, respectively, along the $f_k(x)$'s and the $f_b(x)$ eigenfunctions, this giving [using (2.6)]

$$A_{k,n} + \alpha A_{k,t} + A_k \omega_k^2 = \epsilon_k(t) \quad (2.10)$$

and

$$A_{b,n} + \alpha A_{b,t} = \epsilon_b(t) \quad (2.11)$$

with

$$\epsilon_b(t) = - \int_{-\infty}^{+\infty} f_b(x) n(x,t) dx,$$

$$\epsilon_k(t) = - \int_{-\infty}^{+\infty} f_k^*(x) n(x,t) dx.$$

By using (1.2) and (2.6) we find, for the autocorrelation function $R_{\epsilon}(t-t')$ and for the power spectrum $S_{\epsilon}(\omega)$ of the normal processes $\epsilon_k(t)$ and $\epsilon_b(t)$, that

$$R_{\epsilon_k}(t-t') = R_{\epsilon_b}(t-t') = 16\alpha(k_B T/E_0) \delta(t-t'), \quad (2.12)$$

$$S_{\epsilon_k}(\omega) = S_{\epsilon_b}(\omega) = 16\alpha(k_B T/E_0). \quad (2.13)$$

Equations (2.10) and (2.11) are then integrated by the standard theory of stochastic processes,¹⁰ giving the following expressions for the power spectrum of $A_k(t)$ and $A_{k,t}(t)$:

$$S_{A_k}(\omega) = 16\alpha(k_B T/E_0) \frac{1}{(\omega^2 - \omega_k^2)^2 + \alpha^2 \omega^2}, \quad (2.14)$$

$$S_{A_{k,t}}(\omega) = \omega^2 S_{A_k}(\omega). \quad (2.15)$$

[$S_{A_b}(\omega)$ and $S_{A_{b,t}}(\omega)$ are obtained from (2.14) and (2.15) with the substitution $\omega_k = 0$.] If we assume ergodicity, the time averages of the processes $|A_k(t)|^2$ and $|A_{k,t}(t)|^2$ are evaluated as

$$\langle |A_k(t)|^2 \rangle = R_{A_k}(0) = \int_{-\infty}^{+\infty} \frac{d\omega}{2\pi} S_{A_k}(\omega) = 8(k_B T/\omega_k^2 E_0), \quad (2.16)$$

$$\langle |A_{k,t}(t)|^2 \rangle = R_{A_{k,t}}(0) = \int_{-\infty}^{+\infty} \frac{d\omega}{2\pi} S_{A_{k,t}}(\omega) = 8(k_B T/E_0), \quad (2.17)$$

where contour integration has been used in evaluating the integrals in (2.16) and (2.17). In the same way we obtain

for $\langle |A_{k,i}(t)|^2 \rangle$

$$\langle |A_{k,i}(t)|^2 \rangle = 8(k_B T / E_0). \quad (2.18)$$

From (1.7) and (2.8) we have that the average energies of the k th phonon mode $A_k(t)f_k(x)$ and of the translational mode $A_b(t)f_b(x)$ are given, respectively, by

$$\langle H_k \rangle = \frac{E_0}{16} [\langle |A_{k,i}(t)|^2 \rangle + \omega_k^2 \langle |A_k(t)|^2 \rangle] \quad (2.19)$$

and

$$\langle H_b \rangle = \frac{E_0}{16} \langle |A_{b,i}|^2 \rangle. \quad (2.20)$$

Using (2.16)–(2.18), we finally have

$$\langle H_k \rangle = k_B T \quad (2.21)$$

and

$$\langle H_b \rangle = \frac{1}{2} k_B T \quad (2.22)$$

in complete agreement with the classical statistical-mechanics analysis of a dilute soliton gas derived in Ref. 8.

III. THERMAL PHONONS IN THE ABSENCE OF SOLITONS WITH BIAS

In this section we consider the unthermalized system to be the pure sine-Gordon system of finite length L , with a constant driving force $\eta < 1$:

$$\phi_{xx} - \phi_{tt} - \sin\phi = \eta. \quad (3.1)$$

Phonon modes ψ_n are seen as small oscillations around the classical ground state

$$\phi_0 = -\sin^{-1}\eta, \quad (3.2)$$

satisfying the boundary conditions

$$\psi_{n,x}(0,t) = \psi_{n,x}(L,t) = 0 \quad (3.3)$$

(no solitons are present in the system). The thermalized system is obtained from Eq. (3.1) by adding to the rhs the term $\alpha\phi_t + n(x,t)$ with $n(x,t)$ given as in (1.2):

$$\phi_{xx} - \phi_{tt} - \sin\phi = \eta + \alpha\phi_t + n(x,t). \quad (3.4)$$

Thermal phonons are then solutions of the following stochastic equation:

$$\psi_{xx} = \psi_{tt} - (1 - \eta^2)^{1/2} \psi = \alpha\psi_t + n(x,t). \quad (3.5)$$

When $\alpha=0$, $n(x,t)=0$, these phonons are just classical Klein-Gordon modes with energy given by

$$H_{ph} = \frac{E_0}{16} \int_0^L dx [\psi_x^2 + \psi_t^2 + \psi^2(1 - \eta^2)^{1/2}]. \quad (3.6)$$

The general solution of Eq. (3.5) satisfying the boundary conditions (3.3) is of the form

$$\psi = (2/L)^{1/2} \sum_n A_n(t) \cos(k_n x) \quad (3.7)$$

with

$$k_n = \frac{n\pi}{L} \quad (3.8)$$

and $(2/L)^{1/2}$ being just a normalization factor (for $n=0$ it should be read as $L^{-1/2}$). Substituting (3.7) in (3.5) and applying to both sides of the equation the projection operator $\int_0^L \cos(k_n x) dx$, we obtain

$$A_{n,tt} + \alpha A_{n,t} + [(1 - \eta^2)^{1/2} + k_n^2] A_n = \epsilon_n(t), \quad (3.9)$$

where

$$\epsilon_n(t) = (2/L)^{1/2} \int_0^L n(x,t) \cos(k_n x) dx. \quad (3.10)$$

Using (1.2), we find for the autocorrelation function $R_{\epsilon_n}(t-t')$ and the power spectrum $S_{\epsilon_n}(\omega)$ the same expression as in (2.12) and (2.13). By identifying $[(1 - \eta^2)^{1/2} + k_n^2]$ with ω_n^2 , we see that Eq. (3.9) in the limit $L \rightarrow \infty$ coincides with Eq. (2.0), and therefore, following the same analysis of the preceding section, we obtain that the average energy per phonon mode is

$$\langle H_n \rangle = k_B T. \quad (3.11)$$

No zero-mode energy is present in this case, due to the absence of the soliton in the system. Finally, we remark that the above results do not depend on the particular boundary condition (3.3) used (we could have used generic periodic boundary conditions) as well as on smallness requirements of α and η . The only approximation that has been made in obtaining (2.21), (2.22), and (3.11) is the linearization procedure, which is justified if

$$k_B T \ll E_0, \quad (3.12)$$

as appears evident from Eqs. (2.16) and (2.17).

IV. BROWNIAN MOTION AND DIFFUSION CONSTANT OF A THERMAL SOLITON

We now concentrate on the effect of the α , η , and $n(x,t)$ terms in Eq. (3.4) on the soliton motion (here a soliton is a 2π -kink jump from $-\sin^{-1}\eta$ to $2\pi - \sin^{-1}\eta$). We assume η/α and $k_B T/E_0$ to be small. By introducing the momentum

$$P = -\frac{1}{8} \int_{-\infty}^{+\infty} \phi_x \phi_t dx, \quad (4.1)$$

and differentiating with respect to time, we obtain

$$\frac{dP}{dt} = -\alpha P + \frac{1}{4} \pi \eta + \epsilon(t), \quad (4.2)$$

where we have used Eq. (3.4) to eliminate the ϕ_{tt} term and have defined $\epsilon(t)$ as

$$\epsilon(t) = \frac{1}{8} \int_{-\infty}^{+\infty} \phi_x(x,t) n(x,t) dx. \quad (4.3)$$

Neglecting the noise term, Eq. (4.2) describes the "power balance" motion of a 2π -kink with velocity¹³

$$u_0 = \pm \left[1 + \left(\frac{4\alpha}{\pi\eta} \right)^2 \right]^{-1/2} \quad (4.4)$$

and momentum

$$P_0 = \frac{u_0}{(1-u_0^2)^{1/2}} \quad (4.5)$$

The noise term $n(x,t)$ in Eq. (4.2) introduces fluctuations in the momentum and, from (4.5), in the velocity of the kink. Such fluctuations are readily evaluated by standard techniques (for details see Ref. 7), giving the following for the power spectrum of the process $\Delta u(t) = u(t) - u_0$:

$$S_{\Delta u}(\omega) = 2\alpha(k_B T/E_0) \frac{(1-u_0^2)^{5/2}}{\omega^2 + \alpha^2} \quad (4.6)$$

By assuming $u_0 \ll 1$, Eq. (4.6) reduces to

$$S_u(\omega) = 2\alpha(k_B T/E_0) \frac{1}{\omega^2 + \alpha^2} \quad (4.7)$$

from which we obtain

$$\langle u^2 \rangle = \int_{-\infty}^{+\infty} \frac{d\omega}{2\pi} S_u(\omega) = (k_B T/E_0) \quad (4.8)$$

The time average of the kinetic energy in the Brownian motion of the soliton is then given by

$$\langle E_{\text{sol}} \rangle = \frac{1}{2} E_0 \langle u^2 \rangle = \frac{1}{2} k_B T \quad (4.9)$$

as expected from soliton statistical-mechanics theory.⁸

Finally, from Eq. (4.6) a diffusion constant D for the 2π -kink motion is derived:

$$D = \frac{1}{E_0} (k_B T/\alpha), \quad (4.10)$$

which is just the usual Einstein diffusion constant for the Brownian motion of a particle in a viscous medium (this is a further confirmation of the particlelike nature of the soliton). (See also Ref. 3.)

V. THERMAL SOLITONS AND PHONONS IN JOSEPHSON JUNCTIONS

We will now relate the foregoing sections to a real device as the Josephson junction. We will find the orders of magnitude of the quantities of interest and see if the assumption made in the above analysis holds for Josephson junctions.

The fluxon-rest energy (in laboratory units) for a Josephson junction is

$$E_0 = \hbar\omega_0 = 8\hbar\lambda_J J L / (2e), \quad (5.1)$$

where J is the maximum Josephson current density, L is the length of the junction, and e is the electron charge. λ_J in (5.1) is the Josephson penetration depth given by

$$\lambda_J = (\hbar/2e\mu_0 dJ)^{1/2} \quad (5.2)$$

where d is the magnetic thickness of the oxide layer ($2\lambda_L + t_0$), and μ_0 is the vacuum permeability. From (5.1) we have that for a typical Josephson junction

$$(k_B T/E_0) \approx 10^{-4} - 10^{-5}, \quad (5.3)$$

which justifies the assumption (3.12) made in the analysis.

The Josephson plasma frequency is

$$\omega_p = (2eJt_0/\epsilon_0\epsilon_r\hbar)^{1/2}, \quad (5.4)$$

where ϵ_r and ϵ_0 are, respectively, the relative dielectric constant of the oxide layer and the dielectric constant of the vacuum, while t_0 is the thickness of the oxide layer. For a plasmon described in Sec. III we have that the splitting of the energy level is

$$E_{p1}^q = \hbar\omega_p\omega_n \quad (5.5)$$

with ω_n given by $[(1-\eta^2)^{1/2} + (n\pi/L)^2]^{1/2}$. We have then that the ratio $k_B T/E_{p1}^q$ is of the order of magnitude $1-10$, i.e., the quantum energy levels are separated by a quantity comparable with $k_B T$. To have a rough estimate of the energy-level separation for a fluxon, we can use the analogy of a particle in a box. This gives

$$E_{f1}^q = \frac{\pi^2\hbar^2}{2M_0} \frac{n^2}{L^2} \approx 10^{-4}\hbar\omega_p, \quad (5.6)$$

i.e., for a fluxon the separation in the energy levels is smaller than $k_B T$ by a factor of the order $10^{-3}-10^{-4}$. This numerical manipulation indicates that for a typical Josephson junction fluxon quantitation is *not* necessary, while it is necessary for plasmons (E_{p1}^q being of the same order of magnitude as $k_B T$). In Ref. 6 the effects of quantum plasmons on the fluxon motion have been calculated. It turns out that they are several orders of magnitude smaller than the direct influence of the thermal reservoir on the soliton evaluated in this paper, and therefore, in our context, completely negligible.

Finally, in closing this section it is worth noting that if $k_B T/E_0$ is very small, a statistical-mechanical description of fluxons in Josephson junctions is meaningless. However, the method used in the preceding section is still useful to study the interactions between plasmons and fluxons. (See Ref. 7 for the case of Josephson oscillators.)

VI. CONCLUSION

It has been shown that the effect of a thermal reservoir on the sine-Gordon system can be studied by using standard methods of stochastic processes. Both phonons and solitons are found to be thermalized in a way that the phonons will have an average energy of $k_B T$ per mode, while solitons will have an energy of $\frac{1}{2}k_B T$. These results are in agreement with those obtained by using a statistical-mechanics approach for a "dilute" solution gas.⁸ The main assumption used in our derivation has been $k_B T \ll E_0$ (to justify the linearization procedure). Second-order effects [in the small quantity $(k_B T/E_0)$], such as interaction between phonon modes and solitons,^{6,9} have been neglected therefore. Finally, in closing this paper we wish to point out that in spite of the particularity of the model used, the results obtained are sufficiently general to be extended to other equations of the nonlinear Klein-Gordon class, such as ϕ^4 , double sine-Gordon, etc. As a matter of fact, the only difference in the analysis will be the presence of additional bound states in the linear phonon eigenvalue problem. By following arguments

similar to those used in the present paper, however, it is easily shown that each of these additional bound states carries a thermal-average energy of $k_B T$. This energy will not increase the energy of the center of mass of a soliton-like solution of these more general models, but it will increase the energy of the internal degrees of freedom (motion around the center of mass) of these excitations.¹⁴

ACKNOWLEDGMENTS

One of us (M. S.) would like to thank the Laboratory of Applied Mathematical Physics (LAMF) (where part of this paper was done), for the kind hospitality received, the Danish Ministry of Education, and the European Research Office of the United States Army (Contract No. DAJA-37-82-C-0057) for providing financial support.

*Permanent address: Istituto di Fisica, Università degli Studi di Salerno, I-84100 Salerno, Italy.

¹S. E. Trullinger, M. D. Miller, R. A. Guyer, A. R. Bishop, F. Palmer, and J. A. Krumhansl, *Phys. Rev. Lett.* **40**, 206 (1978).

²H. J. Mikeska, *J. Phys. C* **11**, 129 (1978); K. Maki, *J. Low Temp. Phys.* **41**, 327 (1980); D. J. Bergman, E. Ben Jacob, Y. Imry, and K. Maki, *Phys. Rev. A* **27**, 3345 (1983).

³M. Reimossenet, *Solid State Commun.* **27**, 681 (1978); L. Gunther and Y. Imry, *Phys. Rev. Lett.* **44**, 1225 (1980).

⁴M. Büttiker and R. Landauer, *Phys. Rev. A* **23**, 1397 (1981).

⁵D. J. Kaup, *Phys. Rev. B* **27**, 6787 (1983).

⁶M. Salerno and A. C. Scott, *Phys. Rev. B* **26**, 2474 (1982).

⁷E. Joergensen, V. P. Koshelets, R. Monaco, J. Mygind, M. R. Samuelsen, and M. Salerno, *Phys. Rev. Lett.* **49**, 1093 (1982).

⁸A. R. Bishop, J. A. Krumhansl, and S. E. Trullinger, *Physica (Utrecht)* **1D**, 1 (1980).

⁹Y. Wada and H. Ishiuchi, *J. Phys. Soc. Jpn.* **51**, 1372 (1982).

¹⁰See, for example, A. Papoulis, *Probability, Random Variables, and Stochastic Processes* (McGraw-Hill, New York, 1965).

¹¹J. Rubinstein, *J. Math. Phys.* **11**, 258 (1970).

¹²O. H. Olsen and M. R. Samuelsen, *Phys. Rev. B* **28**, 210 (1983).

¹³D. W. McLaughlin and A. C. Scott, *Phys. Rev. A* **18**, 1652 (1978).

¹⁴M. Salerno and M. R. Samuelsen (unpublished).

Magnetic field dependence of microwave radiation in intermediate-length Josephson junctions

M. P. Soerensen, R. D. Parmentier, P. L. Christiansen, and O. Skovgaard

Laboratory of Applied Mathematical Physics, The Technical University of Denmark, DK-2800 Lyngby, Denmark

B. Dueholm, E. Joergensen, V. P. Koshelets, O. A. Levring, R. Monaco, J. Mygind, N. F. Pedersen, and M. R. Samuelson

Physics Laboratory I, The Technical University of Denmark, DK-2800 Lyngby, Denmark

(Received 21 December 1983)

Experimental measurements of current-voltage structure and emitted X-band radiation in applied magnetic field from overlap-geometry Josephson tunnel junctions of normalized length about 2 are compared with numerical simulations obtained with the use of a perturbed sine-Gordon model. The simulations furnish the current and field dependence of the oscillation configuration, from which can be calculated average voltages, frequencies, and power spectra. Simulation and experimental results are in good agreement with regard to the lobe structure of the height of the first zero-field step and/or second Fiske step in magnetic field and the field dependence of the radiation frequency within the various lobes, including details such as hysteresis between lobes. The simulations predict an alternation of the dominant frequency component with increasing field that accounts well for the experimental observations. The usefulness and limitations of cavity-mode analyses, both single-mode and multimode, are evidenced by comparison with the simulation results.

I. INTRODUCTION

Fluxon (soliton) propagation¹ has been by now established as the essential physical mechanism underlying many of the observed experimental properties of long Josephson tunnel junctions. In particular, the appearance of both zero-field steps (ZFS's) and Fiske steps (FS's) in the current-voltage (I - V) characteristics of such junctions and the emission of microwave radiation from junctions when biased on these steps seem to be explainable in terms of fluxon dynamics.²⁻⁵ A number of different approaches have been employed in the literature to account for the available experimental observations. These include perturbative expansions of the basic soliton equation involved (sine-Gordon equation),⁶ analytic extensions of small-junction theory (cavity-mode-interaction analyses),⁷ and mechanical analog⁸ and digital computer⁹ simulations (the references cited are intended to be representative, not exhaustive). Moreover, direct dynamic measurements at the single-fluxon level are beginning to appear in the literature.^{10,11}

The perturbative approach is most suited for studying the behavior of low-order steps on very long junctions, inasmuch as the usual point of departure here consists of the exact analytic solutions of the sine-Gordon equation on the infinite spatial interval. Multimode extensions of small-junction theory, on the other hand, should presumably be most appropriate for relatively short junctions. For junctions which are neither very long nor very short, one would expect *a priori* that neither of these two approaches could be counted on to give reliable results. In such cases, direct simulation would seem to be indispensable.

The present paper is an attempt to elucidate further and

in more detail just this case, viz., the dynamics underlying the behavior of intermediate-length Josephson junctions. To this end we compare the results of new experimental measurements of I - V structure and microwave emission in magnetic field with the results of detailed numerical simulations. The agreement that emerges is quite convincing. For simplicity, attention is focused primarily on the first zero-field step (ZFS1) and on the second Fiske step (FS2) in junctions of normalized length of about 2. Since the voltage positions of ZFS1 and FS2 approximately coincide, we refer in the following to the step ZFS1/FS2. The numerical simulations are compared also with approximate analytic results, and the usefulness and limitations of the latter are clarified.

The paper is structured as follows: Section II contains a description of the mathematical model used and the techniques employed in its analysis. The results of this analysis are presented in Sec. III. The experimental measurements performed are described and discussed in Sec. IV. Finally, Sec. V contains our concluding comments.

II. MATHEMATICAL MODEL AND COMPUTATION TECHNIQUES

The mathematical model studied is the perturbed sine-Gordon equation,⁹

$$\phi_{xx} - \phi_n - \sin\phi = \alpha\phi_t - \beta\phi_{xxt} - \gamma, \quad (1a)$$

$$\phi_x(0,t) = \phi_x(L,t) = \eta, \quad (1b)$$

appropriate to an overlap-geometry junction.¹² Here, ϕ is the usual Josephson-phase variable, x is distance along the junction normalized to the Josephson penetration depth λ_J , t is time normalized to the inverse of the Josephson

plasma (angular) frequency ω_0 , and subscripts denote partial derivatives (see Ref. 9 for details of the normalizations). The model contains five parameters: α , β , γ , L , and η . The term in α represents shunt (quasiparticle) loss. The β term models dissipation due to the surface resistance of the superconducting films. The constant γ measures a uniformly distributed bias current normalized to the maximum zero-voltage Josephson current. The constant η is a normalized measure of the external magnetic field which determines the boundary conditions [Eq. (1b)] at the two ends of the junction of normalized length L . In this numerical study the dissipative and length parameters were fixed at $\alpha=0.05$, $\beta=0.02$, and $L=2$. These were chosen to be representative of typical physical values without, however, modeling any one specific junction. The bias current and magnetic field parameters were varied in the ranges $0 \leq \gamma \leq 1$, $0 \leq \eta \leq 6$.

Equations (1) were integrated from initial conditions either similar to Eqs. (2) of Ref. 13 or (more often) using the final ϕ and ϕ_t distributions from runs at nearby points in parameter space. The integration was carried out using the implicit finite-difference method described in detail in Ref. 9, with space and time intervals set to 0.02 and 0.01, respectively. Numerical accuracy and stability were verified by halving and doubling these intervals. During each run the time-averaged value of the voltage at the two ends of the junction and the power spectrum of the voltage at the left ($x=0$) end were calculated. Here, voltage is defined as ϕ_t , which represents the physical voltage normalized to $\hbar\omega_0/2e$, where \hbar is Planck's constant divided by 2π , and e is the magnitude of the electronic charge. These quantities were calculated over an integral number of oscillation periods during the last approximately 50 normalized time units of each run. The power spectra were calculated by means of a fast Fourier transform using a simple rectangular window.¹⁴ The values of $\langle \phi_t \rangle$ were calculated both from the elementary definition of average and the zero-frequency components of the power spectra.

Two checks were employed to assure that the average voltages and the power spectra were calculated over steady-state, not transient, dynamic configurations: (i) The values of $\langle \phi_t \rangle$ at the two junction ends were compared. Physically and mathematically, the time-averaged voltage must be constant along the length of the junction. (ii) The quantity $\langle \phi_t \rangle / 2\pi f$, where f is the fundamental oscillation frequency, was calculated. From the Josephson frequency relation, this quantity, in steady state, must be an integer whose value (1 or 2 in the present case) depends upon the type of oscillation present.⁹ If either of these conditions was not satisfied to within specified limits the time duration of the run was increased.

III. NUMERICAL RESULTS

Figure 1 shows the magnetic field diffraction pattern of ZFS1/FS2. In this figure, circles and diamonds are the numerically computed top of the step. Circles were calculated by increasing γ at constant η ; diamonds were determined by varying η at constant γ (as will be seen later, the difference is significant). Small arrows near the diamonds

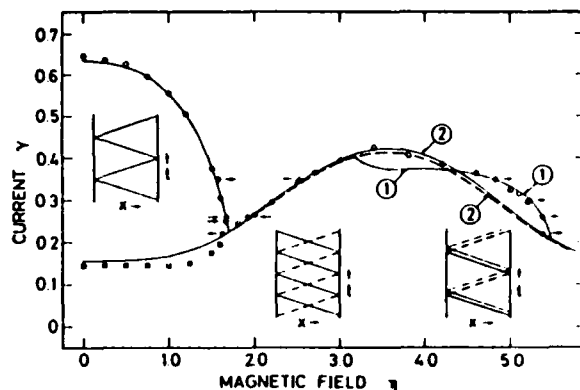


FIG. 1. Magnetic field diffraction pattern of ZFS1/FS2. Circles: step top calculated numerically at constant η . Squares: step bottom calculated numerically at constant η . Diamonds: step top calculated numerically at constant γ . Arrows near diamonds indicate direction of field variation. Solid curve (marked 1 and 2): Enpuku *et al.* multimode theory. Dashed curve: Kulik single-mode theory. Enpuku and Kulik curves coincide at the bottom of the first lobe. Insets show approximate dynamic trajectories in the various η regions: solid lines are fluxons or antfluxons; dashed lines are plasma waves.

indicate the direction in which η was varied near the maximum point. Beyond the maximum points, the junction switched to a different dynamic state, most often to the McCumber-Stewart hysteresis curve at the corresponding value of γ . This fact was evidenced by abrupt changes in the value of $\langle \phi_t \rangle$, the voltage waveform, and the corresponding power spectrum. In zero magnetic field, the form of the McCumber-Stewart hysteresis curve can be approximated by^{15,2}

$$\gamma = 4\alpha E(k) / \pi k, \quad (2a)$$

$$\langle \phi_t \rangle = \pi / kK(k), \quad (2b)$$

where $K(k)$ and $E(k)$ are, respectively, the complete elliptic integrals of the first and second kinds of modulus k . From Eqs. (2) it follows that for $k \rightarrow 0$, $\gamma \rightarrow \alpha \langle \phi_t \rangle$, i.e., the McCumber-Stewart curve approaches asymptotically the Ohmic line, whereas for $k \rightarrow 1$, $\langle \phi_t \rangle \rightarrow 0$, and $\gamma \rightarrow 4\alpha/\pi$. Equations (2) continue to hold as a rough approximation even in the presence of magnetic field, at least for $\eta \leq 1$.

The squares in Fig. 1 are the numerically computed bottom of the step, calculated by decreasing γ at constant η . As will become clear from Figs. 2–6, it is possible to determine numerically the precise bottom of the step in the first lobe of the diffraction pattern, but this is no longer the case in the second lobe. Beyond the minimum points, the solution followed the McCumber-Stewart curve down for a certain distance, after which it switched abruptly to a static, zero-voltage state. The lowest γ value for which such switching was observed was $0.06 \leq \gamma < 0.07$, which is consistent with the value $4\alpha/\pi = 0.064$ estimated from Eq. (2a).

The dashed curve in Fig. 1 has been calculated from the Kulik theory¹⁶ for FS2. The input parameter for this

theory is the quantity $Z_n = L^2 Q_n / n^2 \pi^2$, where n is the step number (2, in our case) and Q_n is the quality factor of the n th mode. Following Enpuku *et al.* (Ref. 7) Q_n is defined by

$$\frac{1}{Q_n} = \frac{L\alpha}{n\pi} + \frac{n\pi\beta}{L} \quad (3)$$

Insertion of parameter values thus yields $Z_2 = 1.2867$. The Kulik theory gives the maximum height of the step above the Ohmic current. Accordingly, to compare with numerical (or experimental) results it is necessary to add this component to the Kulik value. Since, from our numerical results, the top of FS2 is at $\langle \phi_1 \rangle \approx 3.1$, a constant (independent of η) value of $\alpha(\phi_1) = 0.155$ has been added to the Kulik component in drawing the dashed curve in Fig. 1.

The Kulik theory is seen to predict the maximum points of the second lobe up to $\eta \approx 4$. However, for the maximum points of the first lobe and for the second lobe for $\eta > 4$, the theory fails. To predict these results more modes must be included in the computations. Following Enpuku *et al.*⁷ we have used five modes with the quality factor Q_n given by Eq. (3) with $n = 1, 2, \dots, 5$. We have solved Eqs. (10)–(12) in Ref. 7 by means of a standard routine.¹⁷ The results are shown as the solid curve in Fig. 1. The Enpuku theory is seen to predict the maximum points of the first lobe very well. The maximum values on the second lobe up to $\eta = 5.5$ are also in agreement. However, between $\eta = 3.1$ and 5.5 the Enpuku theory predicts two curves for the maximum values. The curves are marked 1 and 2 in accordance with a major contribution to the solution from the first and second cavity modes respectively. Curve 2 lies close to the Kulik curve, in agreement with the fact that this latter curve was computed by means of mode 2 exclusively. The numerically computed maximum values (circles) agree with the upper curves (i.e., curve 2 in the interval $\eta = 3.1$ –4.4 and curve 1 in the interval $\eta = 4.4$ –5.5). Just above the lower curves (i.e., curve 1 for $\eta = 3.1$ –4.4 and curve 2 for $\eta = 4.4$ –5.5) the computer results exhibit changes in the contents of cavity modes from mode 1 to mode 2 above curve 1 and vice versa above curve 2. The accompanying hysteresis phenomena are discussed below.

Figures 2–6 depict five vertical (constant- η) slices through the diffraction pattern. Figure 2(a) shows the current dependence of the power levels of the first two Fourier harmonics of the voltage at the left end of the junction in zero magnetic field. Power levels are given by $10 \ln |A|^2 + 100$, A being the voltage Fourier component. The ac components are thus arbitrarily normalized to $\phi_1^2 = 10^{-10}$. Since no loading effects are included in the model, all power levels calculated should be considered ideal, available values. Figure 2(b) shows the current dependence of the first harmonic frequency f_1 of the oscillation. Since average voltage and frequency are proportional (in steady state) through the relations $\langle \phi_1 \rangle = 4\pi f_1 = 2\pi f_2$, Fig. 2(b) is effectively the current-voltage characteristic of the step. We have chosen to plot this characteristic in frequency rather than in voltage because in the laboratory, frequency can be measured much more precisely (although perhaps less easily) than voltage.

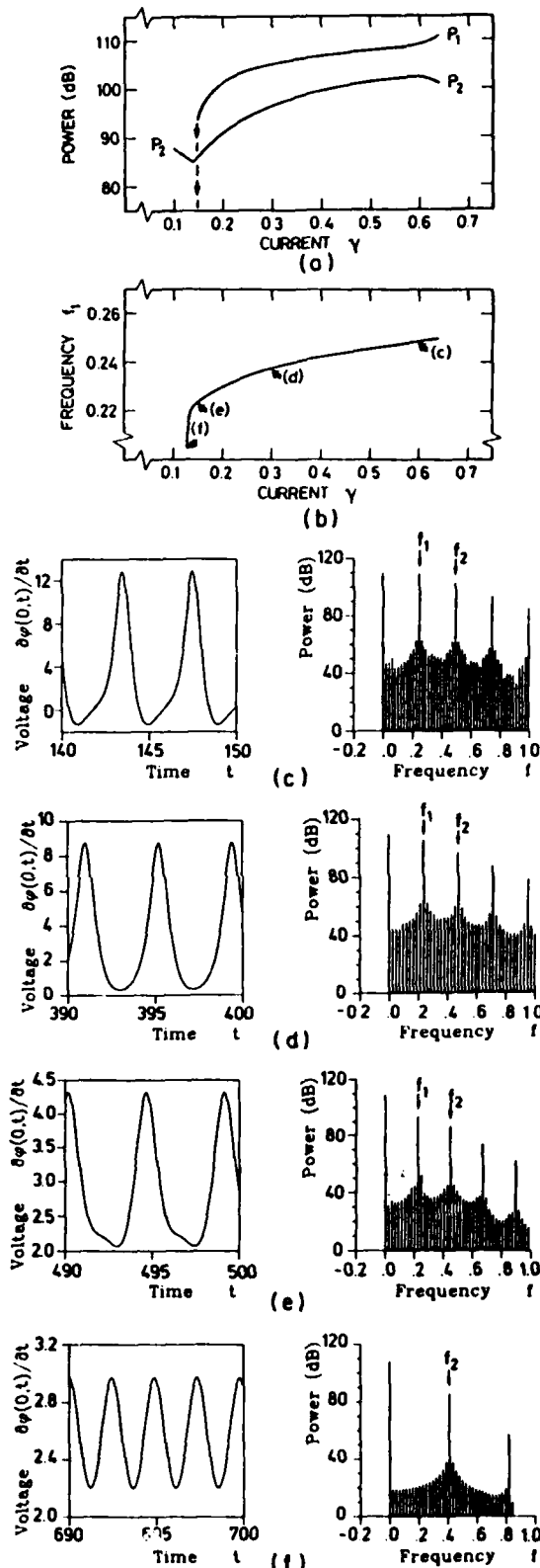


FIG. 2. Section through diffraction pattern at $\eta = 0$. (a) Power levels of first two Fourier voltage components at $x = 0$, normalized to $\phi_1^2 = 1.0 \times 10^{-10}$. (b) First-harmonic frequency. Voltage waveform at $x = 0$ and corresponding power spectrum are shown for (c) $\gamma = 0.60$, (d) $\gamma = 0.30$, (e) $\gamma = 0.15$, and (f) $\gamma = 0.13$.

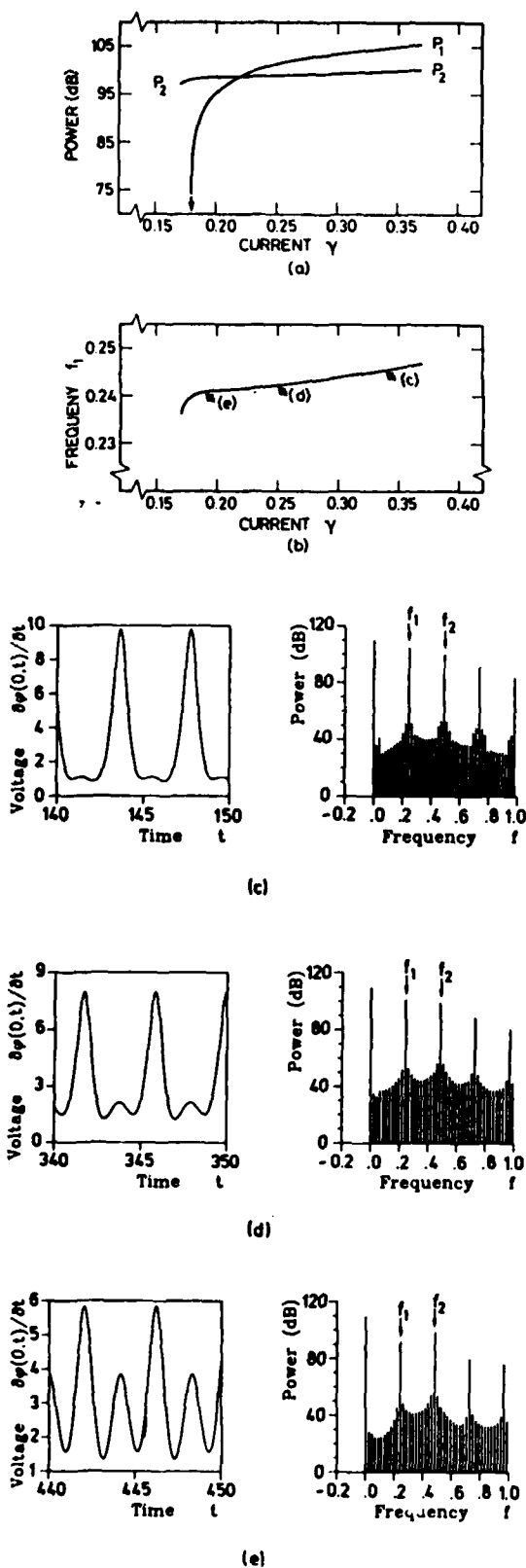


FIG. 3. Section through diffraction pattern at $\eta=1.5$. (a) Power levels of first two Fourier voltage components at $x=0$, normalized to $\phi_0^2=1.0 \times 10^{-10}$. (b) First-harmonic frequency. Voltage waveform at $x=0$ and corresponding power spectrum are shown for (c) $\gamma=0.34$, (d) $\gamma=0.25$, and (e) $\gamma=0.19$.

Figures 2(c)–(f) show the voltage waveform and part of the corresponding power spectrum at the four points indicated by arrows in Fig. 2(b). A comparison of Figs. 2(a)–2(e) with results from the literature [see, in particular, Fig. 17 of Ref. 9 and Fig. 5(a) of Ref. 2] leaves no doubt that the oscillation depicted in Fig. 2 is the fluxon oscillation corresponding to ZFS1. Finally, a comparison of Figs. 2(e) and 2(f) makes clear why it is possible to determine precisely the bottom of the step in the first lobe of the diffraction pattern: At a certain value of the bias current ($0.14 \leq \gamma < 0.15$ in the present case) the f_1 component of the oscillation abruptly disappears, and a new oscillation evolves for which the dominant component is at f_2 .

Figure 3 shows a similar vertical slice through the diffraction pattern at a point near the right-hand extremity

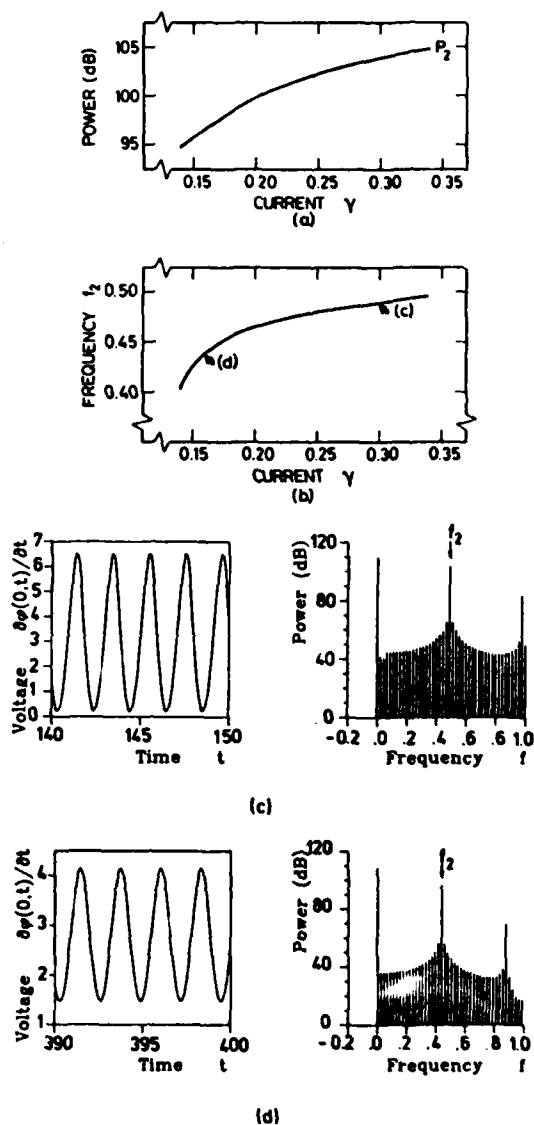


FIG. 4. Section through diffraction pattern at $\eta=2.5$. (a) Power levels of second Fourier voltage component at $x=0$, normalized to $\phi_0^2=1.0 \times 10^{-10}$ (P_1 is absent). (b) Second-harmonic frequency. Voltage waveform at $x=0$ and corresponding power spectrum are shown for (c) $\gamma=0.30$ and (d) $\gamma=0.16$.

of the first lobe ($\eta = 1.5$). Here, the behavior of the oscillation near the top of the step is qualitatively quite similar to that shown in Fig. 2. As γ is decreased, however, a marked difference is seen: The ratio of the f_1 power P_1 to the f_2 power P_2 steadily decreases until, near the bottom of the step, P_2 in fact dominates. Since f_2 is the dominant frequency of FS2, the nature of the step at $\eta = 1.5$ may be described as ZFS1-like near the top and FS2-like near the bottom. It should be noted, however, that the transition between the two oscillation configurations is here relatively gradual, rather than abrupt.

Figure 4 shows a vertical slice at $\eta = 2.5$, in the left-hand side of the second lobe of the diffraction pattern. Here the oscillation is purely FS2-like over the entire extent of the step. The power P_1 is lost in the background

noise (the noise here is of numerical, not physical, origin), and P_2 is the dominant component. The fact that the next-highest component, at $f = 2f_2$, lies 20 dB or more below P_2 , explains why the Kulik theory, which assumes

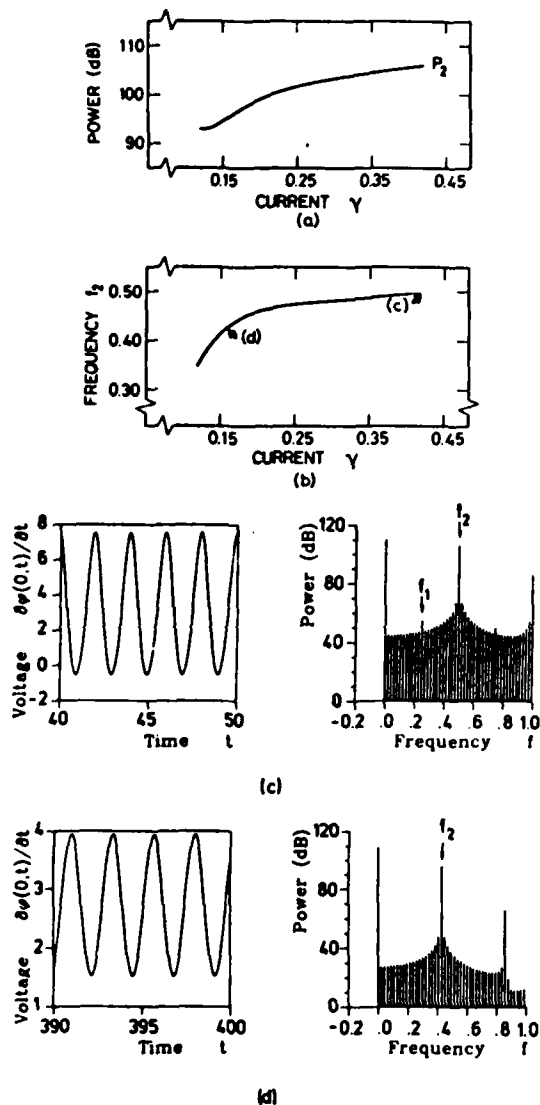


FIG. 5. Section through diffraction pattern at $\eta = 3.4$. (a) Power levels of second Fourier voltage component at $x = 0$, normalized to $\phi_1^2 = 1.0 \times 10^{-10}$ (P_1 is absent or very small). (b) Second-harmonic frequency. Voltage waveform at $x = 0$ and corresponding power spectrum are shown for (c) $\gamma = 0.42$ and (d) $\gamma = 0.16$.

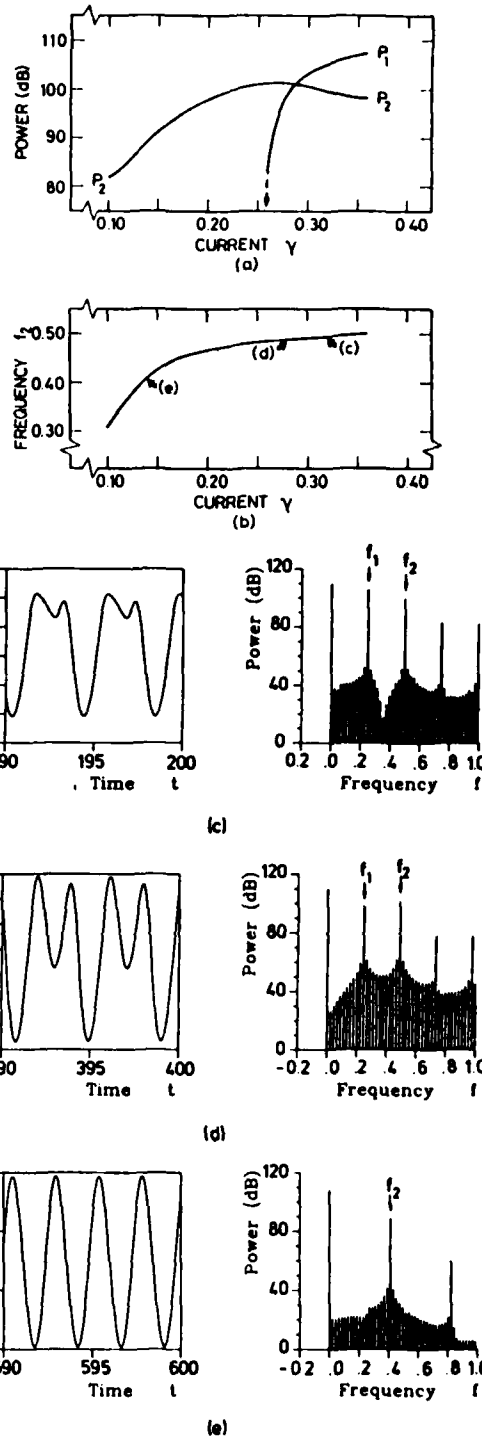


FIG. 6. Section through diffraction pattern at $\eta = 4.6$. (a) Power levels of first two Fourier voltage components at $x = 0$, normalized to $\phi_1^2 = 1.0 \times 10^{-10}$. (b) Second-harmonic frequency. Voltage waveform at $x = 0$ and corresponding power spectrum are shown for (c) $\gamma = 0.32$, (d) $\gamma = 0.28$, and (e) $\gamma = 0.14$.

a single mode at $f=f_2$, gives a reasonable description of the oscillation in this region, as seen in Fig. 1. The difficulty in determining precisely the bottom of the step in the second lobe is now also apparent: f_2 is the dominant component of both FS2 and the McCumber-Stewart curve. As γ is decreased, the step here merges gradually with the McCumber-Stewart curve without any abrupt changes, in contrast with what happens in the first lobe.

The behavior of the oscillation along a vertical slice at the peak of the second lobe ($\eta=3.4$) is shown in Fig. 5. Here, the situation is very similar to that depicted in Fig. 4 except at the very top of the step, where, with increasing γ , the f_1 component just begins to emerge from the background, as seen in Fig. 5(c).

This tendency continues more markedly in Fig. 6, which shows a vertical slice at $\eta=4.6$. Here, recalling the situation depicted in Fig. 3, the step is ZFS1-like near the top and FS2-like near the bottom. As in Fig. 3, the transition here between the two oscillation configurations is relatively smooth.

The information contained in Figs. 2–6 is summarized in a highly schematic and approximate fashion in the insets of Fig. 1. These show trajectories in the $x-t$ plane, with fluxons and antfluxons indicated by solid lines and localized plasma waves indicated by dashed lines. The locations in η of the three insets in Fig. 1 indicate roughly the regions where the corresponding dynamic configurations are observed (we emphasize once again, however, that the transitions between the various configurations are gradual).

A rather different perspective on the nature of the oscillations is obtained by taking horizontal (constant- γ) slices through the diffraction pattern. Two such slices, at $\gamma=0.35$ and 0.26 , are shown in Figs. 7 and 8. Figure 7 shows the magnetic field dependence of the frequency f_2 (proportional to the voltage) in the two slices, while Fig. 8 shows the corresponding behavior of the power levels, P_1 and P_2 , at f_1 and f_2 . The salient facts that emerge from these two figures may be summarized as follows: (i) The essential, overall dependence of the oscillation frequency on magnetic field is the inverse (qualitatively) of that of the diffraction pattern; where the height of the step decreases with field, the frequency increases, and vice versa.

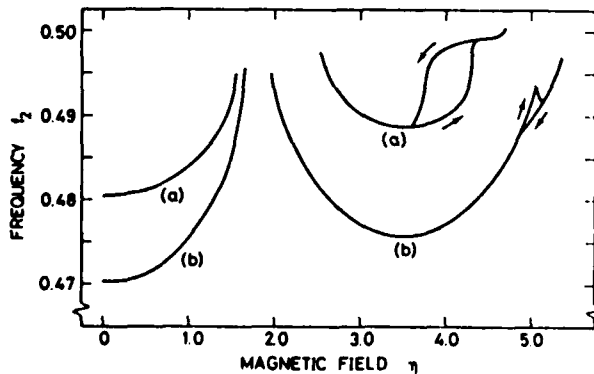


FIG. 7. Second-harmonic frequency section through diffraction pattern at (a) $\gamma=0.35$ and (b) $\gamma=0.26$. Arrows indicate hysteresis.

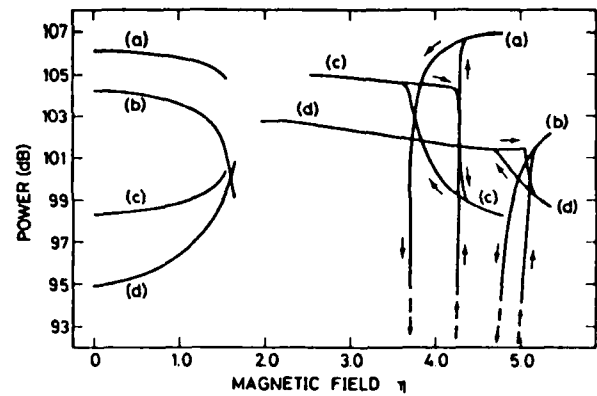


FIG. 8. Power section through diffraction pattern at constant γ . Powers measured at $x=0$ and normalized to $\phi_0^2 = 1.0 \times 10^{-10}$. (a) First harmonic P_1 at $\gamma=0.35$. (b) First harmonic P_1 at $\gamma=0.26$. (c) Second harmonic P_2 at $\gamma=0.35$. (d) Second harmonic P_2 at $\gamma=0.26$. Arrows indicate hysteresis.

(ii) In the first lobe of the diffraction pattern the behavior is quite regular; the frequency increases monotonically with field, and P_1 is the dominant component. We note parenthetically here that this frequency behavior may be different for longer junctions.^{18,19} (iii) In the left half of the second lobe the behavior is also regular; the frequency

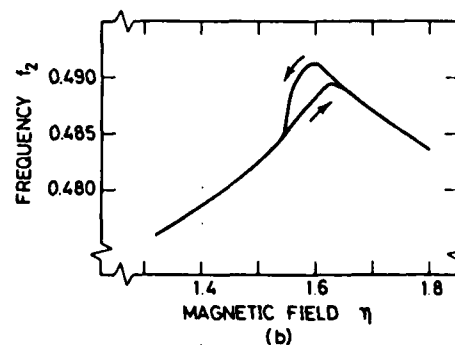
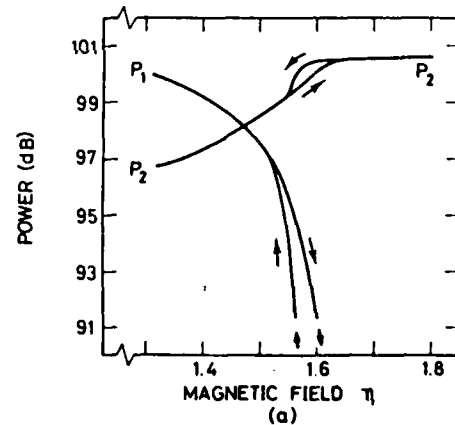


FIG. 9. Partial section through diffraction pattern at $\gamma=0.21$. (a) Power levels of first two Fourier voltage components at $x=0$, normalized to $\phi_0^2 = 1.0 \times 10^{-10}$. (b) Second-harmonic frequency. Arrows indicate hysteresis.

here decreases monotonically with field, reaching a minimum in correspondence with the peak of the second lobe, and P_2 is strongly dominant (the f_1 component lies within the background noise). (iv) In the right half of the second lobe P_1 once again becomes dominant. The cross-over point, where $P_1 \approx P_2$, occurs at larger values of η for decreasing γ . These observations suggest that it might in fact be more appropriate to refer here to a third lobe, rather than to a half of the second lobe. (v) A strongly hysteretic behavior of both frequency and power is observed in the right half of the second lobe (i.e., third lobe). This fact may explain why experimental measurements [see, e.g., Paternò and Nordman²⁰ as well as Fig. 12(a) below] often display notable irregularities in this region.

Figure 9 shows a small section of a horizontal slice at $\gamma=0.21$ in the region just under the juncture point of the first and second lobes. Since $\gamma=0.26$ and 0.35 both lie above this juncture point, the curves in Figs. 7 and 8 are discontinuous in this region. The major conclusions to be drawn from Fig. 9 are similar to those drawn above: (i) The qualitative shape of the field dependence of the oscillation frequency is the inverse of that of the diffraction pattern. (ii) Hysteresis is observed in η regions where the dominant mode is changing.

IV. EXPERIMENTAL RESULTS

The numerical calculations discussed above were compared with measurements on overlap geometry Nb-Nb-oxide-Pb junctions having parameters comparable with those used in the calculations. Although the discussion below is appropriate for the many junctions investigated,²¹ two junctions were measured in detail. Junction no. S10-5-1 has dimensions $479 \times 179 \mu\text{m}^2$, maximum zero-voltage current $I_{c0}=1.40$ mA, and an estimated normalized length, L , of 2. Junction no. 65H7 has dimensions $467 \times 67 \mu\text{m}^2$, $I_{c0}=0.53$ mA, and L slightly less than 2. From independent measurements on similar junctions an estimate of α and β can be made.²² The estimate is reasonably consistent with the values $\alpha=0.05$ and $\beta=0.02$ used in the calculations, although the experimental values are probably somewhat smaller. The parameter values of both junctions are such that the fundamental soliton frequency f_1 may be detected with an X-band receiver (8–12 GHz). Any radiation at f_2 , however, is outside the frequency band of the detector used. The microwave receiver had an overall noise figure of about 8 dB. By using a spectrum analyzer both the power and the frequency of microwave signals from the junction could be measured. Generally, the received power was 25 dB or less above the physical noise level of the receiver. All data discussed here were taken at 4.2 K.

To investigate the fluxon dynamics the following measurements were performed: (i) I - V curves of the steps. (ii) The magnetic field dependence of the maximum height of the steps. (iii) The magnetic field dependence of the voltage of the steps with the bias current as a parameter. (iv) The power and frequency of the f_1 radiation emitted from the junction.

Figure 10 shows the low-voltage part of the I - V curve in zero magnetic field of junction no. S10-5-1. Three

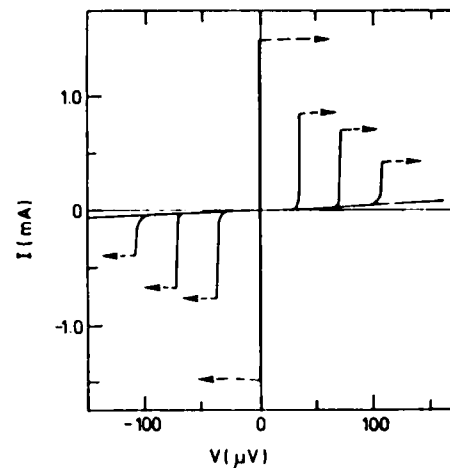


FIG. 10. I - V curve of junction no. S10-5-1, showing three zero-field steps. The dashed curves indicate switching.

ZFS's are seen. The high-voltage part omitted in Fig. 10 only shows the usual increase in current at the energy gap voltage. The dashed lines show switching at the top of the supercurrent and the three ZFS's. The I - V curve of the ZFS's is obtained by decreasing the current to obtain a bias point just below the foot of the ZFS's and then increasing the current again. This I - V curve is typical of the samples investigated. Although not shown with sufficient voltage resolution, the shape of ZFS1 may be compared with Fig. 2(b).

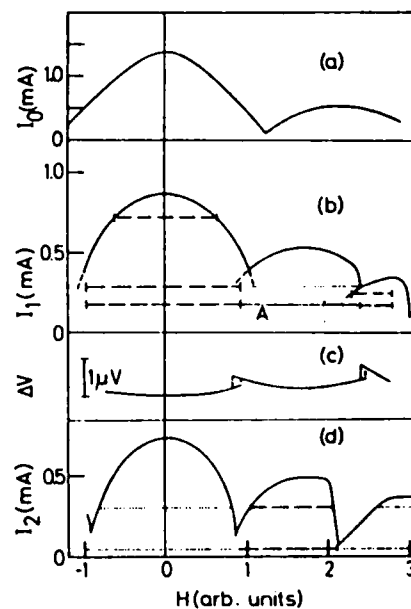


FIG. 11. Junction no. S10-5-1. (a) Magnetic field dependence of the maximum zero-voltage current. (b) Magnetic field dependence of the height of ZFS1/FS2. (c) Voltage tuning of ZFS1/FS2 corresponding to bias level A in (b). (d) Magnetic field dependence of the height of ZFS2/FS4. The dashed lines in (b) and (d) show examples of parameter regions where $f = f_1$ radiation was observed. The dotted lines show parameter regions where $f = f_1$ radiation was not observed.

Figures 11(a) and 11(b) show the magnetic field dependence of the maximum zero-voltage current and of ZFS1/FS2, respectively. Note that the lobe pattern of ZFS1/FS2 is in good qualitative agreement with the calculated one in Fig. 1. In fact, the agreement here is at least semiquantitative: The ratio of the zero-field current in Fig. 11(b) to that in Fig. 11(a) is 0.63; the corresponding value from Fig. 1 is $0.64 < \gamma \leq 0.65$. The extrapolated zero of the first lobe in Fig. 11(b) occurs at a field value approximately equal to that seen for the extrapolated zero of the first lobe in Fig. 11(a) (this is a generally observed experimental fact). In terms of the normalized field η , the extrapolated zero of the first lobe of the zero-voltage current occurs at $\eta=2$ for very long junctions (the exact value for shorter junctions, which is the same for the overlap and the in-line geometries, may be calculated from the theory of Owen and Scalapino²³). Extrapolating to $\gamma=0$, the first lobe in Fig. 1 also yields $\eta \approx 2$. The dashed lines show examples of parameter regions where $f=f_1$ radiation (at approximately 9 GHz) was observed. In general, the $f=f_1$ radiation was observed in the first and third lobes but not in the second lobe. This is in agreement with the results of the numerical calculations, in particular Fig. 8. By comparison with the calculations the reason for the absence of radiation in the second lobe (FS2) is that here the $f=f_2$ radiation is at presumably ~ 18 GHz, outside the range of the receiver. Figure 11(c) shows, for a bias current corresponding to A in Fig. 11(b), the magnetic field tuning of the voltage of ZFS1/FS2 (the absolute value of the voltage is approximately $35 \mu\text{V}$). Figure 11(c) is in good qualitative agreement with the calculation of Fig. 7, showing both the increase in frequency (voltage) as the border regions of the lobes are approached, and the hysteresis there. From the voltage curve, however, it cannot be decided whether it is the $f=f_1$ or the $f=f_2$ radiation that is dominant. Thus, determination of the fluxon-mode configuration requires a measurement of the frequency of the emitted microwave radiation. Such a measurement is described below (Fig. 12). Figure 11(d) shows the lobe pattern of the second step although no corresponding numerical calculations have been performed for this step. The dashed lines show examples of parameters where $f=f_1$ radiation was observed. In general, no such radiation was observed in the first and third lobes; however, $f=f_1$ radiation was observed everywhere in the second lobe. Most likely, the soliton configuration in the first lobe is that of a symmetric fluxon-antifluxon mode (with $f=f_2$). This is in apparent contradiction with measurements on other samples⁴ where the $f=f_1$ radiation was also measured on ZFS2 in zero magnetic field, but the difference may simply be a manifestation of the two soliton configurations, symmetric ($f=f_2$) and bunched ($f=f_1$), that have been demonstrated numerically for ZFS2.⁹ On junction no. 65H7, in fact, the bunched mode was observed on ZFS2. In the second lobe (FS4) a three-fluxon-one-antifluxon mode would give the right frequency (f_1) and voltage; however, other configurations are also possible.

Figure 12(a) shows the diffraction pattern for ZFS1/FS2 of junction no. 65H7. Qualitatively, it is quite similar to Fig. 11(b); however, the right half of the second

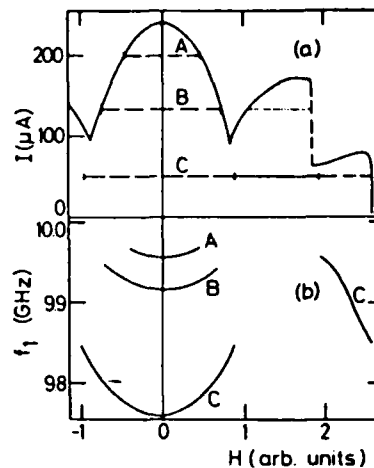


FIG. 12. Junction no. 65H7. (a) Magnetic field dependence of the height of ZFS1/FS2. The dashed lines show examples of parameters where $f=f_1$ radiation was observed. The dotted lines show parameter regions where $f=f_1$ variation was not observed. (b) Frequency of the $f=f_1$ radiation corresponding to bias levels A, B, C in (a).

lobe appears somewhat anomalous. For this measurement the hysteresis phenomena between lobes were observed but not carefully mapped. As indicated by the lines A, B, C for different constant bias currents, $f=f_1$ radiation was observed in the first and third lobes, but not in the second. Figure 12(b) shows a measurement of the frequency of the emitted $f=f_1$ radiation corresponding to bias currents A, B, C in Fig. 12(a). The positive frequency tuning in the first lobe is in good agreement with Fig. 7. The absence of the $f=f_1$ radiation in the second lobe and the reappearance of such radiation at the transition between the second and third lobes are also in qualitative agreement with the numerical calculation of Fig. 8. As noted in connection with Figs. 7 and 9 the frequency tuning resembles the inverse of the diffraction pattern. Qualitatively, curve C in Fig. 12(b) is also in agreement with the voltage tuning in the first and third lobes of Fig. 11(c).

V. CONCLUSIONS

The intermediate regime $L \geq 1$, where the standard analytical methods (cavity-mode theory for $L \leq 1$ and soliton perturbation theory for $L \gg 1$) *a priori* do not apply, was investigated numerically and experimentally. A comparison between the experiments and the numerical calculations showed a very good qualitative agreement. Based on this comparison it was possible to identify the various soliton modes in the magnetic field lobes of ZFS1/FS2. The extension of single-cavity-mode theory to multimodes due to Enpuku *et al.*⁷ gave satisfactory predictions of the diffraction pattern for ZFS1 and FS2. Thus, with caution elements from both types of theories are usable, however, numerical simulation is necessary for a wider understanding of experimental observations.

ACKNOWLEDGMENTS

It is our pleasure to thank Alwyn C. Scott for many helpful discussions. The financial support of the Danish

Natural Science Research Council, the Thomas B. Thriges Fund, and the European Research Office of the United States Army (through Contract No. DAJA-37-82-C-0057) is gratefully acknowledged.

- ¹N. F. Pedersen, in *Advances in Superconductivity*, NATO Advanced Study Institute Series, B100, edited by B. Deaver and John Ruvalds (Plenum, New York, 1982), p. 149.
- ²S. N. Ern  and R. D. Parmentier, *J. Appl. Phys.* **51**, 5025, (1980).
- ³S. N. Ern , A. Ferrigno, and R. D. Parmentier, *Phys. Rev. B* **27**, 5440 (1983).
- ⁴B. Dueholm, O. A. Leving, J. Mygind, N. F. Pedersen, O. H. Soerensen, and M. Cirillo, *Phys. Rev. Lett.* **46**, 1299 (1981).
- ⁵E. Joergensen, V. P. Koshelets, R. Monaco, J. Mygind, M. R. Samuelsen, and M. Salerno, *Phys. Rev. Lett.* **49**, 1093 (1982).
- ⁶D. W. McLaughlin and A. C. Scott, *Phys. Rev. A* **18**, 1672 (1978).
- ⁷K. Enpuku, K. Yoshida, and F. Irie, *J. Appl. Phys.* **52**, 344 (1981).
- ⁸M. Cirillo, R. D. Parmentier, and B. Savo, *Physica (Utrecht)* **3D**, 565 (1981).
- ⁹P. S. Lomdahl, O. H. Soerensen, and P. L. Christiansen, *Phys. Rev. B* **25**, 5737 (1982).
- ¹⁰A. Matsuda and T. Kawakami, *Phys. Rev. Lett.* **51**, 694 (1983).
- ¹¹S. Sakai, H. Akoh, and H. Hayakawa, *Jpn. J. Appl. Phys.* **22**, L479 (1983).
- ¹²A. Barone, W. J. Johnson, and R. Vaglio, *J. Appl. Phys.* **46**, 3628 (1975).
- ¹³M. P. Soerensen, P. L. Christiansen, R. D. Parmentier, and O. Skovgaard, *Appl. Phys. Lett.* **42**, 739 (1983).
- ¹⁴IMSL, Inc. (Houston, Texas) International Mathematical and Statistical Library (Ed. 9) routine FFTRC, 1982 (unpublished).
- ¹⁵W. A. Schlup, *J. Phys. C* **7**, 736 (1974).
- ¹⁶I. O. Kulik, *Zh. Tekn. Fiz.* **37**, 157 (1967) [*Sov. Phys.—Tech. Phys.* **12**, 111 (1967)].
- ¹⁷IMSL, Inc. (Houston, Texas) International Mathematical and Statistical Library (Ed. 9) routine ZSCNT, 1982 (unpublished).
- ¹⁸S. N. Ern , A. Ferrigno, S. DiGenova, and R. D. Parmentier, *Lett. Nuovo Cimento* **34**, 121 (1982).
- ¹⁹O. A. Leving, N. F. Pedersen, and M. R. Samuelsen, *J. Appl. Phys.* **54**, 987 (1983).
- ²⁰G. Patern  and J. Nordman, *J. Appl. Phys.* **49**, 2456 (1978).
- ²¹Junctions fabricated both at the Technical University of Denmark and at the University of Salerno were measured, with similar results.
- ²²N. F. Pedersen and D. Welner, *Phys. Rev. B* **29**, 2551 (1984).
- ²³C. S. Owen and D. J. Scalapino, *Phys. Rev.* **164**, 538 (1967).

Simulation studies of radiation linewidth in circular Josephson-junction fluxon oscillators

F. If, P. L. Christiansen, R. D. Parmentier,* O. Skovgaard, and M. P. Soerensen

Laboratory of Applied Mathematical Physics, The Technical University of Denmark, DK-2800 Lyngby, Denmark

(Received 8 November 1984)

Detailed simulation studies of the dynamics of fluxons in long circular Josephson tunnel junctions under the influence of external microwave radiation and internal thermal noise are presented. The simulation algorithm uses a pseudospectral method well adapted to vector processors (CRAY-1-S), which gives a speed-up factor in computing time of typically 22 in comparison to conventional high-speed computers, and also provides results with a relative accuracy of less than 10^{-4} thereby making possible the study of the very narrow radiation linewidth of such oscillators. Comparison of calculated linewidths with experimental results shows good agreement.

MS code no. BY2341 1985 PACS numbers: 74.50. + r, 84.30.Ng, 05.40. + j

I. INTRODUCTION

Josephson-junction fluxon oscillators continue to attract research interest both theoretically, in studies of nonlinear wave dynamics, and experimentally, where the very narrow linewidth of the emitted microwave radiation promises potentially interesting applications.¹ This very narrow linewidth makes the numerical study of the detailed dynamics of such oscillators very CPU time consuming. In order to overcome these difficulties we have developed a pseudospectral algorithm for solving the perturbed sine-Gordon equation which describes the oscillator. This algorithm employs a Fourier transformation of the spatial variable together with a finite-difference approximation to the time variable. The extensive use of fast Fourier transforms in the algorithm has made the implementation natural on a CRAY-1-S vector processor. The Fourier treatment of the space variable requires spatial periodicity in the model. In physical terms this means that we are studying a circular junction oscillator of the type first proposed by McLaughlin and Scott.² This device, as well as providing a convenient mathematical model because of periodic boundary conditions, has in recent years begun to attract research interest in its own right.^{3,4}

The paper is structured as follows. In Sec. II we describe the mathematical model of the circular junction. Details of the numerical techniques employed are presented in Sec. III. In Sec. VI we study the behavior of the oscillator under the influence of a sinusoidal driving term in the bias current, which models external microwave irradiation. Section V contains calculations of the linewidth under the influence of Gaussian white noise, which models internal thermal noise in the junction. In Sec. VI we compare our results with existing experimental observations. In all of the sections we are focusing on a configuration with a single propagating fluxon, which corresponds to the first zero-field step in the current-voltage characteristic of the oscillator.

II. MATHEMATICAL MODEL

As a model for the Josephson tunnel junction of overlap geometry we use the perturbed sine-Gordon equation,⁵

$$\varphi_{xx} = \varphi_{tt} - \sin\varphi = \alpha\varphi_t + \gamma + \eta(x, t). \quad (2.1)$$

Here φ is the quantum phase difference between the two superconducting layers in the junction. Space and time are normalized to the Josephson penetration length $\lambda_J = (\Phi_0/2\pi j_0 L_p)^{1/2}$, and the inverse of the plasma frequency $\omega_p = (2\pi j_0/\Phi_0 C)^{1/2}$, respectively, where Φ_0 is the magnetic flux quantum given by $\Phi_0 = h/2e = 2.064 \times 10^{-15}$ Wb. L_p and C are the inductance and the capacitance per unit length of the junction. The first of the perturbation terms on the right-hand side of Eq. (2.1) represents the loss due to tunneling of normal electrons, in normalized units $\alpha = G/\omega_p C$, where G^{-1} is an effective normal resistance per unit length. The second term is the normalized bias current γ measured in units of j_0 the maximum Josephson current per unit length. In this paper we include a third term $\eta(x, t)$ representing either an externally applied sinusoidal driving term connected to the bias, or an internal thermal noise term connected to the loss. In this second case we assume a distributed Gaussian white noise with zero mean value.

The normalized length of the Josephson junction $l = L/\lambda_J$ is assumed to be large compared with unity and the normalized width $w = W/\lambda_J$ small compared with unity, allowing us to use a 1+1 dimensional model.⁶ Because the aim of this investigation is to isolate the influence of the term $\eta(x, t)$ on the solution to Eq. (2.1) we avoid phenomena connected with collision with junction boundaries by considering a long annular junction. Therefore, we demand spatial periodicity with period l in the two physical quantities, the voltage drop across the junction:

$$V = \frac{\Phi_0 \omega_p}{2\pi} \varphi_t, \quad (2.2)$$

and the current along the junction,

$$I = -j_0 \lambda_J \varphi_x, \quad (2.3)$$

i.e., boundary conditions

$$\varphi_t(0, t) = \varphi_t(l, t), \quad (2.4a)$$

$$\varphi_x(0, t) = \varphi_x(l, t). \quad (2.4b)$$

The fluxon traveling wave solution to the unperturbed version of Eq. (2.1) is given by⁷

$$\varphi = 2 \sin^{-1}[\text{cn}(\xi, k)], \quad (2.5)$$

with $\xi = (x - ut)/[k(1 - u^2)^{1/2}]$. Here u is the velocity of the wave and k is the modulus in the Jacobian elliptic function.⁸ Spatial periodicity requires $l/(1 - u^2)^{1/2} = 2nkK(k)$, where n is the winding number, i.e., the number of fluxons minus the number of antifluxons, and $K(k)$ is the complete elliptic integral of the first kind. In Ref. 9 it is shown by Hamiltonian perturbation theory² that the steady-state fluxon velocity dependence on the loss and bias parameters is

$$u = 1/(1 + (4\alpha'/\pi\gamma)^2)^{1/2}, \quad (2.6)$$

with $\alpha' = \alpha E(k)/k$, where $E(k)$ is the complete elliptic integral of the second kind. For $l \gtrsim 8$ (assuming $n = 1$) Eq. (2.5) reduces to the kink for the infinite line $\varphi = 4 \tan^{-1}(e^\xi)$ with $\xi = (x - ut)/(1 - u^2)^{1/2}$, and the velocity given by $u = 1/[1 + (4\alpha/\pi\gamma)^2]^{1/2}$. In the numerical simulations we have used $l = 8, 12.8, 20$, and $n = 1$.

III. NUMERICAL TECHNIQUES

The very narrow linewidth of the radiation emitted from a Josephson-junction oscillator (less than 1 kHz at 10 GHz)¹⁰ suggests that a relative numerical accuracy of at least 10^{-7} is essential. We solve Eq. (2.1) numerically by using a pseudospectral method.¹¹ This method, a Fourier transform treatment in space together with a leap-frog scheme in time, has the advantage of simplicity and high-order accuracy in the approximations to the space derivatives. Expansion of the fluxon wave into truncated series of sines and cosines demands periodicity not only in φ_x and φ_t but also in φ itself. Observing that the fluxon is a localized kink connecting two ground states separated by 2π we introduce a new periodic function $\varphi - 2\pi x/l$ whose Fourier representation we denote $\Phi^p(t)$ with the superscript $p = 0, \pm 1, \dots, \pm p_{\max}$.

Transforming Eq. (2.1) into the following set of ordinary nonlinear coupled differential equations:

$$-k_p^2 \Phi^p(t) - \Phi_n^p(t) - F^p[\sin \varphi] = \alpha \Phi_t^p(t) + l\gamma \delta_{p,0} + N^p(t), \quad (3.1a)$$

$$k_p = 2\pi p/l, \quad p = 0, \pm 1, \dots, \pm p_{\max} \quad (3.1b)$$

in which F^p and N^p are the Fourier components of $\sin \varphi$ and η , respectively, and $\delta_{p,0}$ denotes the Kronecker symbol, and using second-order central differences to approximate the time derivatives we get an explicit scheme for the time evolution of the Fourier components

$$\Phi_j^0 = [2\Phi_j^0 - (1 - \alpha\Delta t/2)\Phi_{j-1}^0 - \Delta t^2(S_j^0 + l\gamma + N_j^0)]/(1 + \alpha\Delta t/2), \quad (3.2a)$$

$$\Phi_j^p = [(2 - \Delta t^2 k_p^2)\Phi_j^p - (1 - \alpha\Delta t/2)\Phi_{j-1}^p - \Delta t^2(S_j^p + N_j^p)]/(1 + \alpha\Delta t/2), \quad |p| > 0, \quad (3.2b)$$

where S_j^p equals $F^p[\sin \varphi]$ at time $j\Delta t$, calculated each time step by transforming Φ_j^p back to x space, calculat-

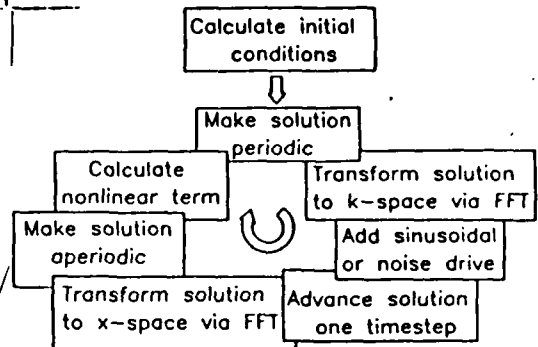


FIG. 1. Schematic diagram of numerical simulation procedure.

ing $\sin \varphi$ and then transforming again to k space as indicated schematically in Fig. 1.

Figure 2 shows the computed φ_x as a function of time at an arbitrary point on the junction. This signal consists of an almost-periodic sequence of pulses. In fact, it is the deviation from perfect periodicity that gives a nonzero linewidth of the radiation. Since the deviation is small it is necessary to devise a very accurate method for determining the revolution periods T_n for the circulating fluxon. We do this by calculating T_n as the time for the mean value of the phase over x to change by 2π . The fundamental frequency of the signal then becomes $f_0 = 1/\langle T_n \rangle$, where brackets denote an average value. We take the power spectrum of the signal near f_0 to be the distribution of the computer values of $1/T_n$.

Figure 3 shows the calculated T_n 's in a computer experiment with the driving term $\eta = 0$ in Eq. (2.1). As can be seen from Fig. 3, the relative accuracy $\Delta T/\langle T_n \rangle \lesssim 10^{-8}$. In fact, examination of the numerical output shows that it is approximately 7×10^{-9} . The long transient arises from the fact that the initial conditions given by

$$\varphi(x, 0) = f(x, 0) - \sin^{-1}(\gamma), \quad (3.3a)$$

$$\varphi(x, -\Delta t) = f(x, -\Delta t) - \sin^{-1}(\gamma), \quad (3.3b)$$

where $f(x, t)$ is the fluxon traveling wave solution to the unperturbed sine-Gordon equation as given by Eq. (2.5)

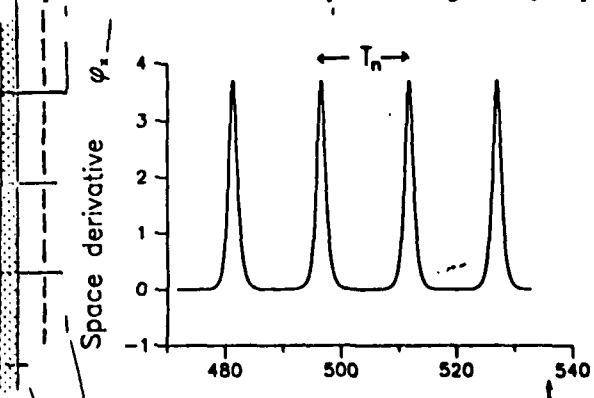


FIG. 2. Time dependence of the space derivative of the fluxon waveform, showing the n th period of revolution T_n for $\alpha = 0.01$, $\gamma = 0.02$, $\eta = 0$, and $l = 12.8$.

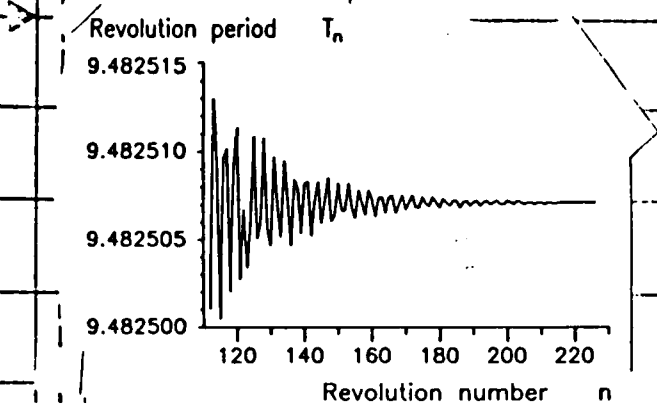


FIG. 3. Revolution period T_n as a function of revolution number n for $\alpha=0.01$, $\gamma=0.02$, $\eta=0$, and $l=8$ showing high level of computational accuracy achieved.

and $\sin^{-1}(\gamma)$ is the ground state, are not exactly equal to the final propagating configuration.

We note at this point that the accuracy of the results was checked by doubling p_{\max} in Eq. (3.1b), in order to ensure that no spurious Fourier modes due to the discretization in x space are produced, and halving Δt in Eqs. (3.2). The values used for p_{\max} ranged from 64 to 256 and those for Δt from 0.075 to 0.0025, depending on the parameters l and γ .

The computer program was implemented on an IBM 3033 in double precision (approximately 16 significant digits) and on a CRAY-1 vector processor in single precision (approximately 15 significant digits) using optimizing FORTRAN compilers. In the former case we have used the IMSL-routine FFT2C for fast Fourier transform.¹² In the latter case, by making full use of vectorization of the computer code and the CRAY routines for Fourier transform and vector copying CFFT2 (Ref. 13) and CCOPY (Ref. 14) we gained a speed-up factor in computing time of 22. Each long simulation requires typically 5×10^5 time steps on a 512-point spatial lattice and uses approximately 10 min of CPU time on the CRAY-1-S as opposed to approximately 4 h on a scalar machine.

Finally, we have compared the steady-state fluxon velocity, given by $u = l / \langle T_n \rangle$, with the predicted value

from Hamiltonian perturbation theory, Eq. (2.6). The result is seen in Fig. 4. The deviation for large bias values is expected because the perturbation theory is only valid for small γ values.

IV. SINUSOIDAL DRIVING TERM

In this section we investigate the behavior of the fluxon velocity when the driving term is given by

$$\eta(x, t) = \eta(t) = \eta_0 \sin(\Omega t), \quad (4.1)$$

as a function of the driving frequency Ω . This might be considered as a model of microwave irradiation of the junction. Using the definition of the normalized momentum

$$p(t) = -\frac{1}{l} \int_0^l \varphi_x \varphi_t dx, \quad (4.2)$$

and separating the phase into a kink part and a background part¹⁵ $\varphi(x, t) = \varphi^k(x, t) + \varphi^\infty(t)$, and assuming that the length of the junction is large, allowing expressions for the infinite junction to be used, we get the following equation for the momentum p^k of the kink,

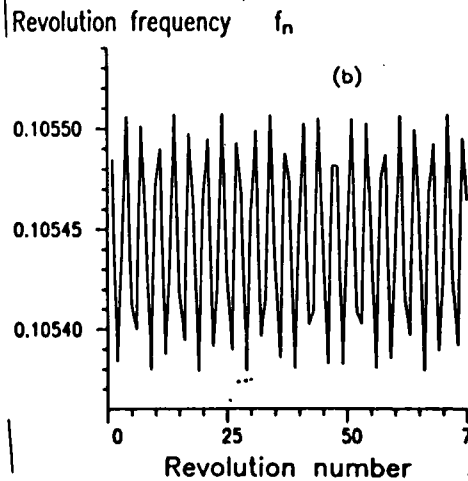
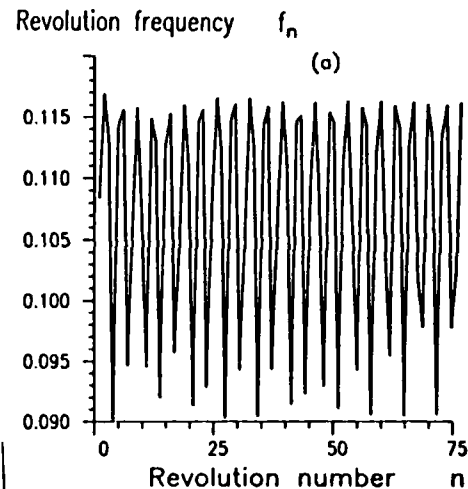


FIG. 5. Revolution frequency f_n as a function of revolution number n for sinusoidal drive, $\eta(t) = \eta_0 \sin(\Omega t)$, with $\alpha=0.01$, $\gamma=0.02$, $\Omega=0.86$, $\eta_0=0.01$, and $l=8$. (a) Numerical simulation. (b) Kink model.

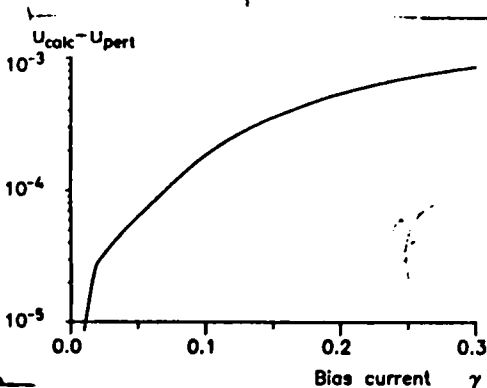


FIG. 4. Difference between average propagation velocity as computed numerically u_{calc} and calculated from perturbation theory u_{pert} from Eq. (2.6) as a function of the bias for $\alpha=0.01$, $\eta=0$, and $l=8$.

$$\frac{dp^k}{dt} + \alpha p^k = \frac{\pi}{4} \left[\gamma + \eta_0 \sin(\Omega t) + \alpha \frac{d\varphi^\infty}{dt} + \frac{d^2\varphi^\infty}{dt^2} \right] \quad (4.3)$$

Thus, the background motion becomes an effective driving term for the kink part. From Eq. (2.1) we derive the linearized equation for $\hat{\varphi}^\infty = \varphi^\infty + \sin^{-1}(\gamma)$, assuming that $\hat{\varphi}^\infty \ll 1$,

$$\frac{d^2\hat{\varphi}^\infty}{dt^2} + \alpha \frac{d\hat{\varphi}^\infty}{dt} + (1-\gamma^2)^{1/2} \hat{\varphi}^\infty = -\eta_0 \sin(\Omega t). \quad (4.4)$$

Combining Eqs. (4.3) and (4.4) we obtain for the kink momentum

$$p^k(t) = \frac{\pi}{4} \left[\frac{\gamma}{\alpha} + \frac{\eta_0}{(\alpha^2 + \Omega^2)^{1/2}} \sin(\Omega t - \theta_1) - \frac{\eta_0 \Omega}{\{[(1-\gamma^2) - \Omega^2]^2 + \alpha^2 \Omega^2\}^{1/2}} \cos(\Omega t - \theta_2) \right], \quad (4.5a)$$

$$\theta_1 = \tan^{-1}(\Omega/\alpha)$$

and

$$\theta_2 = \tan^{-1}\{\alpha\Omega/[(1-\gamma^2)^{1/2} - \Omega^2]\}. \quad (4.5b)$$

The instantaneous kink velocity is then calculated from $p^k = u/(1-u^2)^{1/2}$. In order to compare this approximate theoretical description with the numerical result we calculate the n th period T_n according to the formula

$$\int_{t_{n-1}}^{t_{n-1}+T_n} u dt = l, \quad (4.6)$$

with

$$u = p^k/[1+(p^k)^2]^{1/2}.$$

Figures 5-7 show a comparison of the results from this linearized model and from numerical simulations of Eq. (2.1) with $\Omega = 0.86, 0.89$, and 1.10 , respectively. In all cases it is seen that the kink model is able to reproduce the fluctuations in the revolution frequency $f_n = 1/T_n$ in great detail.

As a measure of the amplitude of the frequency fluctuation

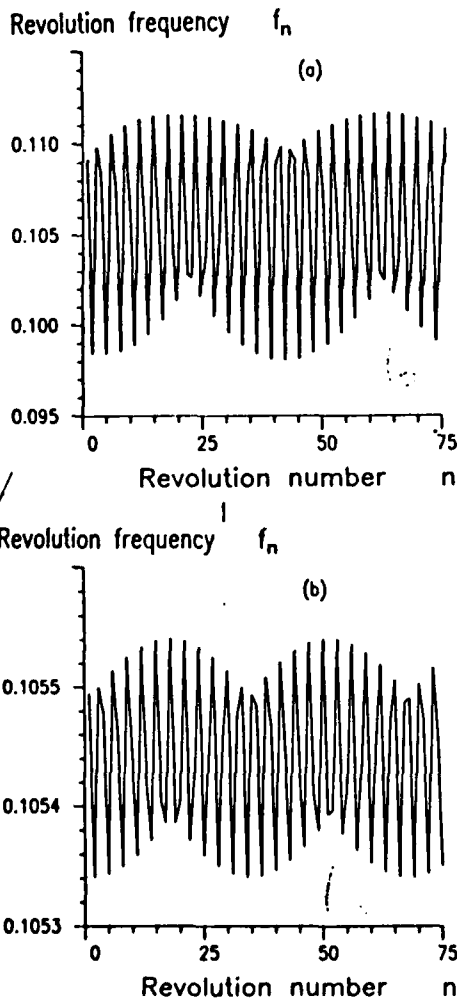


FIG. 6. Revolution frequency f_n as a function of revolution number n for sinusoidal drive, $\eta(t) = \eta_0 \sin(\Omega t)$, with $\alpha = 0.01$, $\gamma = 0.02$, $\Omega = 0.89$, $\eta_0 = 0.01$, and $l = 8$. (a) Numerical simulation. (b) Kink model.

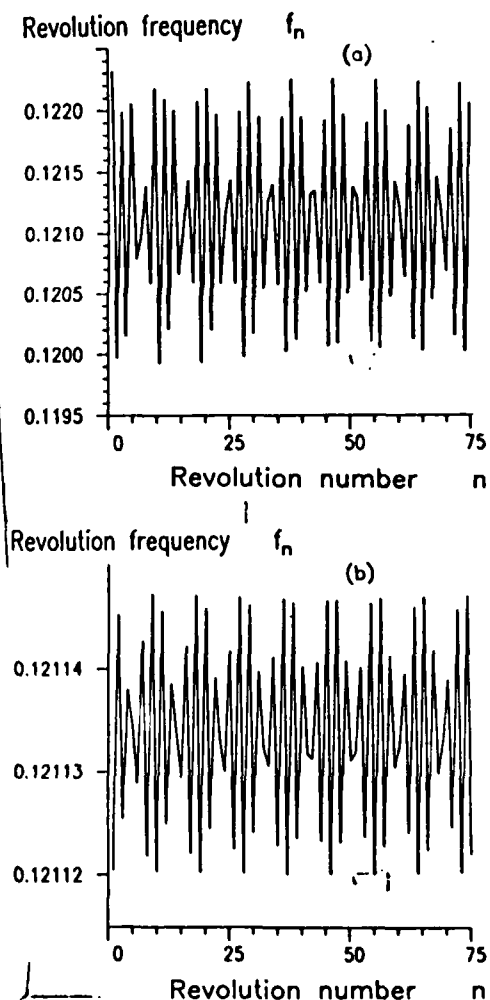


FIG. 7. Revolution frequency f_n as a function of revolution number n for sinusoidal drive, $\eta(t) = \eta_0 \sin(\Omega t)$, with $\alpha = 0.01$, $\gamma = 0.02$, $\Omega = 1.10$, $\eta_0 = 0.01$, and $l = 8$. (a) Numerical simulation. (b) Kink model.

Standard deviation σ_f

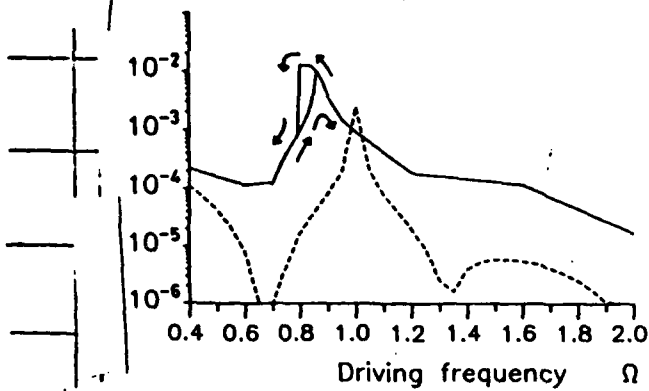


FIG. 8. Standard deviation of revolution frequency σ_f as a function of driving frequency Ω . Solid curve, numerical simulation; dashed curve, kink model; parameters, $\alpha=0.01$, $\gamma=0.02$, $\eta_0=0.01$, and $l=8$.

uation, which is essentially the linewidth of the oscillator, we have calculated the standard deviation of the revolution frequency $\sigma_f = \{ \langle (f_n - \langle f_n \rangle)^2 \rangle \}^{1/2}$ for values of the cyclic driving frequency Ω between 0.4 and 2.0.

The full curve in Fig. 8 shows the results from the numerical simulation and the dashed curve those from the kink model. The kink model predicts a resonance just below the plasma frequency $\Omega=1$, whereas the numerical simulation yields this peak at a somewhat lower frequency. Moreover, the numerical results exhibit a hysteresis not seen in those of the kink model and a difference in scale. The discrepancy in resonance frequency and hysteresis behavior is attributable to the fact that we have used a linearized kink model. Presumably, the use of a higher-order expansion in Eq. (4.4) would yield a behavior analogous to that of a soft nonlinear spring¹⁶ thus reducing these discrepancies. It is not clear, however, to what extent the difference in scale would be resolved by such a refinement.

V. GAUSSIAN WHITE NOISE

The term $\eta(x,t)$ in Eq. (2.1) is here considered to be Gaussian white noise with zero mean $\langle \eta(x,t) \rangle = 0$ and autocorrelation function

$$R_\eta(\xi, \tau) = \langle \eta(x,t) \eta(x+\xi, t+\tau) \rangle = \sigma_\eta^2 \delta(\xi) \delta(\tau). \quad (5.1)$$

The variance of the noise σ_η^2 is connected with the loss α and the absolute temperature T through¹⁷

$$\sigma_\eta^2 = 4\pi akT / \Phi_{0j_0} \lambda_j, \quad (5.2)$$

where k is the Boltzmann constant.

In the vectorized algorithm we find it convenient to introduce the noise term in p - t space, $N^p(t)$, as

$$N^p(t) = F^{-1} \{ \sigma_\eta \exp(i(\theta_p + \theta_\omega)) \}, \quad (5.3)$$

where F^{-1} denotes the Fourier transform from ω to t space, and θ_p and θ_ω are stochastic variables uniformly distributed between 0 and 2π , with an upper limit in p and ω of $p_{max} = 1/2\Delta x$ and $\omega_{max} = \pi/\Delta t$, Δx and Δt being the resolution in space and time, respectively. Standard

Hamiltonian perturbation theory for the fluctuations Δu in the fluxon velocity leads to the power spectrum for Δu ,¹⁰

$$S_{\Delta u}(\omega) = \frac{1}{4} \sigma_\eta^2 (1-u_0^2)^{5/2} \frac{1}{\omega^2 + \alpha^2}, \quad (5.4)$$

with the average velocity u_0 given by Eq. (2.6). By a Fourier transform of Eq. (5.4) we obtain the autocorrelation function for Δu as an exponential

$$R_{\Delta u}(\tau) = \frac{\sigma_\eta^2 (1-u_0^2)^{5/2}}{16\alpha} e^{-\alpha|\tau|}. \quad (5.5)$$

Thus $\Delta u(t)$ is a normal process with zero mean and standard deviation¹⁸

$$\sigma_{\Delta u} = \frac{\sigma_\eta (1-u_0^2)^{5/4}}{4\alpha^{1/2}}. \quad (5.6)$$

Defining the period of a fluxon revolution according to Eq. (4.6) we calculate the average frequency fluctuation as the average of the instantaneous frequency fluctuation $\Delta u/l$ over one average period of revolution

$$\Delta f = \frac{1}{\langle T \rangle} \int_t^{t+\langle T \rangle} \Delta u / l dt. \quad (5.7)$$

From Eq. (5.7) it follows that Δf has a normal distribution with zero mean and the standard deviation,¹⁹

$$\sigma_{\Delta f} = \frac{1}{l} \sigma_{\Delta u} \left[\frac{2u_0}{\alpha l} \left| 1 - u_0 \frac{1 - \exp(-\alpha l / u_0)}{\alpha l} \right| \right]^{1/2}. \quad (5.8)$$

A numerical simulation with $\sigma_\eta = 8.8 \times 10^{-4}$ is seen in Fig. 9 showing a typical frequency distribution of Δf about the fundamental frequency $f_0 = u_0/l$. The connection between the standard deviation and the half-power linewidth is

$$\Delta f_{1/2} = \sqrt{8 \ln 2} \sigma_{\Delta f} \quad (5.9)$$

when Δf is normal distributed.

Figures 10 and 11 show a comparison of the standard deviation predicted by this model Eq. (5.8) and the results

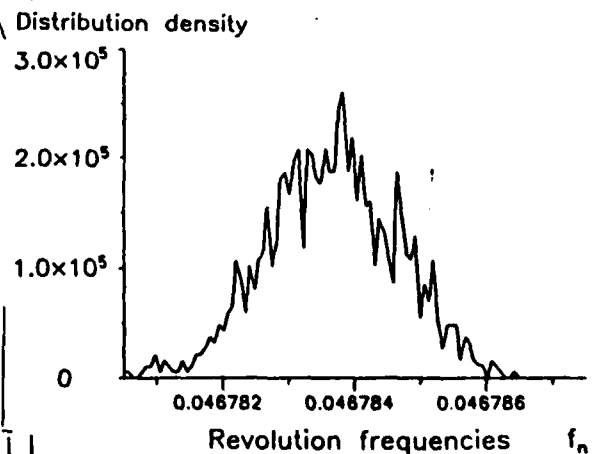


FIG. 9. Distribution of revolution frequency f_n . Numerical simulation with Gaussian noise drive: $\alpha=0.01$, $\gamma=0.034$, $\sigma_\eta=8.8 \times 10^{-4}$, and $l=20$.

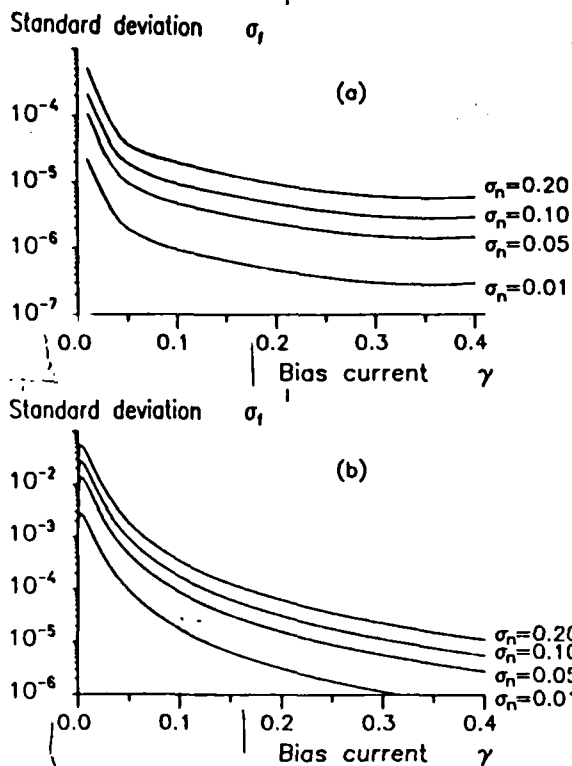


FIG. 10. Standard deviation of revolution frequency σ_f for white Gaussian noise drive as a function of bias current γ , for $\alpha=0.01$, $l=8$, and $\sigma_n=0.01, 0.05, 0.10$, and 0.20 . (a) Numerical simulation. (b) Hamiltonian perturbation theory.

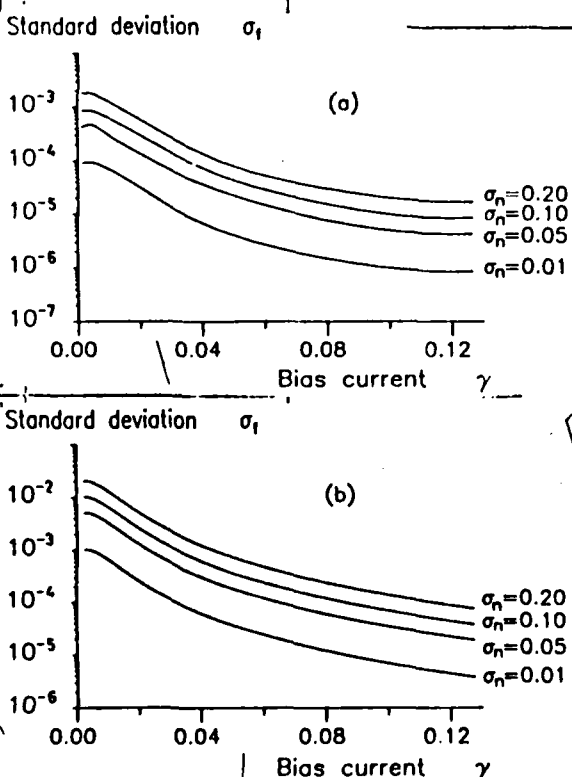


FIG. 11. Standard deviation of the revolution frequency σ_f for white Gaussian noise drive as a function of bias current γ , for $\alpha=0.01$, $l=20$, and $\sigma_n=0.01, 0.05, 0.10$, and 0.20 . (a) Numerical simulation. (b) Hamiltonian perturbation theory.

from the numerical simulations for the lengths $l=8$ and $l=20$, respectively. As can be seen, the model is able to predict the right qualitative dependence on the length, the noise amplitude, and the bias, but the model predicts an overall standard deviation that is about a factor of 10 too large. The reason for this discrepancy is at present not known.

In closing, we note that for γ values near 0.3 it was found necessary to augment the time resolution (by reducing Δt) to avoid spurious peaks in Fig. 10(a). The existence of such spurious peaks might be an indicator of the onset of chaotic behavior at nearby points in parameter space. In fact, parameter values $\gamma=0.3$ with $\alpha=0.01$ lead to chaotic creation of fluxon-antifluxon pairs in the study reported by Eilbeck.²⁰

VI. COMPARISON WITH EXPERIMENTS

The rapidly decreasing linewidth with increasing bias shown in Figs. 10 and 11 is in qualitative agreement with the experimental observations of Fig. 1 in Ref. 10.

To compare quantitatively the calculated results with these experiments we use in Eq. (5.2) data reported by Scott *et al.*⁵ For the junction No. N25L, assuming a temperature of 4 K, Eq. (5.2) gives $\sigma_n=0.0052$. Noting from Fig. 9(a) that σ_f scales linearly with σ_n , we calculate from Eq. (5.9) a normalized half-power linewidth $\Delta f_{1/2}=5.5 \times 10^{-7}$ at $\gamma=0.2$. Taking as the normalized resonance frequency $f_0=u_0/l \approx 0.125$ we calculate a relative linewidth $\Delta f_{1/2}/f_0=4.4 \times 10^{-6}$. The physical resonance frequency for junction No. N25L was 2.3 GHz.⁵ This yields a physical linewidth of 10 kHz. Comparing with the experimental results shown in Fig. 1 of Ref. 10 and noting that $\gamma=0.2$ corresponds to a bias point near the bottom of the zero-field step, we find excellent agreement. The same calculations for junction No. N53C,⁵ again for $T=4$ K and $\gamma=0.2$, yield $\Delta f_{1/2}/f_0=2.3 \times 10^{-6}$. The physical resonance frequency for junction No. N53C was 8.3 GHz, which leads to a physical linewidth of 18 kHz, once again in excellent agreement with experimental results.

VII. CONCLUSIONS

Computational studies of the linewidth of the radiation emitted by Josephson junctions require extremely high resolution. For this reason we developed a pseudospectral method for solving the nonlinear dynamical equation describing a circular Josephson junction oscillator. Because the algorithm makes heavy use of fast Fourier transforms it was implemented on a CRAY-1 vector processor. Driving terms corresponding to physically realistic situations, i.e., sinusoidal microwave irradiation and internal thermal noise, were considered. In the second case the computational results were compared with experimental results reported in the literature, and excellent qualitative and quantitative agreement was found. In addition, in both cases we have compared the computational results with approximate analytic results based on perturbation theory. Here the agreement was qualitatively good, but quantitative discrepancies were found, indicating a need for further development of perturbation theory.

ACKNOWLEDGMENTS

It is our pleasure to thank Alwyn C. Scott for proposing this work and for his continued interest in it. We acknowledge Niels F. Pedersen for helpful discussions on modeling of thermal noise in Josephson junctions and Mogens Samuelsen for pointing out the significance of

Ref. 15 in the context of the present work. The financial support of the Danish Council for Scientific and Industrial Research and by the European Research Office of the United States Army (through Contract No. DAJA-37-82-C-0057) is gratefully acknowledged. R.D.P. thanks the Technical University of Denmark for providing support for part of the period during which this work was performed.

*Permanent address: Dipartimento di Fisica, Università di Salerno, 84100 Salerno, Italy.

¹N. F. Pedersen, in *Advances in Superconductivity, NATO Advanced Study Institute Series, B100*, edited by B. Deaver and J. Ruvalds (Plenum, New York, 1982), p. 149.

²D. W. McLaughlin and A. C. Scott, *Phys. Rev. A* **18**, 1652 (1978).

³A. Davidson and N. F. Pedersen, *Appl. Phys. Lett.* **44**, 465 (1984).

⁴B. Dueholm, A. Davidson, C. C. Tsuei, M. J. Brady, K. H. Brown, A. C. Callegari, M. M. Chen, J. H. Greiner, H. C. Jones, K. K. Kim, A. W. Kleinsasser, H. A. Notarys, G. Proto, R. H. Wang, and T. Yogi, *Proceedings of the 17th International Conference on Low-Temperature Physics, Conference LT 17*, edited by U. Ekern, A. Schmid, H. Weber, and H. Wühl (North-Holland, Amsterdam, 1984), Part I, p. 691.

⁵A. C. Scott, F. Y. F. Chu, and S. A. Reible, *J. Appl. Phys.* **47**, 3272 (1976).

⁶J. C. Eilbeck, P. S. Lomdahl, O. H. Olsen, and M. R. Samuelsen, *J. Appl. Phys.* (to be published).

⁷R. D. Parmentier, in *Solitons in Action*, edited by K. Lonngren and A. C. Scott (Academic, New York, 1978), p. 173.

⁸P. F. Byrd and M. D. Friedman, *Handbook of Elliptic Integrals for Engineers and Physicists* (Springer, Berlin, 1954).

⁹F. If, M. P. Soerensen, and P. L. Christiansen, *Phys. Lett.* **100A**, 68 (1984).

¹⁰E. Joergensen, V. P. Koshelets, R. Monaco, J. Mygind, and M. R. Samuelsen, *Phys. Rev. Lett.* **49**, 1093 (1982).

¹¹D. Gottlieb and S. A. Orszag, *Numerical Analysis of Spectral Methods* (SIAM, Philadelphia, 1977).

¹²IMSL, Inc. (Houston, Texas) International Mathematical and Statistical Library, 9th Ed. routine FFT2C, 1982 (unpublished).

¹³*CRAY-1 Computer Systems, Library Reference Manual SR0014* (Cray Research, Mendota Heights, 1982), pp. 4-49; see also CRAY Computer Systems Technical Note, Complex Fast Fourier Transform Binary Radix Subroutine (CFFT2) SN0203 (Cray Research, Mendota Heights, 1983).

¹⁴*CRAY-1 Computer Systems, Library Reference Manual SR0014* (Cray Research, Mendota Heights, 1982), pp. 4-9.

¹⁵O. A. Levring, M. R. Samuelsen, and O. H. Olsen, *Physica* **11D**, 349 (1984).

¹⁶A. H. Nayfeh and D. T. Mook, *Nonlinear Oscillations* (Wiley, New York, 1979), p. 161.

¹⁷M. Büttiker and R. Landauer, *Phys. Rev. A* **18**, 1652 (1978).

¹⁸A. Papoulis, *Probability, Random Variables, and Stochastic Processes* (McGraw-Hill, New York, 1965), p. 519.

¹⁹A. Papoulis, *Probability, Random Variables, and Stochastic Processes* (Ref. 18), p. 324.

²⁰J. C. Eilbeck, P. S. Lomdahl, and A. C. Newell, *Phys. Lett. A* **87**, 1 (1981).

ON LOW-DIMENSIONAL CHAOS IN RF SQUIDS

M.P. SOERENSEN, M. BARTUCCELLI, P.L. CHRISTIANSEN

*Laboratory of Applied Mathematical Physics, The Technical University of Denmark,
DK-2800 Lyngby, Denmark*

and

A.R. BISHOP

*Theoretical Division and Center for Nonlinear Studies, Los Alamos National Laboratory,
Los Alamos, NM 87545, USA*

Received 14 February 1985; accepted for publication 15 April 1985

Superconducting quantum interference devices (SQUIDS) respond chaotically to external oscillating fluxes. The small deviations from one-dimensional return maps are investigated. Within a narrow region of parameter space a sequence of period doublings, windows with odd periods and chaotic behaviour, intermittency and bifurcation between coexisting attractors of low dimension are found.

A periodically driven rf superconducting quantum interference device (SQUID) consisting of a ring with a single Josephson junction has been investigated recently both by means of analogue circuits [1] and computationally [2,3]. Like many other physical systems the device exhibits deterministic chaos (intrinsic noise). In this letter we investigate in detail a particular portion of parameter space which exhibits extremely rich details of the dynamics. Furthermore, we demonstrate that the choice of attractor (in cases with more than one attractor) may depend on the initial conditions, i.e. there can be coexisting attractors.

The order parameter for the Josephson junction, ϕ , satisfies the differential equation [2]

$$\phi'' + \epsilon\phi' + \sin\phi = \alpha(\gamma \sin \omega_D t - \phi), \quad (1)$$

where primes signify differentiation with respect to the dimensionless time t given by $t = T(C\phi_0/2\pi J_c)^{1/2}$. Here T is laboratory time, $\phi_0 = h/2|e|$ is the flux quantum, C and J_c are the capacitance and the maximal critical current, respectively. The loss parameter, ϵ , is given by $\epsilon^2 = \phi_0/2\pi C J_c R^2$ where R is the resistance of the weak link. The external flux is assumed to be sinusoidal with frequency ω_D and amplitude γ . In the additional term, $\alpha\phi$, $\alpha = \phi_0/2\pi J_c L$, where L is

the inductance of the ring. Due to the presence of this term, which corresponds to a confining quadratic potential, less chaos might be expected in this system than in the single Josephson junction without the $\alpha\phi$ term [2]. We have shown that eq. (1) does *not* possess the Painlevé property [4] in accordance with the fact that chaos in the system does occur for certain initial conditions. The proof is obtained by converting eq. (1) into four non-linear coupled autonomous first-order differential equations through differentiations and trigonometric substitutions [5]. The resulting system can be shown to possess other movable singularities than poles. Therefore the system, and thus eq. (1), is not of Painlevé type.

Eq. (1) was integrated numerically by means of IMSL routine [6] DVERK-1. Our results are shown as the return maps in figs. 1 and 2. As in ref. [2] we plot $X(n+1)$ versus $X(n) = \phi'(t_n + \Delta)$ with t_n given as the n th zero crossing of ϕ' and the constant Δ arbitrarily chosen as $\Delta = 0.134$. The numerical simulations showed that the transients had died out before $n = 300$. Iterations from $n = 300$ to $n = 600$ are included. In view of the fixed rf driving our general return map construction could be substituted by, e.g., a simple strobing at the driving period. Differing constructions

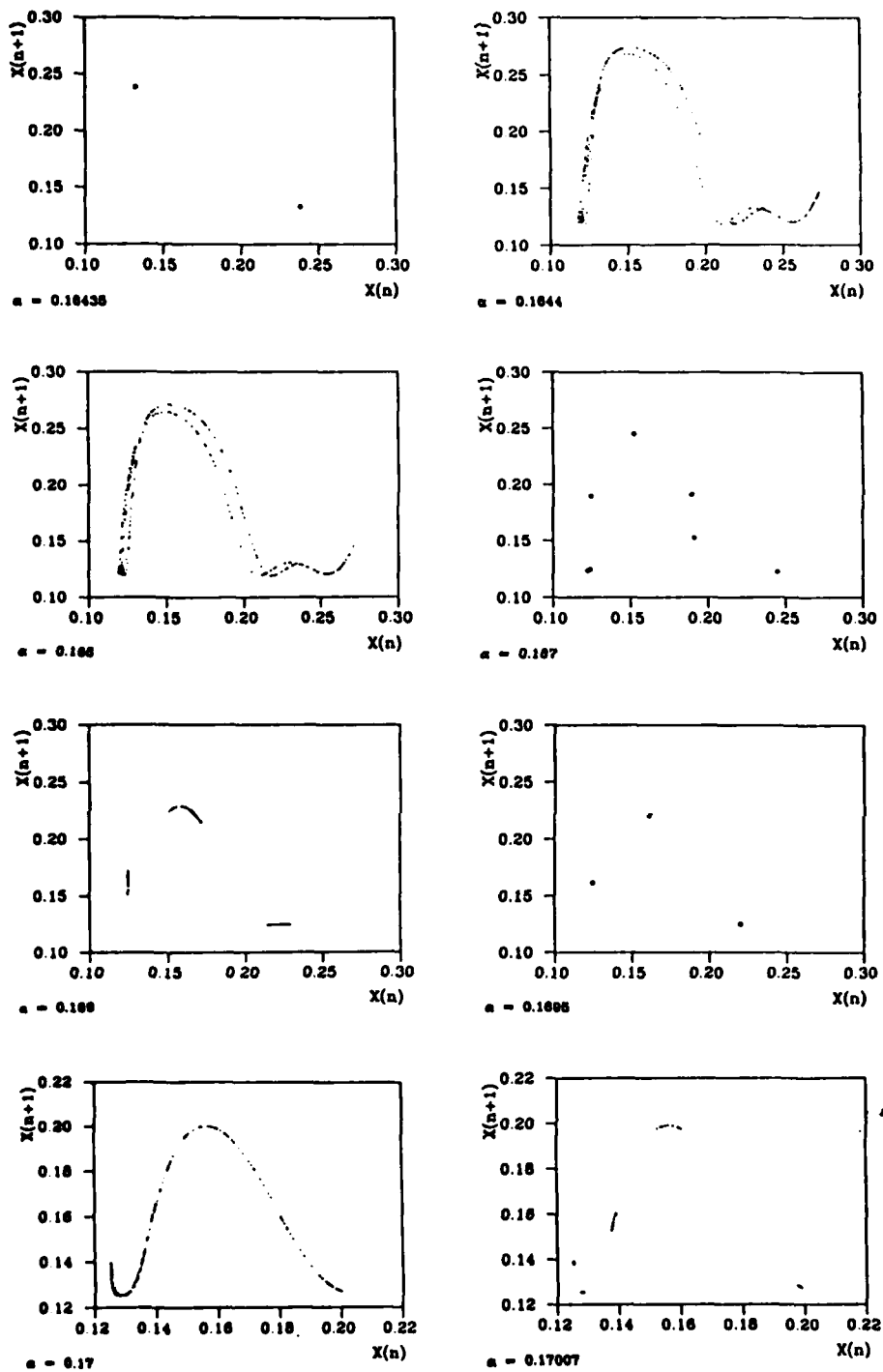


Fig. 1. Continued on next page.

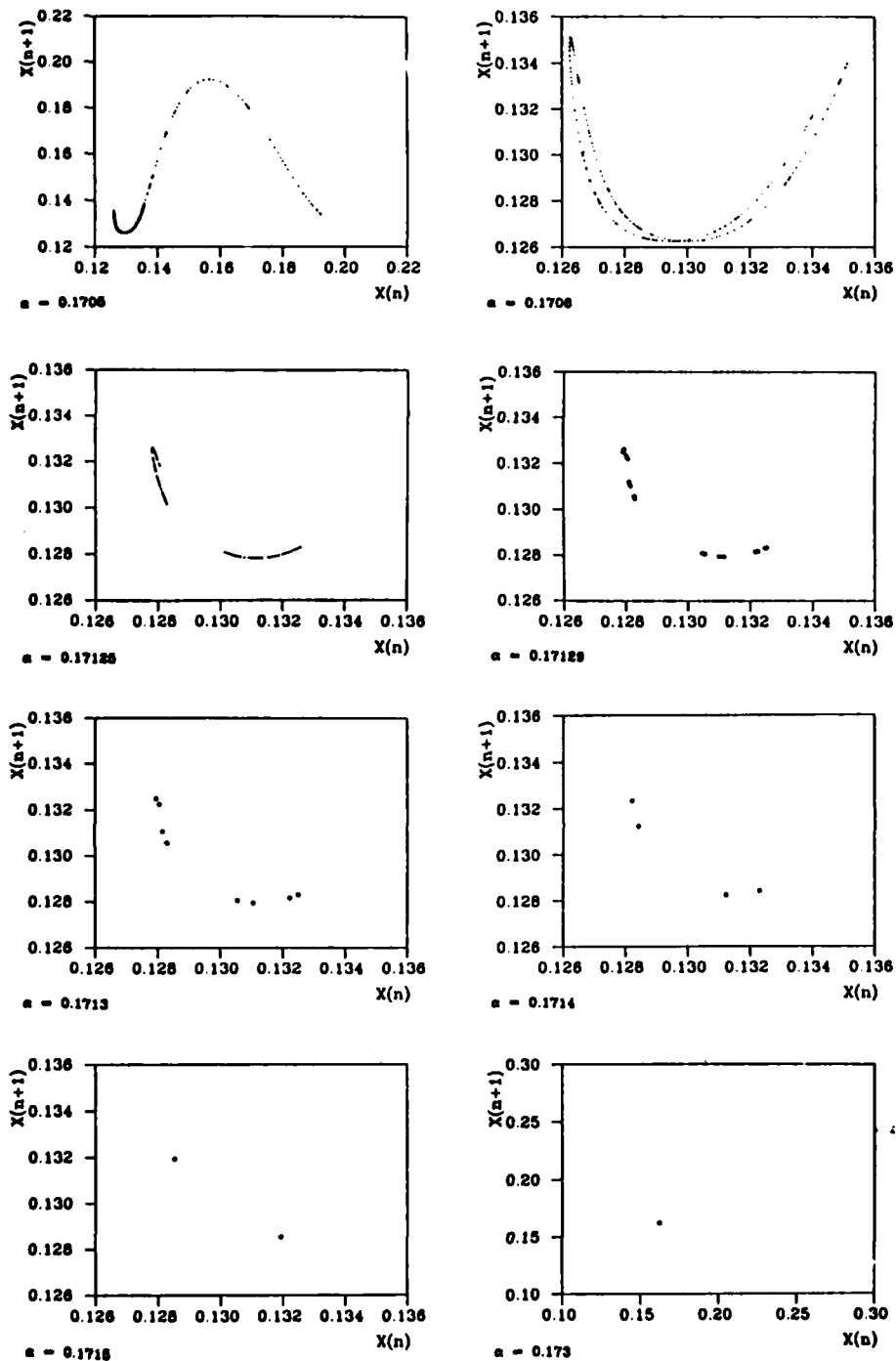


Fig. 1. Return maps obtained as ordered pairs $X(n), X(n+1)$ for $n = 300-600$. Parameters in eq. (1) are $\epsilon = 0.5, \gamma = 10, \omega_D = 0.5$, and $\alpha = 0.16435-0.173$. Initial conditions for $\alpha = 0.16435$ $\phi(0) = \phi'(0) = 0$. In subsequent maps the values of ϕ and ϕ' of the preceding run are used as initial conditions.

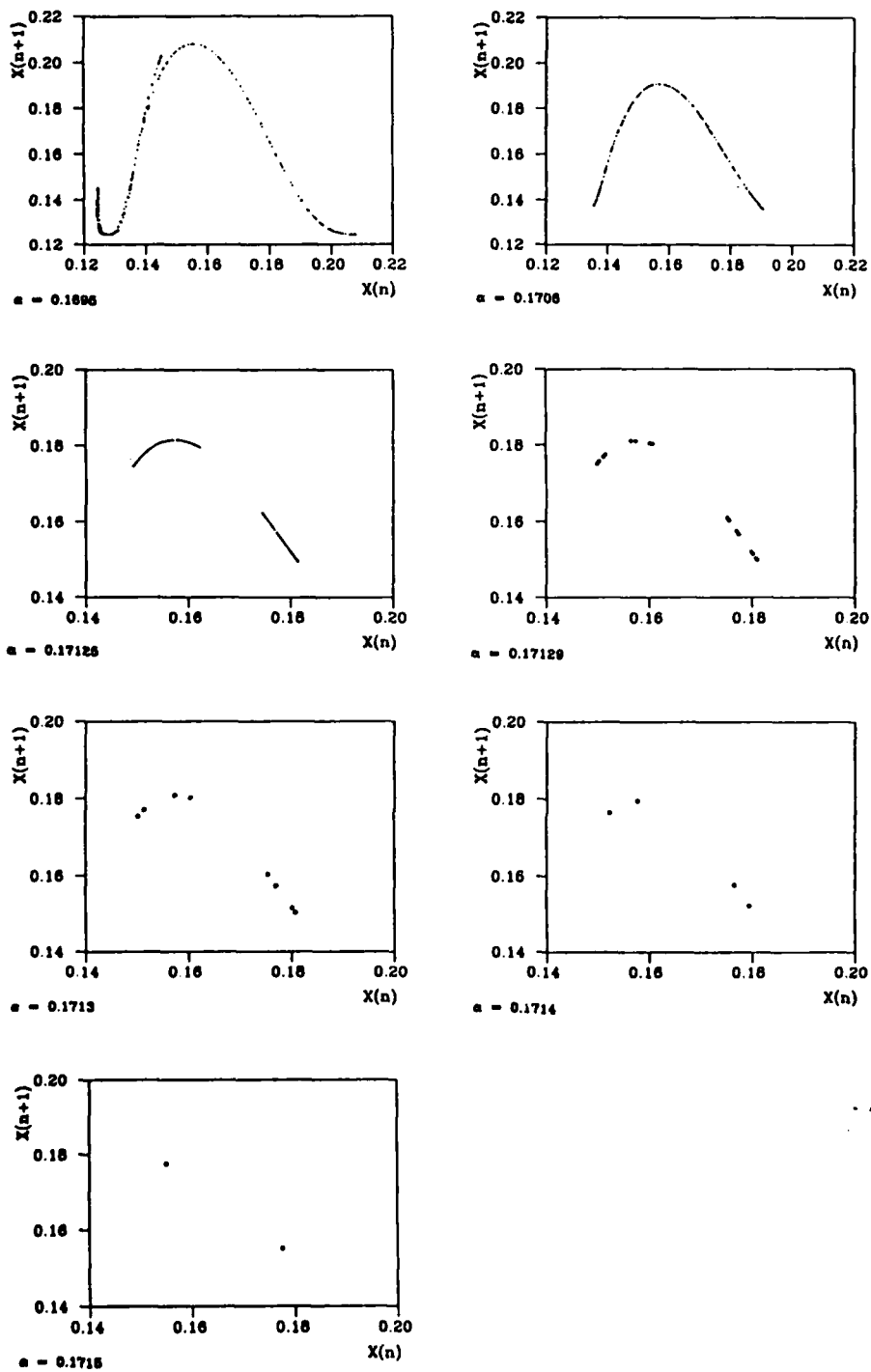


Fig. 2. Return maps obtained as ordered pairs $X(n), X(n + 1)$ for $n = 300-600$. Parameters in eq. (1) are $\epsilon = 0.5, \gamma = 10, \omega_D = 0.5$, and $\alpha = 0.1695-0.1715$. Initial conditions $\phi(0) = \phi'(0) = 0$ throughout.

should not affect the topological information carried by the map. The computational procedure proposed by Hénon [7] was used. Of the four parameters in eq. (1) ϵ , γ and ω_D were kept constant throughout at the values chosen in fig. 3 of ref. [2]: $\epsilon = 0.5$, $\gamma = 10$, and $\omega_D = 0.5$.

In fig. 1 the parameter α was varied from $\alpha = 0.16435$ to $\alpha = 0.173$. In the first run, $\alpha = 0.16435$, initial conditions $\phi(0) = \phi'(0) = 0$ were used and a period-2 solution was found (as indicated in fig. 2 of ref. [2]). In the following run, $\alpha = 0.1644$, the final values of ϕ and ϕ' from the previous run were used as initial conditions. This procedure was used throughout in a series of computer experiments with increasing values of the parameter α . However, for each value of α , eq. (1) was also solved for initial conditions $\phi(0) = \phi'(0) = 0$.

When the resulting return maps (for $n = 300-600$) differed the map is included in fig. 2. For $\alpha = 0.1644$ a return map indicating low-dimensional chaotic behaviour was found (for both sets of initial conditions). As the parameter α was raised to $\alpha = 0.165$ only small changes in the return map occurred. However, at $\alpha = 0.167$ we observed a shift from chaotic behaviour into a period-7 solution. At $\alpha = 0.169$ the return map again exhibits chaotic behaviour, this time as a period-3 window. At $\alpha = 0.1695$ the periodic behaviour is re-established as a period-3 solution which, however, vanishes again at $\alpha = 0.17$ where we find the same *double humped* chaotic return map as in fig. 3c of ref. [2]. Note, however, that if initial conditions $\phi(0) = \phi'(0) = 0$ are used chaos already occurs for $\alpha = 0.1695$ as shown in fig. 2. Already for $\alpha = 0.17007$ the double humped return map depopulates into a chaotic period-5 window, which has already vanished again for $\alpha = 0.1705$ (fig. 1). The double humped envelope curve for this value is very similar to the curve obtained for $\alpha = 0.17$. A closer analysis of the return map shows that the system stays for a number of iterations on the lower hump (which has a double-curve structure). Then it moves to the upper hump (single-curve structure) for a number of iterations before it goes back to the lower hump. This *intermittency cycle* continues as far as we have followed it.

When the parameter α is raised to the value $\alpha = 0.1706$ two things may happen: The system may choose the attractor which corresponds to the lower hump of the curve (as shown in fig. 1) or the attractor which corresponds to the upper hump of the curve

(as shown in fig. 2). Thus a special type of bifurcation occurs between $\alpha = 0.1705$ and 0.1706 . By means of computer experiments we have checked that the choice depends on whether the initial conditions for the run already lie on the lower attractor or the upper attractor, respectively. Also, we have found that initial conditions $\phi(0) = \phi'(0) = 0$ lead always to the upper attractor as shown in fig. 2. The following runs demonstrate that the system stays on the preferred attractor as α is increased. For $\alpha = 0.17125$ the lower attractor (fig. 1) and the upper attractor (fig. 2) have depopulated into period-2 windows. For $\alpha = 0.17129$ period-16 solutions (on the attractors) occur in both cases. For $\alpha = 0.1713$, 0.1714 , and 0.1715 a sequence of period-8, period-4, and period-2 solutions is observed similarly. For $\alpha = 0.173$ the period-1 solution indicated in fig. 2 of ref. [2] is found.

The chaotic behaviour indicated by "c" at $\epsilon = 0.5$ and $\alpha = 0.16-0.17$ in fig. 2 of ref. [2] has an extremely detailed structure within a small portion of parameter space. In particular, note that the "single hump" return map reported in ref. [2] is in fact extremely structured. Since the phase space is two-dimensional a purely one-dimensional return map is not expected, the closeness depending sensitively on the parameter ϵ . Similar small deviations from a one-dimensional *circle* map have been found in ref. [8] in a dc + ac driven single pendulum.

It is our pleasure to thank Klaus Fesser and Robert D. Parmentier for helpful discussions. The financial support of the European Research Office of the United States Army (through contract No. DAJA-37-82-C-0057), the Consiglio Nazionale delle Ricerche (Italy) to the author (M.B.) and U.S.D.O.E. to the author (A.R.B.) is gratefully acknowledged.

- [1] V.K. Kornev and V.K. Semenov, Chaotic and stochastic phenomena in superconducting quantum interferometers, to be published.
- [2] K. Fesser, A.R. Bishop and P. Kumar, Appl. Phys. Lett. 43 (1983) 123.
- [3] R.K. Ritala and M.M. Salomaa, Phys. Rev. B29 (1984) 6143.
- [4] M.J. Ablowitz, A. Ramani and H. Segur, J. Math. Phys. 21 (1980) 715.
- [5] M. Bartuccelli, Licentiate Thesis, Laboratory of Applied Mathematical Physics, The Technical University of Denmark, Lyngby, Denmark, to be published.
- [6] IMSL, International Mathematical and Statistical Library (Ed. 8) DVERK-1 (1980).
- [7] M. Hénon, Physica 5D (1982) 412.
- [8] P. Bak, T. Bohr, M.H. Jensen and P.V. Christiansen, Solid State Commun. 51 (1984) 231.

END

FILMED

1-86

DTIC